MAGISTERARBEIT / MASTER’S THESIS

Titel der Magisterarbeit / Title of the Master‘s Thesis

„Dust Opacity Tables for Protostellar Environments“

verfasst von / submitted by

Eva Brigitte Trausinger, Bakk. rer. nat. BSc

angestrebter akademischer Grad / in partial fulfilment of the requirements for the degree of

Master of Science (MSc)

Wien, 2018 / Vienna 2018

Studienkennzahl lt. Studienblatt / degree programme code as it appears on the student record sheet:	A 066 861
Studienrichtung lt. Studienblatt / degree programme as it appears on the student record sheet:	Masterstudium Astronomie UG2002
Betreut von / Supervisor:	Univ.-Prof. Dr. Ernst Dorfi

Acknowledgments

First of all, I want to thank my supervisor Univ.-Prof. Dr. Ernst Dorfi for his support and all the knowledge he provided me with. I am also very grateful to Florian Ragossnig and Daniel Steiner for their helpful comments regarding the field of protoplanetary atmospheres and numerics.
A special thanks goes to my family and all my dear friends, especially Nadja and Christian who invested some of their time for test reading.

I devote this work to my parents Brigitte and Rudolf, my husband Daniel, and to my brother Gert and his wife Lisa who supported and encouraged me through all these years.

Contents

Abstract (german)

Die Opazität oder Extinktion beschreibt die Abschwächung von Strahlung beim Durchqueren eines Mediums durch Absorption und Streuung. Sie ist somit eine Eigenschaft des betrachteten Mediums selbst, beeinflusst thermodynamische Größen und in weiterer Folge auch die Dynamik des Systems, und ist daher vor allem in der Evolution von protoplanetaren Scheiben relevant. Es gibt zwei Opazitätsmittel, die die über die Frequenzen integrierte Opazität beschreiben. Das Planck Mittel findet Anwendung für optisch dünne Umgebungen, geht daher in die Strahlungsenergiegleichung sowie in die innere Energiegleichung ein. Die Gewichtung erfolgt mittels der Planck Funktion. Das Rosseland Mittel, das für den optisch dicken Fall gilt, wird mit der Ableitung der Planck Funktion nach der Temperatur gewichtet und geht in die Strahlungsflussgleichung sowie in die Bewegungsgleichung ein.
In protoplanetaren Scheiben wird die Opazität durch die Streuungs- und Absorptionseigenschaften des Gases sowie der festen Partikeln, i.e. Staub, bestimmt. Mit der Zeit wird sich Staub gravitativ bedingt in der Äquatorebene der Scheibe ansammeln und zur späteren Planetenentstehung beitragen, wohingegegen das leichtere Gas durch den der Gravitation entgegen wirkenden Strahlungsdruck eine stärkere vertikale Ausdehnung aufweisen wird. Daher wird eine getrennte Betrachtung von Staub und Gas, insbesondere in Hinblick auf ihre Opazität wichtig. Zudem wird sich die Größenverteilungsfunktion für Staub auch durch Aggregation, dem Zusammenwachsen von Partikeln, lokalzeitlich verändern, und kann somit nicht als zeitlich konstant angenommen werden.
Ziel dieser Masterarbeit ist daher die Erstellung von Tabellen für monochromatische als auch mittlere Staubopazitäten in protostellaren Umgebungen. Um diese für frühe Entstehungsprozesse der Scheibe als auch spätere Evolutionsphasen, in denen v.a. eine korrekte Modellierung des Verlustes der dichten Uratmosphäre eines Planeten relevant wird, zu berechnen, werden zwei verschiedene Größenverteilungsfunktionen, eine für kleinere Partikelgrößen und die zweite für größere Aggregate, angenommen. Für größere Partikel ist auch der Effekt ihrer Porösität auf die Opazität relevant.
In dieser Arbeit werden daher monochromatische sowie Rosseland und Planck Mittel mit Hilfe von Mie Theorie berechnet, einerseits für kompakte sphärische Partikel, die nur aus einem Material bestehen, und andererseits für Aggregate, die unterschiedliche Porösitäten und Materialmischungen aufweisen. Die benötigten, mittleren Brechungsindizes für Staubaggregate werden mit Hilfe der Effective Medium Theory berechnet.
Die höchsten mittleren Opazitäten ergeben sich für kompakte (nicht-poröse) Aggregate mit Radien von 1-10 μm für Temperaturen $\leq$425 K. Für weiter zunehmende Partikelgrößen, außer für sehr kleine Temperaturen, zeigt sich eine generelle Abnahme der mittleren Opazitäten. Die Annahme von Porösität führt nur für sehr große Aggregate zu einer Opazitätszunahme. Eine Erhöhung des Vakuumanteils für Partikel, die maximale Radien von <10 μm aufweisen, wirkt sich umgekehrt aus und geht mit kleineren Opazitäten einher. Bei Temperaturen über 425 K tragen kleinere Partikel zum Großteil der Extinktion bei.

Abstract

The opacity of a medium describes how much light is extinct by absorption and scattering while traversing it. The combination of these two processes is known as extinction and plays an important role in the evolution of protoplanetary disks since it influences the energy budget of a medium, thermodynamic quantities and hence, hydrodynamics. There are two quantities that describe the mean opacity of a medium integrated over the spectral range. The first is known as the Planck mean, applied to optically thin media with its weighting function being the Planck function for Black Body radiation. The second uses the derivative of the Planck function with temperature as the weighting function and is called Rosseland mean. While the Planck mean enters into the radiation energy equation and the internal energy equation, the Rosseland mean is needed for the calculation of the radiation flux equation and the equation of motion, and is suited for optically thick media.

Due to segregation processes during the evolution of a protoplanetary disk, heavier materials, i.e. dust, will accumulate at the disk's equator resulting in later planet formation while gas, supported against gravitation through radiation pressure, will still extend farther outwards. Therefore, the separation of dust and gas dynamics becomes a necessary issue and seems even more important for protoplanetary atmospheres. Beside this, also the size distribution function that is often viewed as constant during the whole disk evolution changes and has large effects on the mean opacity of the dust medium.

So, the aim of this master thesis is to create opacity tables only for the dust fraction of the medium. To cover early evolution phases of the disk as well as later stages, in which also correct modelling of the loss of primordial protoplanetary atmospheres becomes relevant, tow different size distributions for smaller and larger aggregate particles are considered. In the case of aggregates, also the effect of porosity is evaluated. A decrease in opacity by assuming larger particle sizes leads to a reduction in planet formation time-scales which would be otherwise comparable to the disk's lifetime and hence, unrealistic.

In this thesis, monochromatic, as well as Rosseland and Planck mean opacities derived with full Mie Theory calculations are presented for compact spherical particles of one species and aggregate particles having different porosities and compositions. Average complex refractive indices for aggregate particles are calculated with Effective Medium Theory. Considering protoplanetary atmospheres, a variation of larger aggregate particle size ranges is assumed and hence, a different size distribution with respect to the standard MRN size distribution.

The highest mean opacities for temperatures $\leq$425 K are obtained from compact aggregates with particle sizes of 1-10 μm. Varying the size distribution and shifting the size range of particles to larger ones is especially important for small temperatures where the narrow dip before the vaporization of water ice becomes lower in magnitude but broader to the left and hence, higher mean opacities at lower temperatures are present while magnitude decreases for higher ones. The assumption of high porosities leads only for very large particle size ranges to higher magnitudes of mean extinction. For smaller particle ranges and high porosities, slopes being similar to those for very small particle size ranges are obtained. At temperatures > 425 K small particles contribute most to extinction.

1. Introduction

The opacity or extinction of a medium or particle can be described as its non-transmissivity of light. It is defined as the sum of absorbed and scattered light within this medium or by a particle. Due to different materials with different scattering and absorption properties, more or less energy is brought into that system, thereby influencing thermodynamic properties as well as hydrodynamical quantities that in turn influence the whole evolution of the, in our case, protoplanetary disk environment or protoplanetary atmosphere.

Dust is the main opacity source in a protostellar environment. Correct modelling of heating and cooling mechanisms within a protostellar disk or atmosphere is hence determined by a correct description of the dust opacity depending on size distribution, composition, structure and spatial and temporal variation.[8]

Due to segregation processes during the evolution of a protoplanetary disk, heavier materials, i.e. dust, will accumulate at the disk's equator resulting in later planet formation while gas, supported against gravitation through radiation pressure, will still extend farther outwards[1]. So, the separation of dust and gas dynamics becomes a necessary issue and seems even more important for protoplanetary atmospheres. This can be achieved by creating opacity tables only for the dust fraction of a medium which is the aim of this Master thesis. There were a few authors who already did groundwork on this topic for protoplanetary disks (e.g. Pollack et al.[26, 27], 1985; 1994), some of them also considered particle aggregation and the effect of porosity (e.g. Mathis & Whiffen[20], 1989; Henning & Stognienko[13], 1996; Voshchinnikov et al.[35], 2006). The most commonly used opacity tables may be the ones of Semenov et al.[31] (2003) continuing on some of the papers mentioned but having the disadvantage that the opacity means consist of a prior assumed mixture of gas and dust as one medium. Therefore, they do not allow consideration of segregation processes when feeding them into a protoplanetary disk evolution model. Beside this reason, also the size distribution function that is often viewed as constant during the whole disk evolution changes and has large effects on the mean opacity of the dust medium.

Especially when considering the evolutionary time-scale of runaway gas accretion on protoplanets, the effect of opacity becomes crucial[28, 25, 21]. A decrease in opacity from orders of 1 cm^2/g for interstellar dust size distributions to 10^{-2} cm^2/g by assuming larger particle sizes through aggregation processes, leads to a reduction in planet formation time-scales which would be otherwise comparable to the disk's lifetime and hence, unrealistic.

In general, one can describe the change in the irradiation of the light beam occurring when traversing a medium of thickness ds and density ρ by[3, 5]

$$dI = -I_0 \kappa \rho ds, \tag{1.1}$$

with I_0 being the initial irradiation of the light beam and κ being the attenuation or extinction coefficient describing the attenuation of light in the medium by scattering and absorption.

1.1. Scattering and Absorption

Scattering, in its simplest description, is the change in the light beam's direction of propagation when interacting with particles. Whereas absorption by a particle describes the energy loss of the radiation, changing its initial wavelength to longer, i.e. less energetic, ones. The sum of these processes is known as extinction since light is removed from the initial direction of propagation. In more detail, a particle interacts with radiation in the form that the electric field of the incident wave introduces an oscillatory motion on the electrical charges within the particle, e.g. an excitation of electrons to higher energy levels in the atom. This oscillation of protons and electrons leads in turn to a secondary radiation, e.g., when the electrons move back to lower energy levels - a state of least resistance and minimal potential energy -, that is known as scattering. A part of the energy of the electromagnetic wave is thereby transformed into thermal energy and hence, absorbed leading to a change in the wavelength of the outgoing radiation. So, these two processes are in general not independent from each other and occur in all media except, of course, in vacuum. Phenomena, like reflection and diffraction, are also outcomes of scattering.[3]

There are different forms of scattering depending on the scattering angle Θ, with cos(Θ)=1 for totally forward scattering and cos(Θ)=0 for isotropic or Rayleigh scattering.[26]

1.1.1. Optical constants

The absorption and scattering properties of a material are defined by its complex refractive index N which can be determined by laboratory measurements[3]:

$$N = n + ik \equiv n' + in'' \tag{1.2}$$

While the imaginary part provides information about the absorption of the incident light within the particle or medium, the real part determines its phase velocity $v = c/n$. Both, commonly denoted as n or n' (real part) and k or n" (imaginary part), are commonly referred to as optical constants which can be somewhat confusing since they vary very strongly with wavelength or frequency.[3]

The above mentioned properties of n' and n" can be seen when assuming an electromagnetic plane wave with the electric part/field vector[3]

$$E_c = \mathbf{E_0} \exp(i\mathbf{k} \cdot \mathbf{x} - i\omega t) \tag{1.3}$$

with $\mathbf{k}$ being the complex wave vector, $\mathbf{x}$ the space vector, and ω the oscillation frequency. Analogue to this, of course, a magnetic wave $\mathbf{H_c}$ exists. Splitting $\mathbf{k}$ into its real and imaginary part with $\mathbf{k} = \mathbf{k}' + i\mathbf{k}''$, we get

$$E_c = \mathbf{E_0} \exp(-\mathbf{k}'' \cdot \mathbf{x}) \exp(i\mathbf{k}' \cdot \mathbf{x} - i\omega t) \tag{1.4}$$

with $\mathbf{E_0} \exp(-\mathbf{k}'' \cdot \mathbf{x})$ being the amplitude of the electric wave, and $\Phi = \mathbf{k}' \cdot \mathbf{x} - \omega t$ its phase. Using the Maxwell equations for plane waves and assuming that $\mathbf{k}$, $\mathbf{E_0}$ and $\mathbf{H_0}$ are perpendicular, we obtain

$$k = \omega\sqrt{\epsilon\mu} = \frac{\omega N}{c} \tag{1.5}$$

with the complex refractive index

$$N = c\sqrt{\epsilon\omega} \tag{1.6}$$

ϵ and μ are the electric and magnetic permeability, c is the speed of light. Substituting relation 1.5 into equation 1.4 and taking into account $\omega/c = 2\pi/\lambda$ yields the above mentioned properties, i.e. n'' describing the attenuation of the wave and n' determining its phase velocity:[3]

$$E_c = \mathbf{E_0} \exp\left(-\frac{2\pi n''\hat{\mathbf{e}} \cdot \mathbf{x}}{\lambda}\right) \exp\left(\frac{2\pi i n'\hat{\mathbf{e}} \cdot \mathbf{x}}{\lambda} - i\omega t\right) \tag{1.7}$$

1.2. Formation of Protostars and Protoplanetary Disks

Protoplanetary disks evolve around young stellar objects in dense molecular cloud cores. When a dense core collapses, a protostar with a circumstellar disk forms. Later on, through instabilities and collisions in the protoplanetary disk, material can accumulate to result in a protoplanet. In general, star formation takes place in clusters. In the following, the interaction between protostars in such an environment is neglected and, for simplification, only the formation of a disk around a single star is considered.

In a molecular cloud in magneto-static equilibrium thermal pressure and magnetic forces act against self-gravity. Charged particles gyrating around the magnetic flux lines collide with neutrals and thereby counteract gravity by keeping them from drifting inwards. Dense cores are low ionization fractions of molecular clouds, so more neutrals can slip through the magnetic field lines. This process is known as ambipolar diffusion. Hence, mass enclosed within the innermost flux tubes increases due to the inward drift of neutrals while the total magnetic flux threading the cloud decreases.[32]
With increasing density the core becomes more opaque to its cooling radiation which results, combined with the ongoing compression, in a rise of the inner temperature. Incoming, by the enhanced pressure force decelerated material re-radiates energy before settling on the core's surface and becoming buried under new matter. This cooling of the outer shell in turn enhances compression. The material of this first core consists mostly of molecular hydrogen resulting in an early collapse. A rise in temperature beyond 2000 K initiates the collisional dissociation of H_2. The energy needed for this process is very high compared to the thermal energy of the molecules. So, energy gained by compression is absorbed while the temperature will not change immensely. Due to this, at some point, the increase in gravitational force cannot be counteracted any longer by the internal pressure. This leads to the collapse of the first core after a partially atomic hydrogen region has formed. The resulting high density ($\sim 10^{-2}$ g cm^{-3}) and temperature (> 10^5 K) of the central region leads then to the ionization of most of the hydrogen via collisions, and the formation of a dynamically stable protostar. The luminosity of the new born star is mainly produced by external mass accretion, and is thus called accretion luminosity. The kinetic energy of infalling gas is almost completely converted into radiation as it is abruptly decelerated at the stellar surface. The protostar's outer boundary is determined by an accretion shock front, marking the transition between slow, on the protostar settling, and freely infalling material. There are also minor contributions to the radiation coming from inner contraction and nuclear fusion, and resulting in turbulent motion, i.e. convection, in the protostar's interior (see figure 1). The dust density in the very dense surroundings of the protostar is very high which is why the star itself remains optically invisible and can only be observed in the IR regime and longer wavelengths.[32]

Since every molecular cloud is rotating, angular momentum must be removed from the infalling material that forms the protostar. Otherwise the angular speed of matter would increase with decreasing radius leading to the disruption of the protostar by the enhanced centrifugal force. So we should take a step back to look at the evolution and contribution of the magnetic field.[32]
As the density in the dense core rises and the gravitational forces acting on the surrounding mass

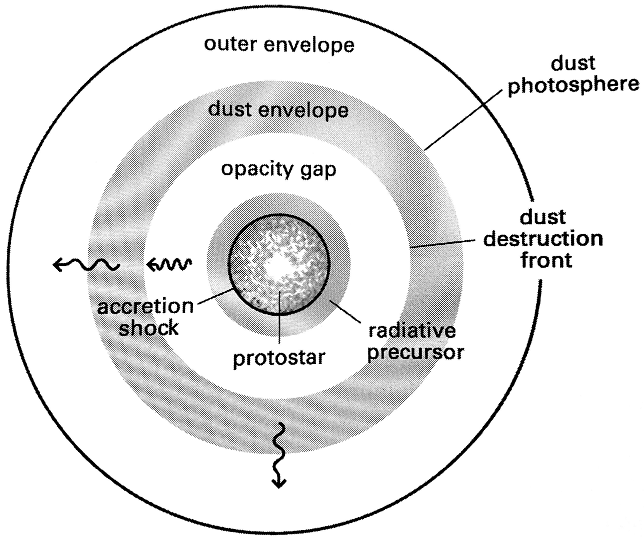

Figure 1: Structure of a protostar (Stahler & Palla,[32] 2004).

increase, also the magnetic field lines are pulled inwards (see fig. 2) since now the neutrals exert a drag force on the ions and electrons that are coupled to the magnetic field. This effect refers to magnetic flux freezing in a plasma. Charged particles are bound to the magnetic field and vice versa, hence the magnetic field lines move with the plasma. As a result, magnetic tension builds up in the equatorial region (B in fig. 2). Also, a movement of gas perpendicular to the magnetic field lines, i.e. the direction of least resistance, occurs and leads to the formation of a somewhat elongated core. In these columns below and above the center (A and A' in fig. 2) only thermal pressure acts against the gravitational force and collapse will start when a critical length of the column, the so called Jeans length, is exceeded. As far as the magnetic tension in the equatorial region is concerned, an increase in density of the central core does not only lead to a decrease in the ionization fraction, as matter cools and recombination takes place. Matter will successfully decouple from the magnetic field as it approaches the center, and its drift velocity becomes comparable to the free-fall velocity. The residual magnetic field remaining undergoes magnetic reconnection when coming near other field lines of reversed sign. This results in an outburst of thermal energy transformed from magnetic flux, known as Ohmic dissipation, and a rearrangement of the magnetic field lines.[32]

Observations of dense cores show that they are slowly rotating regions. The effect responsible for the removement of angular momentum is known as magnetic braking and becomes crucial once the rotation of a magnetized cloud is taken into account. The spin-up of an infalling particle twists the magnetic field in azimuthal direction (see fig. 3). The slight bending of the magnetic field line leads to a build-up in magnetic tension acting as a restoring force, and putting the plasma into oscillation. This creates a magnetic-hydrodynamic wave, i.e. a torsional Alfvén

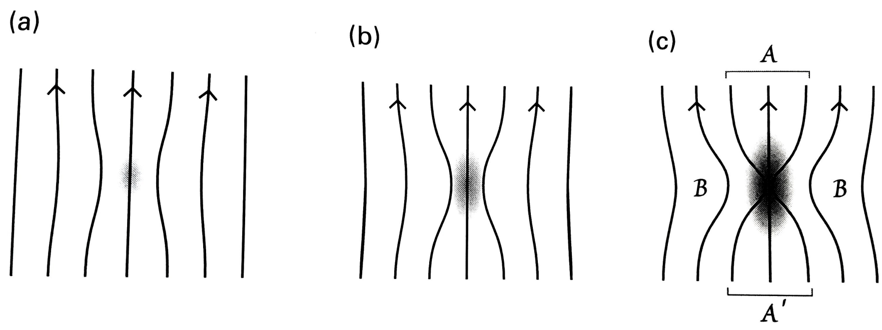

Figure 2: Evolution of dense cores (Stahler & Palla,[32] 2004).

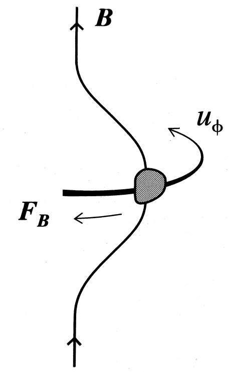

Figure 3: Rotational twisting of a magnetic field line (Stahler & Palla,[32] 2004).

wave, propagating along the magnetic field lines and transporting angular momentum away in poloidal direction. Magnetic braking is expected to operate from the earliest evolution of a dense core and enforces co-rotation in a cloud.[32]

But magnetic braking must fail in the deeper interior of a molecular cloud for a disk to evolve. This fact is given by the assumed removement of the magnetic flux, as discussed above. So once the magnetic field has decoupled and the thermal pressure, assuming a supersonic velocity, has decreased, the infall of matter is only regulated by the gravitational and centrifugal force. The angular momentum in the absence of a significant magnetic field is then conserved, and the angular velocity of matter increases when approaching the protostar. This spin-up results in a rise of the centrifugal force acting on the infalling material which will then not arrive at the protostar's surface and instead settle farther outside on the equatorial region where a disk will evolve. The particle's specific angular momentum distinguishes how far away from the protostar its settlement will be. The extent of this disk is determined by the centrifugal radius, i.e. the maximum impact distance of gravitationally displaced matter. Due to the described inside-out collapse of the core, the centrifugal radius will increase with time since $R_{\rm cen} \propto \Omega^2 t^3$, with Ω as the angular rotation rate. This is because material originating farther outside, and thus exhibiting a higher

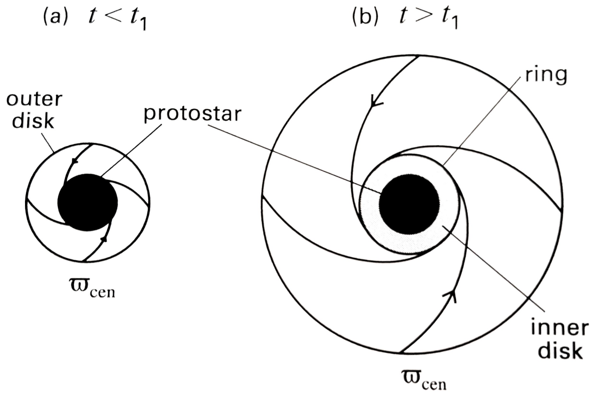

Figure 4: Early growth of a protostellar disk: (a) Before a certain time t_1, matter spirals inwards to fall directly onto the protostar. (b) With ongoing growth of the disk defined by its centrifugal radius $\bar{\omega}_{\rm cen}$, matter residing farther outwards will be pulled inwards by the increasing gravitational force, but no longer reaches the central star. Instead, its streamlines converge and form a dense ring which transfers mass to an inner disk around the star (Stahler & Palla,[32] 2004).

specific angular momentum, will be attracted and displaced by the growing central mass' exerted gravitation. Due to the ongoing impact of material, another accretion shock covering the whole disk's surface forms. Infalling matter from above and below the equatorial plane will conserve only its horizontal momentum, and is deflected towards the central protostar sustaining its mass accretion. As the centrifugal radius rises and the accretion shock weakens, matter impacting the outermost part of the disk will no longer reach the star. As a consequence, the surface density of the disk will increase. Fig. 4 shows the streamlines of matter elements penetrating towards the protostar. As the disk grows, the streamlines will meet prior reaching the star and an inner, nearly circular disk will form. The high-density region is surrounded by a ring of turbulent gas. Due to the impacting material outside the inner disk, a slight drag force will cause the nearly circular orbits to slowly spiral inwards. As the centrifugal radius and the inner disk grow, the drag force exerted by impacting material on the ring will become weaker and the protostar's mass accretion will slow down. So another process sustaining mass accretion onto the protostar is needed to get the observed disk to star mass ratio that is typically around a few percent for pre-main-sequence stars. Otherwise the disk would soon outgrow its protostar by mass. Hence, angular momentum transfer from inner to outer regions is needed for matter to penetrate towards the center. This internal torquing could be provided by internal friction or shear viscosity but is still not fully understood. Another possibility would be provided by spiral waves that create gravitational torques. Spiral density waves form when regions within the disk become gravitationally unstable. This happens when the density of a fluid element rises and the self-gravitation is no longer counteracted by the pressure and centrifugal force. The density perturbations are then subject to shearing and a spiral pattern forms.[32]

A stability criterion is given by the Toomre-Parameter with

$$Q \equiv \frac{\Omega(r) c_s}{\pi G \Sigma} > 1. \tag{1.8}$$

Here $\Omega(r)$ is the Keplerian speed or angular velocity of a particle, c_s is the internal sound speed, Σ is the surface density and G is the gravitational constant.[1, 32]
The Toomre-Parameter is also important for the formation of planetesimals, as will be mentioned in section 1.6.[1]

1.3. Classification of Young Stellar Objects

Young stellar objects (YSO's) can be classified by their spectral energy distribution (SED). It is the slope of the SED curves that specifies their evolutionary state. A possible infra-red excess, i.e. an enhanced emission above the black body radiation of the star, signals the existence of a protoplanetary disk.[1]
Four different classes exist:[1]

- **Class 0**
  In the early stages of protostellar evolution a protostar is still embedded within an envelope of optically thick gas and dust absorbing stellar radiation. Its SED is therefore marked by a lack of emission in the visible and near-IR wavelengths. A potentially already formed disk around the protostar cannot be yet detected.

- **Class I**
  The protostar and its disk are still embedded within gas and their SED curve is still shifted to longer wavelengths. A strong accretion of material from the disk or the envelope onto the surface of the star leads to outflows and jets with high velocities.

- **Class II**
  Once the envelope is thinned out due to accretion onto the star and its protostellar disk, the SED shows the visible emission from the star and near-IR to mm excess added by the disk. Accretion from the disk onto the star results in an additional UV excess.

- **Class III**
  After a few Myrs the disk has almost dissipated and the object becomes a pre-main-sequence star.[1]

1.4. Properties of Protoplanetary Disks

The main source of heating for a 'passive disk' stems from the absorbed stellar radiation. But within a disk also dissipation of gravitational potential energy, i.e. accretional heating, provided by material that spirals towards the star occurs. Both sources decrease strongly with increasing distance from the star. There are some analytical simplifications concerning the shape (razor-thin, flared, warped) of passive disks. A razor-thin disk re-emits the absorbed stellar radiation

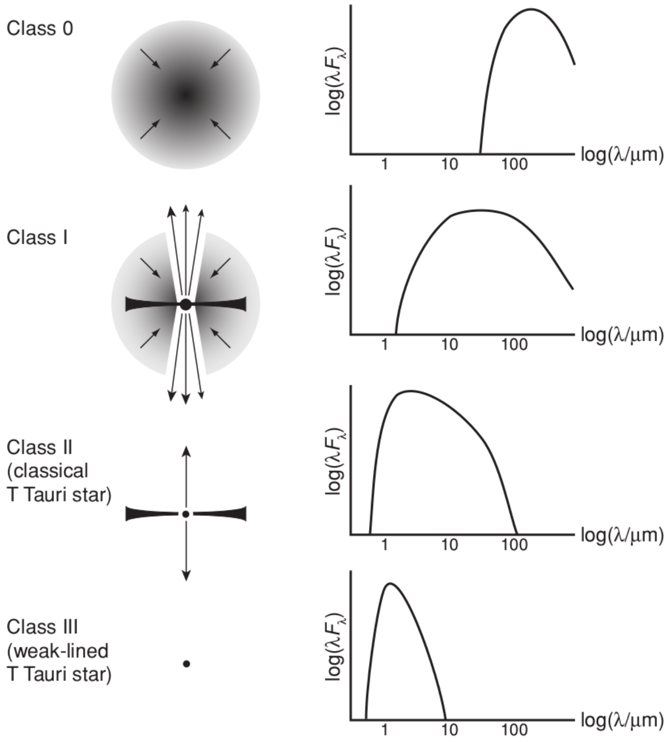

Figure 5: Classification of Young Stellar Objects (Armitage,[1] 2009).

locally as a black body. It has a steep temperature profile with $T_{\mathrm{disk}} \propto r^{-3/4}$. A flared disk is described as having an increasing ratio of h_{p}/r with radius, h_{p} being the height above the mid-plane where stellar radiation is absorbed. They show a stronger IR excess than thin disks since they also absorb more stellar radiation. At larger distance from the star the temperature profile becomes $T_{\mathrm{disk}} \propto r^{-1/2}$.[1]

In reality, of course, the disk does not re-radiate as a single black body. When considering dust as the dominant opacity source, which absorbs short wavelengths more efficiently than emitting at longer ones, we must assume an optically thick disk with a surface layer that is optically thin to longer wavelengths. So, the disk's emission is the sum of a cool black body component from the disk's interior and a warmer one representing the surface layer. While the optically thin layer re-emits half of the radiation coming from the star back to space, the other half is re-emitted downwards to be absorbed by the disk's interior. This two-component disk model (see figure 6) describes radiative equilibrium disks and can be applied as long as non-radiative cooling due to collisions between molecules and dust can be neglected. This means that thermal decoupling of gas and dust is fulfilled as long as the gas density in the optically thick regions is low enough which is the case, especially at larger radii.[1]

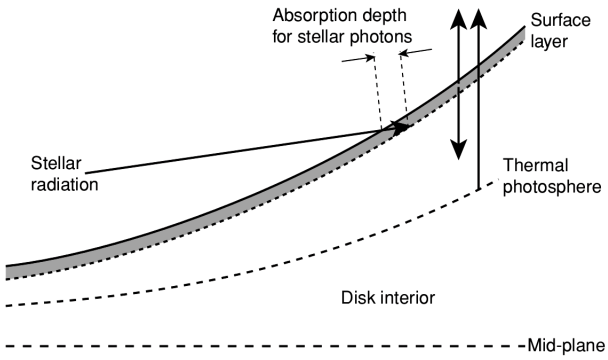

Figure 6: Two-component disk model for radiative equilibrium disks (Armitage,[1] 2009).

1.5. Dust in Protoplanetary Disks

The chemistry in protoplanetary disks is linked to disk dynamics. Together with grain evolution, it influences the ionization structure of the disk and hence, magnetohydrodynamics and the transport of angular momentum. Because of its dependence on temperature, density and radiation fields, it is in turn influenced by the dynamics of the disk.[14]
In general, molecular hydrogen and helium account for the dominant mass fraction in a protoplanetary disk. Dust particles are mostly present in the form of amorphous silicates, crystalline forsterite, water ice and other molecular ices having sizes that can grow far beyond the typical sub-micron sizes of interstellar dust grains.[14] They constitute the main opacity source for a protoplanetary disk, except in the inner regions where the temperature exceeds vaporization temperatures ($\sim$1500 K) and dust is destroyed. Within the inner disk, the mean free path of thermal radiation is small compared to the disk's scale-height resulting in an approximately isotropic and black body radiation field.[1]
In the colder outer mid-plane of the disk, molecules freeze out on grain surfaces. Most of the molecular line emission observed in the sub-mm range where the dust is optically thin, originates from here. This is in contrast to infra-red (IR) wavelengths where dust is optically thick and the bright dust continuum emission overlaps molecular line emission. Hence, high spectral resolution is needed to distinguish between them. Since the different wavelength ranges correspond to different temperatures, they can be used to study different regions of the disk (see figure 7). Inner disk chemistry is best observed in the IR while for the outer disk sub-mm wavelength observations are needed. Beside the destruction of molecules due to photo-dissociation, the observation of molecular lines delivers important information considering the, above mentioned, freeze-out on solid grains and hence, dust growth.[14]
Observational evidence shows that emission in the mid-IR of T Tauri and Herbig Ae/Be stars is dominated by vibrational resonances in amorphous and crystalline silicates, especially crystalline forsterite, enstatite and, to some extent, silica, originating from the warm surface layer with temperatures above 100 K. The strength and shape of the observed 10 μm feature in spectra of Herbig Ae/Be stars, originating from porous iron-poor amorphous silicates, suggests strong grain growth to micron-sized particles. With ongoing settling of the dust grains the optically

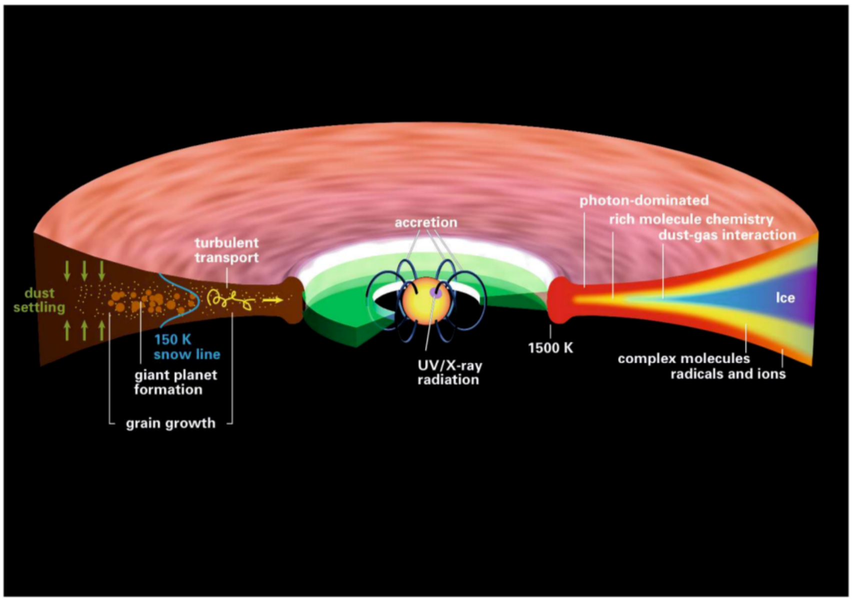

Figure 7: Physical and chemical structure of a 1-5 Myr old protoplanetary disk around a Sun-like star (Henning & Semenov,[14] 2013).

thick disk region expands while the disk's vertical structure flattens. Dust emission in the mm and cm-wavelength regimes proves the existence of grains up to cm-sizes.[14]
Crystalline silicates are present as sharp bands in nearly all disk spectra and have mass fractions ranging from 1 to 30%. This is in contrast to molecular clouds and the diffuse interstellar medium (ISM) which lack in crystalline silicates. The occurring crystallization can be explained by mechanisms of strong thermal processing in the disks, like thermal annealing and condensation in the inner regions or shock heating in the outer ones. Varying with location, the forsterite to enstatite mass ratio is lower in the inner disk and higher in the outer regions with forsterite particles being, in general, nearly iron-free. Fe and FeS particles have not yet been detected by IR spectroscopy but should certainly be present. This could be due to a lack in abundance, maybe too large sizes to show strong features or because they simply do not show intrinsic IR bands. In disks seen edge-on, absorption features suggesting evidence for molecular ices are present.[14]
Due to the strong vertical and radial temperature and density gradients in protoplanetary disks the chemistry is manifold and subject to various chemical reactions.[14]

1.6. Formation of Protoplanets

The formation of planets can be divided into 3 main stages - planetesimal formation, terrestrial planet formation and giant planet formation and core migration.[1] I will focus only on the first two stages since for this thesis only the atmosphere of terrestrial protoplanets is relevant.

1.6.1. Dust Settling

Before planetesimals of sizes of approximately 1-100 km will form in the mid-plane of the disk, dust has to settle near the disk's equator. Whereas gas is supported against the gravitational force through radiation pressure, small solid particles are not and will be accelerated downwards (i.e. in the direction normal to the disk's equator). At some point, the gravitational force they experience will be balanced out by an aerodynamic force. Depending on the particle size s and the mean free path λ of the gas molecules, one distinguishes between Epstein drag ($s \lesssim \lambda$) - derived by considering the frequency of collisions between gas represented as molecules with a Maxwellian velocity distribution and solid particles - and Stokes drag ($s \gtrsim \lambda$) - treating the gas as a fluid and neglecting its molecular nature - as the dominant drag forces. Both scale with the frontal area πs^2 of the particle meaning that the drag force exerted on the particle, and hence the acceleration, decrease with increasing particle size and become less important once planetesimals have formed.[1]
The Epstein drag is defined as:[1]

$$\mathbf{F}_{\mathbf{D},\mathbf{E}} = -\frac{4\pi}{3}\rho s^2 v_{\mathrm{th}}\mathbf{v} \tag{1.9}$$

It acts in the opposite direction of the particle's relative velocity $\mathbf{v}$ to the gas. v_{th} and ρ are the mean thermal velocity of the molecules and the particle's density, respectively.[1]
Stokes drag is proportional to ram pressure acting on a particle with[1]

$$\mathbf{F}_{\mathbf{D},\mathbf{S}} = -\frac{C_D}{2}\pi s^2 \rho v \mathbf{v}. \tag{1.10}$$

The drag coefficient C_D for spherically assumed particles is independent of shape and proportional to, as well as scaled with, the fluid Reynold's number $Re = 2sv/\nu_{\mathrm{m}}$ that describes the flow motion (turbulent/laminar) by taking into account the molecular gas viscosity v_{m}. The transition between Epstein and Stokes drag occurs at particle sizes of $s = 9\lambda/4$.[1]
When balance between gravitational and drag force is achieved, the solid particle will drift towards the mid-plane with a terminal velocity, i.e. the settling velocity. The friction time-scale, $t_{\mathrm{fric}} = mv/|F_D|$, describes how fast this balance is achieved, i.e. the time in which the relative velocity is modified significantly by drag to become the settling velocity. In the Epstein regime, balance between gravitational and drag force yields for the settling velocity:[1]

$$v_{\mathrm{settle}} = \frac{\rho_{\mathrm{m}}}{\rho}\frac{s}{v_{\mathrm{th}}}\Omega^2 z = t_{\mathrm{fric}}\Omega^2 z \tag{1.11}$$

with Ω, z and ρ_m being the Keplerian angular velocity, the height above mid-plane and the material density, respectively.[1]
The settling velocity leads to the definition of a settling time $t_\mathrm{settle} = z/|v_\mathrm{settle}|$ that is rather short compared to the disk's lifetime when turbulence acting against the settling is neglected. Also the coagulation due to collisions of solids must be accounted for. The growth in particle size and mass increases the gravitational force and decreases the aerodynamic force acting on the particles. Hence, also the settling velocity increases leading to a faster collapse of the dust towards the equator. Due to turbulence substantial particle growth is required for dust to settle.[1]
Hence, an initial assumed size distribution for dust particles in the protoplanetary disk changes during its evolution.

1.6.2. Radial Drift

Gravitational forces acting on the gas in the disk are only partially counteracted by an outward pressure gradient. Due to this fact, gas orbits a star of mass M_* at sub-Keplerian velocity and will slowly spiral inwards since the centrifugal force will not balance out the gravitational force.[1]
Hence, the orbital velocity of the gas is defined as[1]

$$\frac{v_{\Phi,\mathrm{gas}}^2}{r} = \frac{GM_*}{r^2} + \frac{1}{\rho}\frac{dP}{dr}. \tag{1.12}$$

Assuming a mid-plane pressure defined as a power-law in radius, $P = P_0(r/r_0)^{-\mathrm{n}}$, and substituting $P_0 = \rho_0 c_\mathrm{s}^2$, with c_s being the speed of sound, it can be rewritten as

$$v_{\Phi,\mathrm{gas}} = v_\mathrm{K}(1-\eta)^{1/2}, \tag{1.13}$$

with Keplerian velocity $v_\mathrm{K} = \sqrt{GM_*/r}$ and $\eta = nc_\mathrm{s}^2/v_\mathrm{K}^2$.[1]

Small dust particles are aerodynamically coupled to the gas and will therefore spiral inwards. But also larger bodies that show less coupling to the gas will, since the aerodynamic forces exert perturbations on the motion of the bodies that orbit close to the Keplerian speed. Via this effect they act as a brake and result in the loss of angular momentum enhancing again the inward drift of the bodies.[1]
The radial (r) and azimuthal (Φ) momentum equations for solids exposed to aerodynamic drag forces within the gas are:[1]

$$\frac{dv_\mathrm{r}}{dt} = \frac{v_\Phi^2}{r} - \Omega_\mathrm{K}^2 - \frac{1}{t_\mathrm{fric}}(v_\mathrm{r} - v_{\mathrm{r,gas}}), \tag{1.14}$$

$$\frac{d(rv_\Phi)}{dt} = -\frac{r}{t_\mathrm{fric}}(v_\Phi - v_{\Phi,\mathrm{gas}}). \tag{1.15}$$

The azimuthal equation simplifies when assuming inward spiralling of almost circular, Keplerian orbits, meaning that the specific angular momentum is close to Keplerian and hence,[1]

$$\frac{d(rv_\Phi)}{dt} \simeq v_\mathrm{r}\frac{d(rv_\mathrm{K})}{dr} = \frac{1}{2}v_\mathrm{r}v_\mathrm{K} \tag{1.16}$$

and

$$v_\Phi - v_{\Phi,\mathrm{gas}} \simeq -\frac{1}{2}\frac{t_\mathrm{fric}v_\mathrm{r}v_\mathrm{K}}{r}. \tag{1.17}$$

Substituting the relations 1.13 and 1.17 in the radial momentum equation (1.14) and defining a dimensionless stopping time $\tau_\mathrm{fric} \equiv t_\mathrm{fric}\Omega_\mathrm{K}$ yields for the radial velocity:[1]

$$v_\mathrm{r} = \frac{\tau_\mathrm{fric}^{-1}v_\mathrm{r,gas} - \eta v_\mathrm{K}}{\tau_\mathrm{fric} + \tau_\mathrm{fric}^{-1}} \tag{1.18}$$

Small particles tightly coupled to the gas ($\tau_\mathrm{fric} \ll 1$) will hence experience a radial drift relative to the gas that linearly increases with the dimensionless stopping time with $v_\mathrm{r} \simeq v_\mathrm{r,gas} - \eta\tau_\mathrm{fric}v_\mathrm{K}$. The opposite is the case for very large particles. The highest drift velocity $v_\mathrm{r,peak} \simeq -1/2\eta v_\mathrm{K}$ occurs at $\tau_\mathrm{fric} \simeq 1$ and depends only on the pressure gradient.[1]
The minimum radial drift time-scale, defined as the ratio of particle/body distance from the star to the maximum radial drift velocity $t_\mathrm{drift} = r/|v_\mathrm{r,peak}|$, is for reasonable disk parameters very short, in the order of $< 10^3$ years, when considering aerodynamic drag and sub-Keplerian velocities. From this, it becomes clear that the formation of planetesimals must proceed rapid through collisions. Otherwise, most solids would just spiral towards the star and evaporate again in the hotter inner disk regions. Since the radial drift velocity depends on the size of particles, local enhancements or depletions of solids relative to the gas surface density will occur. The introduction of a relative velocity between bodies facilitates collisions. This can lead to particle growth or break-up depending on the magnitude of radial velocities and hence, particle sizes.[1]

1.6.3. Turbulence

Turbulence has a stronger effect on the vertical settling than on the radial inward drift of solids. Especially considering larger bodies, the latter can only be altered by very strong turbulence creating local pressure maxima which force solid particles, drifting always in the direction of the pressure gradient, to flow towards them and pile up. This can happen on time-scales even shorter than the global drift time-scale and can prevent the usual inward drift of larger particles. Small particles coupled to the gas are more exposed to turbulent motion.[1]
The time-scale for vertical diffusion across a scale z to efficiently erase spatial gradients in particle concentrations and hence, oppose vertical settling, can be described by the turbulent diffusion coefficient D as[1]

$$t_\mathrm{diffuse} = \frac{z^2}{D}. \tag{1.19}$$

Equating the settling and diffusion time-scale yields an expression for the diffusion coefficient D. Although the vertical turbulence is not equivalent to the radial diffusion of angular momentum given by the anomalous viscosity ν, numerical simulations suggest that $D \approx \nu$ and hence, the diffusion coefficient can be written as[1]

$$D \approx \nu = \frac{\alpha c_{\rm s}^2}{\Omega}. \tag{1.20}$$

The Shakura Sunyaev α parameter is defined as the efficiency of angular momentum transport by turbulence. Due to the assumption above, a criterion for α, above which turbulence prevents vertical settling, can be defined by the ratio of the column density of a single dust particle to that of the disk:[1]

$$\alpha \geq \frac{\pi e^{1/2}}{2}\frac{\rho_{\rm m} s}{\Sigma} \tag{1.21}$$

The critical value for α is very small for particles in the micron range and hence, turbulence opposes vertical settling in this regime. For particles of sizes $s \approx$1 mm, α is in the order of 10^{-2} which is comparable to estimates for protoplanetary disks. Hence, these particle sizes will no longer be efficiently stirred up by turbulence and settle down.[1]

For the radial transport of solids within a turbulent disk one must consider aerodynamic drag, advection with the mean flow and turbulent diffusion. When considering advection and diffusion as the two dominant processes, radial diffusion is important only for small particles ($s \lesssim$ 1 mm) and for a relatively low Schmidt number $Sc \equiv \nu/D$, i.e. the ratio of the two transport coefficients, namely the viscosity ν of the disk and the turbulent gaseous diffusion coefficient D. When considering larger particles, aerodynamic drag becomes the main process for radial drift and leads to the large-scale redistribution of solids.[1]

1.6.4. Formation of Planetesimals

While the coagulation and growth of small particles via frequent collisions are well understood, the larger relative velocities of bodies with sizes of $s \gtrsim$ 1 m complicate coagulation during collisions. The probability for solids to stick together depends on particle masses, collision velocities and additional parameters describing shape and strength of the particles involved. The sticking efficiency is a function of the particle size, composition (including internal structure and strength) and relative velocity. Relative velocities cover a range from $\Delta v \sim$ 0.1 cm s^{-1} for micron-sized dust particles to $\Delta v \sim$ 10-100 m s^{-1} for meter-sized bodies. Two particles can remain bound when for a given impact velocity the surface forces are strong enough to make them stick together or the internal structure can absorb the energy of the impact efficiently. The first case is especially important for small solids. Neutral dust particles can adhere due to induced dielectric forces during collisions. While for spherical particles with $s \approx$ 0.5 μm the transition between adhesion and bouncing is very sharp with a threshold velocity of around 1-2 m s^{-1}, dust grains of irregular shape have no threshold velocity but the sticking efficiency declines with increasing relative velocity up to 100 m s^{-1} at which the sticking probability becomes 0. For larger bodies the surface area to mass ratio declines, rendering surface forces less important but enhancing the significance of the ability to dissipate energy within.[1]

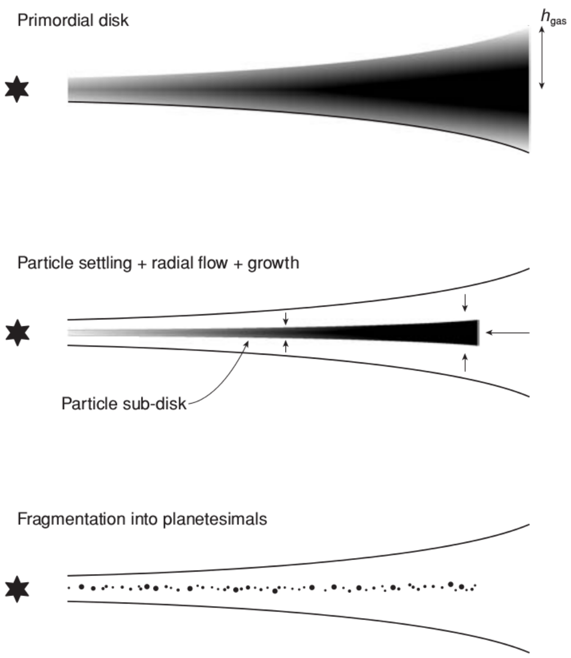

Figure 8: (I) At first solids and gas are well mixed within the disk. (II) With time solids settle near the disk's equator and an inner disk forms. Collisional growth of particles acts against turbulence that hinders settling and becomes less effective for larger solids. The increase in surface density is also supported by the radial inward drift. (III) The disk becomes gravitationally unstable due to increasing surface density and/or decreasing velocity dispersion leading to the formation of planetesimals (Armitage,[1] 2009).

As the number of solids rises they also become dynamically important for the whole disk. So, other effects leading to the formation of planetesimals may occur. These can be gravitational instabilities in the denser layer near the disk's mid plane, turbulence modified by gas-solids feedbacks and two-fluid instabilities including clumping of solid particles around over-densities. The gravitational stability of the disk can be described, like mentioned before, by the Toomre Parameter (see equation 1.8). As the surface density rises and/or the velocity dispersion decreases, the inner disk becomes locally gravitationally unstable leading to clumping and agglomeration of particles and finally, the formation of planetesimals. This mechanism is also known as the Goldreich-Ward mechanism and is pictured in figure 8. This gravitational collapse of a layer of small particles leading to fragmentation and formation of planetesimals, bypasses all the constraints that arise from prior assumed coagulation and growth of particles with sizes in the meter-scale range. It hence forms a welcomed theory to overcome this problem. Since solids build up only 1% of the total surface density, the particle layer must be very thin to become unstable. In addition to this, turbulence becomes a counteracting force. If the particles are small, their radial drift is slowly. In very turbulent regions of the disk the Goldreich-Ward mechanism would fail. Even in an initially laminar flow a dense solid particle layer would excite turbulence. So, much larger local over-densities are needed to overcome this effect and initiate collapse.[1]

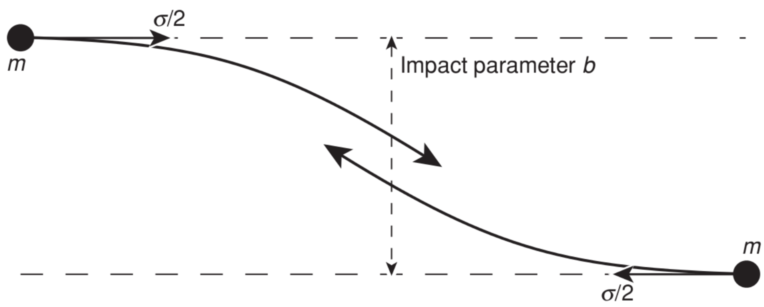

Figure 9: Gravitational focusing (Armitage,[1] 2009).

Other instabilities may enhance particle densities resulting in the formation of clumps, streams, spiral arms, etc. Also, considering our knowledge about the Solar system, the mechanism responsible for the formation of planetesimals must happen rapidly, on time-scales of less then 10^5 years across the whole extent of the disk. Solid bodies of varying composition show a rather smooth radial distribution across the Solar system.[1]

1.6.5. Formation of Terrestrial Planets

After planetesimals have formed, further growth is controlled by gravitational interaction between them. Bodies of higher masses will gravitationally attract other bodies with trajectories nearby. Hence, their collisional cross-section will be larger than their physical cross-section by a derived factor of $(1 + \frac{v_{\rm esc}^2}{\sigma^2})$. This mechanism, the boost of the cross-section beyond its physical, is called gravitational focusing (see figure 9). Energy balance between two bodies of mass m at initial and final state, i.e. the closest approach at $R_{\rm c}$ and velocity $v_{\rm max}$, yields

$$\frac{1}{4} m\sigma^2 = m v_{\rm max}^2 - \frac{Gm^2}{R_{\rm c}}, \tag{1.22}$$

with σ being the relative velocity at infinity.[1]

Angular momentum conservations leads to $v_{\rm max} = b\sigma/(2R_{\rm c})$ and to the definition of the largest impact parameter that will result in a physical collision of two bodies:

$$b^2 = R_{\rm s}^2 + \frac{4GmR_{\rm s}}{\sigma^2} = R_{\rm s}^2 \left(1 + \frac{v_{\rm esc}^2}{\sigma^2}\right) \tag{1.23}$$

with $R_{\rm s}$ and $v_{\rm esc}^2 = 4Gm/R_{\rm s}$ being the sum of their physical radii and the escape velocity from the point of contact, respectively.[1]

The smaller the random velocity of the bodies compared to the escape velocity from the point of contact, the higher their collisional cross-section and the more likely a collision occurs. A "cold" planetesimal disk with $\sigma \ll v_{\rm esc}$ and hence, $v_{\rm esc}^2/\sigma^2 \gg 1$ will show fast planet growth due to gravitational focusing.[1]

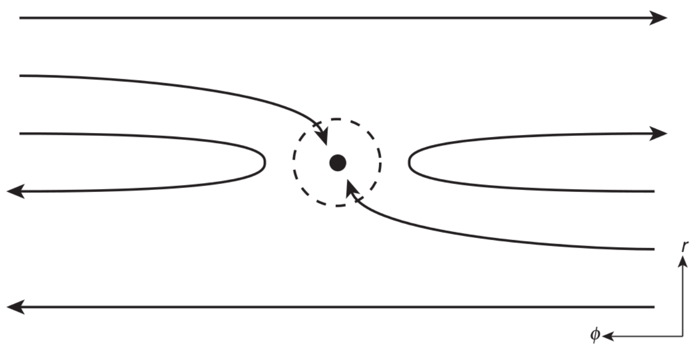

Figure 10: Trajectories of particles on almost circular orbits. Only particles with $\sigma > v_{\mathrm{H}}$ will enter the Hill sphere (dashed) and collide with the protoplanet. Particles with orbits too close to the protoplanet's are in the shear dominated regime and hence, will not enter the Hill sphere (Armitage,[1] 2009).

In protostellar environments we first have to consider at least three bodies when formulating gravitational interaction - star, protoplanet and planetesimal. The radius within which the gravity of the protoplanet dominates over that of the star, and the dynamics hence reduce to a two-body problem between protoplanet and third body, is defined as the Hill radius. As a first estimate, it can be derived by equating the orbital frequency of the protoplanet around the star and that of the third body orbiting the planet at radius r, $\sqrt{GM_*/a^3} = \sqrt{GM_{\mathrm{P}}/r^3}$. A more appropriate derivation over the so called Hill's equations is given in Armitage[1] (2009) and yields

$$r_{\mathrm{H}} \approx \left(\frac{M_{\mathrm{P}}}{3M_*}\right)^{1/3} a. \tag{1.24}$$

Accordingly, the orbital velocity around the protoplanet at this distance is called the Hill velocity:[1]

$$v_{\mathrm{H}} \approx \sqrt{\frac{GM_{\mathrm{P}}}{r_{\mathrm{H}}}} \tag{1.25}$$

One can distinguish between shear dominated and dispersion dominated systems. If the initial velocity of the third body is small compared to the Hill velocity ($\sigma < v_{\mathrm{H}}$), it will not enter the Hill sphere (see figure 10). In this case a three-body effect must be considered. This applies to bodies moving on orbits close to the protoplanet around the star and is called shear dominated regime. If, on the other hand, the initial velocity is larger than the Hill velocity ($\sigma > v_{\mathrm{H}}$), the system is determined by two-body dynamics and is said to be dispersion dominated.[1]

When particles enter the Hill sphere and collision takes place, there are three possible outcomes (see figure 11). The first one is accretion of most of the impactor's mass on the protoplanet or net growth. The collision can also lead to shattering of the protoplanet. But it can again become one object after re-accretion of the fragments. The third outcome would be total dispersal where the pieces of the protoplanet will not re-accumulate again and are not gravitationally bound

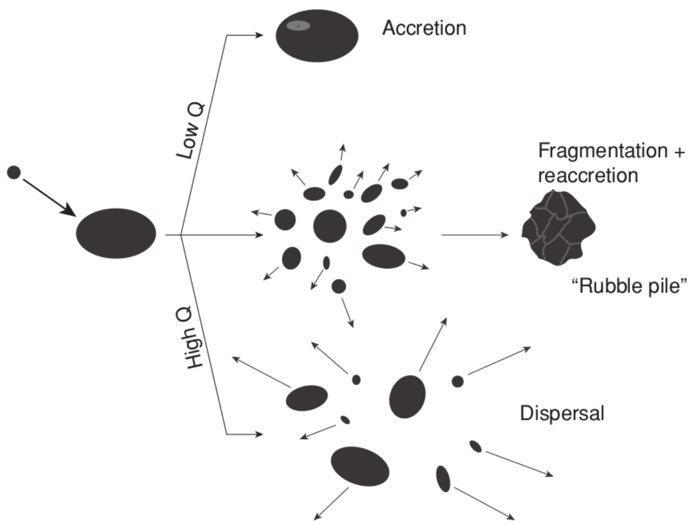

Figure 11: Possible outcomes of collisions (Armitage,[1] 2009).

any more. Besides mass ratio, impact angle, shape, composition (porosity) and rotation rate of the bodies involved, the outcome of the collision depends also on the specific energy Q of the impact.[1]

A massive body surrounded by a couple of smaller planetesimals in the dispersion dominated regime will undergo runaway growth due to gravitational focusing as the dominant process. The rapid growth rate will slow down with time since the velocity dispersion of the planetesimals increases as the protoplanet grows.[1]
For the shear dominated regime a "feeding zone" can be defined, i.e. the shell surrounding the protoplanet within which bodies will be deflected towards trajectories that will enter the Hill sphere.[1]
The maximum mass a protoplanet can attain during runaway growth, i.e. the isolation mass, can be derived assuming the body has "eaten up" all planetesimals in its surrounding. In the shear dominated regime this applies only for bodies that can enter the feeding zone $\Delta a_{\max} = 2\sqrt{3} r_{\mathrm{H}}$ to be deflected towards the Hill sphere with radius r_{H}. As the planet grows also the feeding zone expands, but the mass of new planetesimals increases more slowly. Assuming values typical for our planet, the mass at which a planet is isolated lies around 0.07 $M_{\oplus}$.[1]

Changes in the velocity dispersion of planetesimals are governed by viscous stirring - the excitation of motions due to weak gravitational encounters in the initially cold disk for bodies of equal masses -, dynamical friction - energy is transferred from massive bodies to smaller, less massive ones -, aerodynamic drag and inelastic collisions that result in energy dissipation.[1]
In an initially cold disk gravitational scattering or viscous stirring heats up the disk, the encounter velocities increase and so does the vertical extent of the disk with time as $\sigma(t) \propto t^{1/4}$. The time-scale for heating by viscous stirring is short with $\sim 10^3$ years, and hence one of the

main mechanisms for heating before larger bodies have formed. Later on, when a different mass spectrum can be applied to the disk, energy equipartition between more massive and less massive bodies becomes relevant known as dynamical friction. As a result, the mean eccentricity and inclination of planetesimals or protoplanets become mass dependent. Also the relative velocity between a protoplanet and a planetesimal becomes smaller while it is larger between two planetesimals of similar masses. This enhances collisions due to gravitational focusing by increasing the collisional cross-section of the protoplanet. Hence, dynamical friction plays an important role in understanding runaway growth and the formation of terrestrial planets.[1]
Gas drag becomes important only for smaller bodies to stay on almost circular orbits despite gravitational scattering. Together with dynamical friction that leads to a 'cooling' of the larger bodies, it acts against the heating imposed by viscous stirring by keeping the overall velocity dispersions low and hence, supports the effect of gravitational focusing. Additionally, inelastic collisions between smaller bodies, significant only for $\sigma > v_{\rm esc}$, lead to damping of velocity dispersions and hence, eccentricities and inclinations. This process therefore acts as an additional cooling mechanism but is less important than gas drag. The motion of planetesimals can also be excited by turbulent fluctuations of the gas. Larger bodies are no longer aerodynamically but can be gravitationally coupled to the gas. Disk turbulence, such as emerging from magneto-rotational instability, can change the local gas surface density and thereby create gravitational fluctuations that lead to excitation of the random velocities of planetesimals. It provides an additional heating mechanism that is yet not well investigated.[1]

After a few massive planetesimals or protoplanets have formed via runaway growth, the ongoing heating of smaller bodies by viscous stirring from protoplanets is only partially cooled by gas drag. This leads to a new phase, known as oligarchic growth, during which gravitational focusing is not that strong any more. It describes a stage in which the growth of protoplanets with respect to planetesimals dominates. The "isolated" protoplanets resume coagulation within their growing feeding zones. At the end of these two very fast growth phases (0.01 to 1 Myr) 10^2 to 10^3 bodies of masses ranging from 10^{-2} to 0.1 $M_\oplus$ will have formed within the terrestrial planet zone. Once dynamical friction can no longer maintain a low velocity dispersion due to the depletion of the planetesimal disk by the "oligarchs", strong interaction between the massive bodies starts and ends the prior isolated oligarchic growth. This final stage of planetary growth is characterized by chaotic conditions, large collisions and strong scattering of smaller objects and continues to at least 10 Myrs.[1]

1.7. Protoplanetary Atmospheres

After the runaway accretion of planetesimals has depleted the protoplanetary feeding zone, the evolution enters a phase where both dust and gas accretion are small and time-independent. This phase is the dominant determinant for the whole evolutionary time. When solid and gas masses become nearly equal, a runaway accretion of gas starts and results in the development of an initial dense atmosphere around the planet.[28, 21]
At the time of planetary formation the size distribution for dust in the disk has already changed significantly and it becomes even more different within a protoplanetary atmosphere. The destruction of in-falling planetesimals changes the amount of particles. Larger solid particles result

in a decrease of the opacity of the protoplanetary atmosphere. This decrease can be 3 orders in magnitude compared to the initially assumed interstellar opacity.[21] The in the following chapters described Mie Theory to compute scattering and absorption properties for compact particles becomes inaccurate since the assumption of spherical particle shapes is no longer valid for larger sizes.[3] A good representation to model the loss of this initial atmosphere for Earth-like planets on realistic time-scales, i.e. time-scales not comparable to the lifetime of the disk, becomes necessary.

Several authors modelling this final gas contraction on the protoplanet claim that it is very sensitive to opacity. A decrease in opacity is the key for a more rapid planet formation[28, 25]. Lower opacities lead to a more rapid heat loss which results in an earlier contraction of the protoplanetary envelope.[22]

Terrestrial planets should lose their primordial hydrogen/helium atmosphere which would be far too dense for the evolution of life as we know it. Processes within the atmosphere causing mass loss, i.e. heating of in-falling planetesimals, as well as ultraviolet and soft X-ray radiation from the host star after the depletion of the disk, determine the final amount of atmosphere.[33]

After the depletion of the gas disk around a protoplanet and a decrease in the temperature of the planet's core due to a decrease of in-falling planetesimals heating the core, the accumulated primordial atmosphere contracts and is exposed to the XUV radiation of the host star leading to thermal escape of the hydrogen envelope of the planet.[16, 33]

Considering the rough structure of a protoplanetary atmosphere, density will decrease with height. The lower atmosphere's temperature is determined by the planet's luminosity and hence, by the accretion rate of planetesimals on the planet's core. The atmosphere around the protoplanet can be divided into an optically thin envelope in the upper levels and an optically thick part near the surface. In the optically thin upper atmosphere absorption of stellar XUV radiation leads to ionization, dissociation and heating processes which in turn result in expansion and thermal escape of the upper hydrogen envelope. Only a minor part of the XUV radiation penetrates through the optically thick lower atmosphere. The vertical temperature gradient between the optically thin and thick region leads to a downward thermal energy flux. The amount of molecules will increase downwards to the optically thick region and hence, goes along with enhanced IR-cooling. This results in a temperature minimum near the boundary of the optically thin and thick layer.[16]

2. Theory

For the sake of simplicity, only the interaction of light with spherical compact homogeneous particles consisting of one material species, as well as spherical particle aggregates consisting of multiple species inclusions is treated in this thesis. Both can be described using Mie Theory since we assume sphericity. The optical constants of particle aggregates assuming different degrees of porosity can be calculated with the Effective Medium Theory (EMT). The porosity relates to the volume fraction of vacuum within the particle.

2.1. Mie Theory

Scattering of light by a particle depends on its shape, size, orientation and the optical properties of its composition, i.e. its optical constants. The electromagnetic field of a wave incident on a particle is defined by its electrical and magnetic components $\mathbf{E_i}$ and $\mathbf{H_i}$ with[3]

$$\mathbf{E_i} = \mathbf{E_0} \exp(i\mathbf{k} \cdot \mathbf{x} - i\omega t), \quad \mathbf{H_i} = \mathbf{H_0} \exp(i\mathbf{k} \cdot \mathbf{x} - i\omega t), \tag{2.1}$$

and must satisfy the Maxwell equations:[3]

$$\nabla \cdot \mathbf{E} = 0 \tag{2.2}$$

$$\nabla \cdot \mathbf{H} = 0 \tag{2.3}$$

$$\nabla \times \mathbf{E} = i\omega\mu\mathbf{H} \tag{2.4}$$

$$\nabla \times \mathbf{H} = -i\omega\epsilon\mathbf{E} \tag{2.5}$$

The incident field gives rise to an internal field $(\mathbf{E_1}, \mathbf{H_1})$ within the particle. The electromagnetic field surrounding the particle $(\mathbf{E_2}, \mathbf{H_2})$ can be expressed as the superposition of the incident and the scattered field $(\mathbf{E_s}, \mathbf{H_s})$:[3]

$$\mathbf{E_2} = \mathbf{E_i} + \mathbf{E_s}, \quad \mathbf{H_2} = \mathbf{H_i} + \mathbf{H_s} \tag{2.6}$$

To determine the scattering properties of a particle one must find solutions to the Maxwell equations for the field inside and outside the particle. They must also satisfy the boundary condition:[3]

$$[\mathbf{E_2}(\mathbf{x}) - \mathbf{E_1}(\mathbf{x})] \times \hat{\mathbf{n}} = 0, \quad [\mathbf{H_2}(\mathbf{x}) - \mathbf{H_1}(\mathbf{x})] \times \hat{\mathbf{n}} = 0 \tag{2.7}$$

$\hat{\mathbf{n}}$ is the unit vector pointing outward, normal to the particle surface S with $\mathbf{x}$ on S. The transition region between particle and medium forms a discontinuity requiring that the tangential components are continuous across that boundary.[3]

Due to the linearity of the Maxwell equations and the boundary condition the principle of superposition can be applied, i.e. if A and B are solutions to the equations, also their sum A+B is a solution. Therefore, considering scattering of a plane monochromatic wave is justified since any arbitrarily polarized wave can be understood as a superposition of plane waves of different polarization states.[3]

Any point in the particle can be described by a Cartesian coordinate system (see figure 12) with the z-axis defined by the incident light beam's direction of propagation, hence $\hat{\mathbf{e}}_\mathbf{z}$ pointing

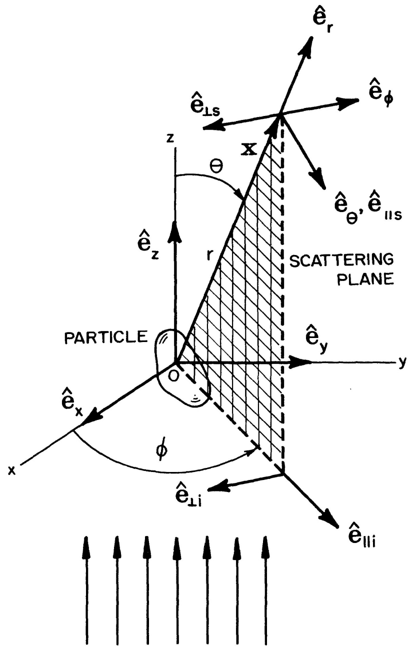

Figure 12: Scattering by an arbitrary particle (Bohren & Huffman,[3] 1983).

in forward direction, and forming an orthogonal system with x and y. The scattering plane is defined by the scattering direction $\hat{\mathbf{e}}_\mathbf{r}$ and $\hat{\mathbf{e}}_\mathbf{z}$ and is determined by the azimuthal angle Φ. The scattering angle Θ defines the angle between forward and scattering direction. The incident field $\mathbf{E_i}$ can be split into its two components parallel and normal to the scattering plane with the new defined unit vectors $\hat{\mathbf{e}}_{\|\mathbf{i}}$ and $\hat{\mathbf{e}}_{\perp\mathbf{i}}$ forming again an orthonormal basis with $\hat{\mathbf{e}}_\mathbf{z}$.[3]

$$\mathbf{E_i} = E_{\|\mathrm{i}}\hat{\mathbf{e}}_{\|\mathbf{i}} + E_{\perp\mathrm{i}}\hat{\mathbf{e}}_{\perp\mathbf{i}} \tag{2.8}$$

The same holds for the scattered field $\mathbf{E_s}$ in the far-field region ($kr \gg 1$) where $\mathbf{E_s}$ can be assumed being transverse to $\hat{\mathbf{e}}_\mathbf{r}$ with $\mathbf{E_s} \cdot \hat{\mathbf{e}}_\mathbf{r} = 0$.[3]

$$\mathbf{E_s} = E_{\|\mathrm{s}}\hat{\mathbf{e}}_{\|\mathbf{s}} + E_{\perp\mathrm{s}}\hat{\mathbf{e}}_{\perp\mathbf{s}} \tag{2.9}$$

The scattering direction $\hat{\mathbf{e}}_\mathbf{r}$ together with $\hat{\mathbf{e}}_\mathbf{\Phi}$ and $\hat{\mathbf{e}}_\mathbf{\Theta}$ are orthonormal basis vectors of the spherical coordinate system with the parallel component of the scattered field $\mathbf{E}_{\|\mathbf{s}}$ in direction $\hat{\mathbf{e}}_{\|\mathbf{s}} = \hat{\mathbf{e}}_\mathbf{\Theta}$ and $\mathbf{E}_{\perp\mathbf{s}}$ in direction $\hat{\mathbf{e}}_{\perp\mathbf{s}} = -\hat{\mathbf{e}}_\mathbf{\Phi}$. Because of the linearity of the boundary conditions the amplitude of the scattered field can be written as a linear function of the incident field:[3]

$$\begin{pmatrix} E_{\|\mathrm{s}} \\ E_{\perp\mathrm{s}} \end{pmatrix} = \frac{e^{ik(r-z))}}{-ikr} \begin{pmatrix} S_2 & S_3 \\ S_4 & S_1 \end{pmatrix} \begin{pmatrix} E_{\|\mathrm{i}} \\ E_{\perp\mathrm{i}} \end{pmatrix} \tag{2.10}$$

S_j are the complex elements of the amplitude scattering matrix that depend on azimuthal angle Φ and scattering angle Θ.[3]

2.1.1. Absorption and Scattering by a Sphere

The aim is to reduce the problem of finding solutions for the field equation to the simpler problem of finding solutions to the scalar wave equation. To start with, one can define vector functions *or* vector harmonics $\mathbf{M}$ and $\mathbf{N}$ with[3]

$$\mathbf{M} = \nabla \times (\mathbf{c}\Psi) \tag{2.11}$$

$$\mathbf{N} = \frac{\nabla \times \mathbf{M}}{k} \tag{2.12}$$

that satisfy the vector wave equation, are divergence-free (given for any function that is defined as a curl) and are proportional to the curl of each other. The generating function ψ is a scalar function, $\mathbf{c}$ is an arbitrary constant vector also called guiding *or* pilot vector. Since scattering by a sphere is the matter of interest and we seek solutions in spherical coordinates of the form $\psi(r,\theta,\phi) = R(r)\Theta(\theta)\Phi(\phi)$, the radius vector $\mathbf{r}$ is chosen as the guiding vector. The scalar wave equation is then[3]

$$\frac{1}{r^2}\frac{\partial}{\partial r}\left(r^2\frac{\partial\psi}{\partial r}\right) + \frac{1}{r^2\sin\theta}\frac{\partial}{\partial\theta}\left(\sin\theta\frac{\partial\psi}{\partial\theta}\right) + \frac{1}{r^2\sin\theta}\frac{\partial^2\psi}{\partial\phi^2} + k^2\psi = 0, \tag{2.13}$$

and split into its spherical components

$$\frac{d^2\Phi}{d\phi^2} + m^2\Phi = 0, \tag{2.14}$$

$$\frac{1}{\sin\theta}\frac{d}{d\theta}\left(\sin\theta\frac{d\Theta}{d\theta}\right) + \left[n(n+1) - \frac{m^2}{\sin^2\theta}\right]\Theta = 0, \tag{2.15}$$

$$\frac{d}{dr}\left(r^2\frac{dR}{dr}\right) + \left[k^2r^2 - n(n+1)\right]R = 0, \tag{2.16}$$

with m and n being separation constants determined by subsidiary conditions. Linearly independent and finite solutions at $\theta = 0$ and $\theta = \pi$ for equation 2.15 are provided by the associated orthogonal Legendre functions of the first kind, $P_{\mathrm{n}}^{\mathrm{m}}(\cos\theta)$ of degree n and order m. For equation 2.16 linearly independent solutions are the spherical Bessel functions z_{n}.[3]
The according generating functions with even (e) and odd (o) components are then:[3]

$$\psi_{\mathrm{emn}} = \cos m\phi P_{\mathrm{n}}^{\mathrm{m}}(\cos\theta) z_{\mathrm{n}}(kr) \tag{2.17}$$

$$\psi_{\mathrm{omn}} = \sin m\phi P_{\mathrm{n}}^{\mathrm{m}}(\cos\theta) z_{\mathrm{n}}(kr) \tag{2.18}$$

From these $\mathbf{M}_{emn}$, $\mathbf{M}_{omn}$, $\mathbf{N}_{emn}$ and $\mathbf{N}_{omn}$ can be generated. Any solution of the field equation can now be expanded into an infinite series of the vector spherical harmonics. A detailed derivation for the expansion of a plane wave in spherical harmonics is given by Bohren &

Huffman[3] (1983, p.89-93) and yields for the remaining case $m = 1$:

$$\mathbf{E}_i = E_0 \sum_{n=1}^{\infty} i^{\mathrm{n}} \frac{2n+1}{n(n+1)} (\mathbf{M}^{(1)}_{o1n} - i\mathbf{N}^{(1)}_{e1n}), \tag{2.19}$$

$$\mathbf{H}_i = \frac{-k}{\omega\mu} E_0 \sum_{n=1}^{\infty} i^{\mathrm{n}} \frac{2n+1}{n(n+1)} (\mathbf{M}^{(1)}_{o1n} - i\mathbf{N}^{(1)}_{e1n}) \tag{2.20}$$

For $m \neq 1$ all the coefficients vanish due to the orthogonality of the vector harmonics. For $\mathbf{H}_i$ the connection with $\mathbf{E}_i$ given in equation 2.4 is used. The superscript specifies the radial dependence of the generating functions with (1) being the first kind spherical Bessel function $j_{\mathrm{n}}(kr)$. This is required since the field is finite at the origin whereas the second kind spherical Bessel function $y_{\mathrm{n}}(kr)$ is rejected because of its infinity at the origin.[3]

2.1.2. Coefficients of the scattered and internal field

The internal and scattered fields can be expanded into[3]

$$\mathbf{E}_1 = \sum_{n=1}^{\infty} E_{\mathrm{n}} (c_{\mathrm{n}} \mathbf{M}^{(1)}_{o1n} - i d_{\mathrm{n}} \mathbf{N}^{(1)}_{e1n}), \tag{2.21}$$

$$\mathbf{H}_1 = \frac{-k_1}{\omega\mu_1} \sum_{n=1}^{\infty} E_{\mathrm{n}} (d_{\mathrm{n}} \mathbf{M}^{(1)}_{o1n} + i c_{\mathrm{n}} \mathbf{N}^{(1)}_{e1n}) \tag{2.22}$$

$$\mathbf{E}_s = \sum_{n=1}^{\infty} E_{\mathrm{n}} (i a_{\mathrm{n}} \mathbf{M}^{(3)}_{o1n} - b_{\mathrm{n}} \mathbf{N}^{(3)}_{e1n}), \tag{2.23}$$

$$\mathbf{H}_s = \frac{k}{\omega\mu_1} \sum_{n=1}^{\infty} E_{\mathrm{n}} (i b_{\mathrm{n}} \mathbf{M}^{(3)}_{o1n} + a_{\mathrm{n}} \mathbf{N}^{(3)}_{e1n}) \tag{2.24}$$

with $E_{\mathrm{n}} = i^{\mathrm{n}} E_0 (2n+1)/(n(n+1))$, μ_1 as the magnetic permeability of the sphere and k_1 as the wave number in the sphere. The superscript (3) in the expansion of the scattered field indicates that the spherical Bessel function of the third kind, also known as Hankel function $h^{(1)}_{\mathrm{n}}(kr) = j_{\mathrm{n}}(kr) + i y_{\mathrm{n}}(kr)$, with (1) corresponding to an outgoing spherical wave, describes the radial dependence of the generating functions.[3]
a_{n} and b_{n} are the scattering coefficients, c_{n} and d_{n} are the coefficients of the field inside the particle. From the boundary conditions four independent equations can be obtained for a given n that lead to the formulation of four linear equations from which the expansion coefficients can be derived:[3]

$$a_{\mathrm{n}} = \frac{\mu m^2 j_{\mathrm{n}}(mx)[x j_{\mathrm{n}}(x)]' - \mu_1 j_{\mathrm{n}}(x)[mx j_{\mathrm{n}}(mx)]'}{\mu m^2 j_{\mathrm{n}}(mx)[x h^{(1)}_{\mathrm{n}}(x)]' - \mu_1 h^{(1)}_{\mathrm{n}}(x)[mx j_{\mathrm{n}}(mx)]'}, \tag{2.25}$$

$$b_{\mathrm{n}} = \frac{\mu_1 j_{\mathrm{n}}(mx)[x j_{\mathrm{n}}(x)]' - \mu j_{\mathrm{n}}(x)[mx j_{\mathrm{n}}(mx)]'}{\mu_1 j_{\mathrm{n}}(mx)[x h^{(1)}_{\mathrm{n}}(x)]' - \mu h^{(1)}_{\mathrm{n}}(x)[mx j_{\mathrm{n}}(mx)]'}, \tag{2.26}$$

$$c_{\mathrm{n}} = \frac{\mu_1 j_{\mathrm{n}}(x)[xh_{\mathrm{n}}^{(1)}(x)]' - \mu_1 h_{\mathrm{n}}^{(1)}(x)[xj_{\mathrm{n}}(x)]'}{\mu_1 j_{\mathrm{n}}(mx)[xh_{\mathrm{n}}^{(1)}(x)]' - \mu h_{\mathrm{n}}^{(1)}(x)[mxj_{\mathrm{n}}(mx)]'}, \tag{2.27}$$

$$d_{\mathrm{n}} = \frac{\mu_1 m j_{\mathrm{n}}(x)[xh_{\mathrm{n}}^{(1)}(x)]' - \mu_1 m h_{\mathrm{n}}^{(1)}(x)[xj_{\mathrm{n}}(x)]'}{\mu m^2 j_{\mathrm{n}}(mx)[xh_{\mathrm{n}}^{(1)}(x)]' - \mu_1 h_{\mathrm{n}}^{(1)}(x)[mxj_{\mathrm{n}}(mx)]'} \tag{2.28}$$

Functions with a prime are derivatives with respect to the argument in brackets. $x = ka = 2\pi Na/\lambda$ is the size parameter depending on particle radius a and $m = \frac{k_1}{k} = \frac{N_1}{N}$ is the relative refractive index with N_1 being the refractive index of the particle and N of the medium.[3]
By the definition of the Riccati-Bessel functions with $\psi_{\mathrm{n}}(kr) = krj_{\mathrm{n}}(kr)$ and $\xi_{\mathrm{n}}(kr) = krh_{\mathrm{n}}^{(1)}(kr)$ the scattering coefficients (equations 2.25 and 2.26) simplify to[3]

$$a_{\mathrm{n}} = \frac{m\psi_{\mathrm{n}}(mx)\psi_{\mathrm{n}}'(x) - \psi_{\mathrm{n}}(x)\psi_{\mathrm{n}}'(mx)}{m\psi_{\mathrm{n}}(mx)\xi_{\mathrm{n}}'(x) - \xi_{\mathrm{n}}(x)\psi_{\mathrm{n}}'(mx)} \tag{2.29}$$

$$b_{\mathrm{n}} = \frac{\psi_{\mathrm{n}}(mx)\psi_{\mathrm{n}}'(x) - m\psi_{\mathrm{n}}(x)\psi_{\mathrm{n}}'(mx)}{\psi_{\mathrm{n}}(mx)\xi_{\mathrm{n}}'(x) - m\xi_{\mathrm{n}}(x)\psi_{\mathrm{n}}'(mx)} \tag{2.30}$$

2.1.3. Cross sections and efficiencies

The net rate of electromagnetic energy crossing a sphere with surface A can be written as[3]

$$W_{\mathrm{a}} = -\int_A \mathbf{S} \cdot \hat{\mathbf{e}}_{\mathbf{r}} dA \tag{2.31}$$

with the Poynting vector $\mathbf{S} = \mathbf{E} \times \mathbf{H}$ determining the magnitude and direction of the rate at which electromagnetic energy is transferred at all points in space - so it represents the electromagnetic energy flux density. The minus sign stands for the outward normal. If $W_{\mathrm{a}} > 0$ there is a net transfer of electromagnetic energy into the volume which means energy is absorbed by the particle. Therefore the index a indicating absorption is applied, and it holds $W_{\mathrm{a}} = W_{\mathrm{i}} - W_{\mathrm{s}} + W_{\mathrm{ext}}$. Because $W_{\mathrm{i}} = -\int_A \mathbf{S_i} \cdot \hat{\mathbf{e}}_{\mathbf{r}} dA$ vanishes in a non-absorbing medium, the rate at which energy is extinct across the surface A is the sum of the rate of energy scattered and the rate of energy absorbed:[3]

$$W_{\mathrm{ext}} = W_{\mathrm{s}} + W_{\mathrm{a}} \tag{2.32}$$

The cross sections are defined as the ratio of the rate of energy extinct, absorbed or scattered to the incident irradiation:[3]

$$C_{\mathrm{ext}} = \frac{W_{\mathrm{ext}}}{I_i}, \quad C_{\mathrm{sca}} = \frac{W_{\mathrm{s}}}{I_{\mathrm{i}}}, \quad C_{\mathrm{abs}} = \frac{W_{\mathrm{a}}}{I_{\mathrm{i}}} \tag{2.33}$$

The efficiencies can be understood as dimensionless cross sections in being the ratio of the cross section to the particle's cross-sectional area projected onto a plane normal to the incident beam,

$G = \pi a^2$ with a as the radius of a sphere:[3]

$$Q_{\text{ext}} = \frac{C_{\text{ext}}}{G}, \quad Q_{\text{sca}} = \frac{C_{\text{sca}}}{G}, \quad Q_{\text{abs}} = \frac{C_{\text{abs}}}{G} \tag{2.34}$$

Following chapter 3.4 of Bohren & Huffman[3] (1983) that gives additional information to the above roughly defined quantities as well as chapter 4.4.1 in calculating the net rate W_a in a non-absorbing surrounding medium, a more applicable description is given for the cross sections:

$$C_{\text{sca}} = \frac{2\pi}{k^2}\sum_{n=1}^{\infty}(2n+1)(|a_{\text{n}}|^2 + |b_{\text{n}}|^2) \tag{2.35}$$

$$C_{\text{ext}} = \frac{2\pi}{k^2}\sum_{n=1}^{\infty}(2n+1)\Re\{a_{\text{n}} + b_{\text{n}}\} \tag{2.36}$$

It follows from the relations in 2.34 and the introduction of the size parameter $x = kr = \frac{2\pi r}{\lambda}$:[3]

$$Q_{\text{sca}} = \frac{2}{x^2}\sum_{n=1}^{\infty}(2n+1)(|a_{\text{n}}|^2 + |b_{\text{n}}|^2) \tag{2.37}$$

$$Q_{\text{ext}} = \frac{2}{x^2}\sum_{n=1}^{\infty}(2n+1)\Re\{a_{\text{n}} + b_{\text{n}}\} \tag{2.38}$$

$\Re\{\}$ is the real part of the argument.

2.1.4. Radiation pressure efficiency

Light carries energy and momentum. The latter is defined as the ratio of energy to the speed of light. Due to extinction momentum will be removed from the initial light beam. The momentum removed by absorption will not be replaced whereas the scattered part of momentum carried in the forward scattered radiation still needs to be accounted for.[34]
The total momentum of the forward scattered radiation is proportional to $<\cos\theta>C_{\text{sca}}$ with $<\cos\theta>=\beta$ being the mean of $\cos\theta$ weighted by the scattering function, called the asymmetry parameter. The removed part of the forward momentum that is not replaced by the forward momentum of the scattered light is proportional to the radiation pressure cross section that is defined as:[34]

$$C_{\text{pr}} = C_{\text{ext}} - \beta C_{\text{sca}} \tag{2.39}$$

Hence, in contrast to the extinction cross section, the radiation pressure cross section still includes the energy/momentum of the forward scattered light that is not removed from the light beam.[34] It therefore can be applied as a corrected extinction cross section including anisotropic scattering.[26, 27, 13]
Analogue to this, the radiation pressure efficiency is[26, 13]

$$Q_{\text{pr}} = Q_{\text{ext}} - \beta Q_{\text{sca}} = Q_{\text{ext}}(1-\omega\beta) \tag{2.40}$$

with $\omega = \frac{Q_{\mathrm{sca}}}{Q_{\mathrm{ext}}}$ being the scattering albedo. Like already mentioned the factor $(1 - \omega\beta)$ gives a correction for anisotropic scattering. $\beta = 0$ is for isotropic, i.e. Rayleigh scattering, and $\beta = 1$ for totally forward scattering.[26, 13]

2.1.5. Mass attenuation coefficient

The attenuation or extinction coefficient in equation 1.1 is of course a function of the cross section and is defined for a single particle species j as

$$\kappa_{\mathrm{ext,j}} = \Upsilon_{\mathrm{j}} C_{\mathrm{ext,j}} = \Upsilon_{\mathrm{j}}(C_{\mathrm{abs,j}} + C_{\mathrm{sca,j}}) \tag{2.41}$$

with Υ_{j} being the number of particles per unit volume. The total attenuation coefficient is then the sum of all individual particle coefficients $\kappa_{\mathrm{ext,j}}$:

$$\kappa_{\mathrm{ext}} = \sum_{j} \Upsilon_{\mathrm{j}} C_{\mathrm{ext,j}} \tag{2.42}$$

Relating $\kappa_{\mathrm{ext,j}}$ to a volume (for the sake of better illustration the index j is neglected) we obtain

$$\kappa_{\mathrm{ext,v}} = \frac{f C_{\mathrm{ext}}}{v} \tag{2.43}$$

with $f = 1/\Upsilon$ being the volume fraction of particles in the medium and v being the volume of a single particle.[3] The mass attenuation or mass extinction coefficient can then be written as

$$\kappa_{\mathrm{ext,m}} = \frac{f}{\rho} \frac{C_{\mathrm{ext}}}{v} \tag{2.44}$$

with ρ as the density of the particle.[3]
It is important to note that the extinction cross section per unit volume C_{ext}/v or mass $C_{\mathrm{ext}}/\rho v$ provides more physical information than the extinction efficiency Q_{ext} which only describes the cross section over an unit area. Strictly said, rather a quantity defined over an unit volume or mass should be called efficiency. Hence, it often makes more sense to plot $C_{\mathrm{ext}}/v = 3Q_{\mathrm{ext}}/4r$ as a function of size instead of Q_{ext} alone.[3]

2.2. Effective Medium Theory

With the help of the Maxwell-Garnett Effective Medium Theory we can calculate the average dielectric function ϵ of certain material compositions consisting of inclusions embedded in a medium with ϵ_{m}.[3, 6] Beside the complex refractive index, the complex dielectric function or complex dielectric constant $\epsilon = \epsilon' + i\epsilon''$ provides another set of quantities that describe the optical properties of a material. They are derived from the Lorentz model in which electrons and ions are treated as simple harmonic oscillators that are excited by radiation.[3] The relation between dielectric constant and complex refractive index $N = n + ik$ is given with[3, 6]

$$\epsilon' + i\epsilon'' = (n + ik)^2. \tag{2.45}$$

The average dielectric function ϵ of a spherical inclusion with ϵ_0 embedded in a homogeneous medium with ϵ_{m} is defined as[6]

$$\epsilon = \epsilon_{\mathrm{m}} \left[1 + 3f_{\mathrm{v}} \left(\frac{\epsilon_0 - \epsilon_{\mathrm{m}}}{\epsilon_0 + 2\epsilon_{\mathrm{m}}} \right) \left(1 - f_{\mathrm{v}} \left(\frac{\epsilon_0 - \epsilon_{\mathrm{m}}}{\epsilon_0 + 2\epsilon_{\mathrm{m}}} \right) \right)^{-1} \right] \tag{2.46}$$

with f_{v} being the particle volume fraction of the inclusion. The Garnett EMT equation can be generalized for aggregates containing multiple inclusions of species j embedded in vacuum, hence ϵ_{m}=1.

Following Cuzzi et al.[6] (2014) it yields after separation of complex and imaginary parts:

$$\epsilon = \epsilon' + i\epsilon'' = \frac{1 + 2\sum_{\mathrm{j}} f_{\mathrm{vj}}\sigma_{\mathrm{j}} + i6\sum_{\mathrm{j}} f_{\mathrm{vj}}\gamma_{\mathrm{j}}}{1 - \sum_{\mathrm{j}} f_{\mathrm{vj}}\sigma_{\mathrm{j}} - i3\sum_{\mathrm{j}} f_{\mathrm{vj}}\gamma_{\mathrm{j}}} \tag{2.47}$$

with

$$\sigma_{\mathrm{j}} = \frac{(n_{\mathrm{j}}^2 - k_{\mathrm{j}}^2 - 1)(n_{\mathrm{j}}^2 - k_{\mathrm{j}}^2 + 2) + 4n_{\mathrm{j}}^2 k_{\mathrm{j}}^2}{(n_{\mathrm{j}}^2 - k_{\mathrm{j}}^2 + 2)^2 + 4n_{\mathrm{j}}^2 k_{\mathrm{j}}^2} \tag{2.48}$$

and

$$\gamma_{\mathrm{j}} = \frac{2n_{\mathrm{j}}k_{\mathrm{j}}}{(n_{\mathrm{j}}^2 - k_{\mathrm{j}}^2 + 2)^2 + 4n_{\mathrm{j}}^2 k_{\mathrm{j}}^2} \tag{2.49}$$

already transformed to being a function of (n,k) instead of (ϵ',ϵ'') according to relation 2.45.

The average complex refractive index is then obtained via[6]

$$N = n + ik = \left[\frac{\sqrt{\epsilon'^2 + \epsilon''^2} + \epsilon'}{2} \right]^2 + i \left[\frac{\sqrt{\epsilon'^2 + \epsilon''^2} - \epsilon'}{2} \right]^2. \tag{2.50}$$

The average mass density ρ of a composite particle depends on its porosity ϕ and the solid average particle density $\bar{\rho}$ with[6]

$$\rho = (1 - \phi)\bar{\rho}. \tag{2.51}$$

The total particle volume fraction of inclusions is given with $f_{\mathrm{v}} = \sum_{\mathrm{j}} f_{\mathrm{vj}} = 1 - \phi$. It is defined for an inclusion of species j with[6]

$$f_{\mathrm{vj}} = \frac{v_{\mathrm{j}}}{V} = \frac{m_{\mathrm{j}}}{\rho_{\mathrm{j}} V} = \frac{\rho \alpha_{\mathrm{j}}}{\rho_{\mathrm{j}} \alpha} = \frac{(1-\phi)\bar{\rho}\alpha_{\mathrm{j}}}{\rho_{\mathrm{j}} \alpha}. \tag{2.52}$$

The total mass fraction of all species j per disk gas mass, later indicated as f (see equation 2.73), is here defined as α to avoid confusion with the particle volume fraction f_{v}.
It therefore holds for the solid particle density[6]

$$\bar{\rho} = \frac{\alpha}{\sum_{\mathrm{j}} (\alpha_{\mathrm{j}} / \rho_{\mathrm{j}})}. \tag{2.53}$$

After deriving average complex refractive indices for aggregates of different composition or porosity, Mie Theory can again be used to determine their optical properties like efficiencies and asymmetry factors. Although, one has in general to be careful when assuming aggregates of large particle sizes which are no longer spherical and influence the amount of forward scattered light by enhanced diffraction and hence, the asymmetry parameter becomes (g=cos θ=1), making the total extinction being dominated by absorption for particle sizes $r \ll \lambda$.[6]

2.3. Rosseland Mean Opacity

A derivation for the Rosseland mean opacity is given by Clayton (1968)[5]. It descends from the radiative transfer equation which can be defined by introducing the radiation field intensity as the integral over the specific intensity depending on the direction angle θ in the frequency interval $d\nu$:[5]

$$I(\theta) = \int_0^\infty I_\nu(\theta) d\nu \tag{2.54}$$

As mentioned in the chapters before, a light beam traversing a medium of thickness ds and density ρ can be weakened due to extinction. This change of the specific intensity dI_ν can be written separately for the two mechanisms causing it, namely scattering and absorption:[5]

$$dI_{\nu,\mathrm{abs}} = -\kappa_{\nu,\mathrm{abs}} \rho I_\nu ds, \quad dI_{\nu,\mathrm{sca}} = -\kappa_{\nu,\mathrm{sca}} \rho I_\nu ds \int_{\Omega'} p(\cos\theta') \frac{d\Omega'}{4\pi} \tag{2.55}$$

κ defines the according coefficient for absorption (abs) or scattering (sca), θ' is the angle of scattered radiation relative to the direction angle. The scattering phase function $p(\cos\theta')$ describes the angular distribution of the energy removed by scattering and is normalized, so that the integral on the right hand side of the second equation in 2.55 becomes 1. For isotropic scattering, $p(\cos\theta') = 1$, the removed energy due to scattering is equally redistributed to all solid angles $d\Omega'$. Because of the definition of the phase function, its integral over all solid angles being unity, it is a needless complexity when calculating the change in specific intensity. However, it is needed for the computation of the amount of energy scattered into the beam.[5]
Accordingly, the total change in the specific intensity due to scattering and absorption becomes:[5]

$$dI_\nu = -(\kappa_{\nu,\mathrm{abs}} + \kappa_{\nu,\mathrm{sca}}) \rho I_\nu ds \tag{2.56}$$

In addition to extinction also emission occurs and increases the specific intensity:[5]

$$dI_\nu(\theta) = +j_\nu(\theta) \rho ds \tag{2.57}$$

The emission term of radiative transfer is simplified by the assumption of local thermodynamic equilibrium. A small temperature gradient sustains this assumption.[5]
For the further definition of the emission coefficient $j_\nu(\theta)$ we assume a thin slab of thickness dx and an unit cross-sectional area with an energy absorption rate of[5]

$$dE_\nu(\theta) = -\kappa_{\nu,\mathrm{abs}} \rho dl I_\nu(\theta) \cos\theta, \tag{2.58}$$

with $dl = dx/\cos\theta$ being the absorbing path length of the slab and $I_\nu \cos\theta$ taking into account the inclination angle of the impinging specific intensity. It can then be rewritten by the integral over all solid angles[5]

$$dE_\nu(\theta) = -\kappa_{\nu,\mathrm{abs}} \rho dx \int I_\nu(\theta) d\Omega = -\kappa_{\nu,\mathrm{abs}} \rho dx c u_\nu, \tag{2.59}$$

using the relation $\int I_\nu(\theta) d\Omega = c u_\nu$, with u_ν as the radiation energy density of frequency ν per unit frequency interval and c as the speed of light. Since $dm = \rho dx$ it follows for the energy absorption rate per unit mass:[5]

$$\frac{dE_\nu}{dm} = -\kappa_{\nu,\text{abs}} c u_\nu \tag{2.60}$$

For local thermodynamic equilibrium and hence, a balance between emission and absorption, known as Kirchoff's law, we get[5]

$$j_\nu(\theta) = \kappa_{\nu,\text{abs}} \frac{c u_\nu}{4\pi} = \kappa_{\nu,\text{abs}} B_\nu(T). \tag{2.61}$$

Since the emission coefficient $j_\nu(\theta)$ is defined per unit solid angle and isotropic in local thermodynamic equilibrium, the factor 4π is applied. The source *or* Planck function for emission in thermodynamic equilibrium *or* Black Body radiation is defined as:[5]

$$B_\nu(T) = \frac{2h\nu^3}{c^2} \frac{1}{\exp(h\nu/kT) - 1}, \tag{2.62}$$

T is the temperature, h is the Planck constant and k is the Boltzmann constant.[5]
There are different forms of emission. Spontaneous emission results only from the temperature of the material. Induced emission is caused by transitions in atoms exerted to a radiation field. The probability of this downward transitions is described by the Einstein coefficient B_{ij}. This effect produces radiation having the same frequency and propagation direction as the incident light. The fraction of the spontaneous to total emission can be derived with the help of the Einstein coefficients and yields:[5]

$$\frac{\textit{spontaneous emission}}{\textit{total emission}} = 1 - e^{-h\nu/kT} \tag{2.63}$$

There are also mechanisms other than transitions between discrete atomic states like for example ionization in the case of absorption, and its inverse process accounting for emission, radiative recombination. The ratio of spontaneous to total emission by recombination is the same as in equation 2.63.[5]
While the spontaneous emission determined solely by the temperature of the material depends on the source function $B_\nu(T)$ also in non-thermodynamic equilibrium conditions, the induced emission does not. It is then proportional to the actual specific radiation intensity:[5]

$$j_\nu(\theta) = \kappa_{\nu,\text{abs}}(1 - e^{-h\nu/kT}) B_\nu(T) + \kappa_{\nu,\text{abs}} e^{-h\nu/kT} I_\nu(\theta) \tag{2.64}$$

Photons scattered into the beam must also be considered. The energy scattered per unit solid angle into the beam propagating in the direction (θ, ϕ) from another cone specified by (θ', ϕ') is[5]

$$j_{\nu,\text{sca}} = \kappa_{\nu,\text{sca}} \frac{1}{4\pi} \int^{\pi} \int^{2\pi} p(\theta, \phi; \theta', \phi') I_\nu(\theta', \phi') \sin\theta' d\theta' d\phi'. \tag{2.65}$$

$p(\theta, \phi; \theta', \phi')$ is the scattering phase function between the light beam (θ, ϕ) and any other cone or pencil (θ', ϕ').[5]

We can now establish an energy balance for a small cylinder with unit cross section and coaxial length dl, by demanding that the radiation leaving the top of the cylinder equals the radiation entering at the bottom minus the absorption within and plus the emission entering from outside:[5]

$$\begin{aligned} I_\nu(r+dr,\theta) - I_\nu(r,\theta) = \frac{\partial I_\nu}{\partial r}dr = \\ &- (\kappa_{\nu,\mathrm{abs}} + \kappa_{\nu,\mathrm{sca}})I_\nu(r,\theta)\rho dl + \kappa_{\nu,\mathrm{abs}}(1-e^{-h\nu/kT})B_\nu(T)\rho dl \\ &+ \kappa_{\nu,\mathrm{abs}}e^{-h\nu/kT}I_\nu(r,\theta)\rho dl \\ &+ \kappa_{\nu,\mathrm{sca}}\frac{\rho dl}{4\pi}\int^{\Omega'} p(\theta,\phi;\theta',\phi')I_\nu(r,\theta',\phi')d\Omega' \end{aligned} \tag{2.66}$$

Dividing through the total mass ρdl and defining $\kappa^*_{\nu,\mathrm{abs}} = \kappa_{\nu,\mathrm{abs}}(1-e^{-h\nu/kT})$, as well as using the relation $dr/dl = \cos\theta$, yields the radiative transfer equation for a plane parallel atmosphere in local thermodynamic equilibrium:[5]

$$\begin{aligned} \frac{1}{\rho}\frac{\partial I_\nu}{\partial r}\cos\theta = &- (\kappa^*_{\nu,\mathrm{abs}} + \kappa_{\nu,\mathrm{sca}})I_\nu(r,\theta) + \kappa^*_{\nu,\mathrm{abs}}B_\nu(T) \\ &+ \kappa_{\nu,\mathrm{sca}}\frac{1}{4\pi}\int^{\Omega'} p(\theta,\phi;\theta',\phi')I_\nu(r,\theta',\phi')d\Omega' \end{aligned} \tag{2.67}$$

We further multiply by $\cos\theta$ and integrate over all solid angles $d\Omega$. The single terms (I)-(IV) then become:[5]

$$\begin{aligned} (I) \quad & \frac{1}{\rho}\frac{\partial}{\partial r}\int I_\nu \cos^2\theta d\Omega = \frac{c}{\rho}\frac{\partial P_\nu}{\partial r} \\ (II) \quad & \int (\kappa^*_{\nu,\mathrm{abs}} + \kappa_{\nu,\mathrm{sca}})I_\nu \cos\theta d\Omega = -(\kappa^*_{\nu,\mathrm{abs}} + \kappa_{\nu,\mathrm{sca}})H_\nu \\ (III) \quad & \int \kappa^*_{\nu,\mathrm{abs}}B_\nu(T)\cos\theta d\Omega = 0 \\ (IV) \quad & \kappa_{\nu,\mathrm{sca}}\frac{1}{4\pi}\int_\Omega\int_{\Omega'} \cos\theta p(\theta,\phi;\theta',\phi')I_\nu(r,\theta',\phi')d\Omega d\Omega' \end{aligned} \tag{2.68}$$

P_ν is the radiation pressure that still equals the energy density u_ν with a factor $\frac{1}{3}$, even if the radiation field is slightly anisotropic. H_ν is the monochromatic heat flux per unit area.[5]
One can check the relations used in the terms (I) and (II) in Clayton (1968)[5] (p. 107-108) stating that the energy density u, the net flux of energy or heat flux H and the radiation pressure P_r are related to the three moments of the radiation field $I(\theta)$. The term (III) vanishes since the source function $B_\nu(T)$ is isotropic and hence, its integral over all solid angles becomes 0.[5]
The integral in (IV) vanishes if the scattering phase function contains only even powers of the cosine. Holding θ' and ϕ' fixed, one can assume the integral over $d\Omega$ as the sum of light beams in the direction θ and the direction opposite to it. So, p will have the same value for both while the cosine will take equal but opposite values and hence, the integral will vanish.[5]

So only terms (I) and (II) remain. Furthermore, the total heat flux per unit area is

$$H = \int_0^\infty H_\nu d\nu = -\frac{c}{3\rho}\int_0^\infty \frac{1}{\kappa^*_{\nu,\mathrm{abs}} + \kappa_{\nu,\mathrm{sca}}}\frac{du_\nu}{dr}d\nu = -\frac{c}{3\rho}\int_0^\infty \frac{1}{\kappa^*_{\nu,\mathrm{abs}} + \kappa_{\nu,\mathrm{sca}}}\frac{du_\nu}{dT}\frac{dT}{dr}d\nu, \tag{2.69}$$

using $\frac{du_\nu}{dr} = \frac{du_\nu}{dT}\frac{dT}{dr}$ since in local thermodynamic equilibrium the energy density is only a function of temperature. The temperature gradient is independent of frequency and hence, can be written outside the integral. Normalization by the integral $\int_0^\infty \frac{du_\nu}{dT}d\nu = \frac{d}{dT}\int u_\nu d\nu = \frac{du}{dT} = 4aT^3$, with a being a constant then yields:[5]

$$H = -\frac{4ac}{3\rho}T^3\frac{dT}{dr}\frac{\int_0^\infty \frac{1}{\kappa^*_{\nu,\mathrm{abs}}+\kappa_{\nu,\mathrm{sca}}}\frac{du_\nu}{dT}d\nu}{\int_0^\infty \frac{du_\nu}{dT}d\nu} \tag{2.70}$$

Since in local thermodynamic equilibrium $u_\nu \propto B_\nu(T)$[5], we can replace it in the integrals and introduce the Rosseland mean opacity κ_R as the inverse of the last term[26, 13]:

$$\kappa_\mathrm{R} = \frac{\int_0^\infty \frac{\partial B_\nu(T)}{\partial T}d\nu}{\int_0^\infty \frac{1}{<\kappa_{\nu,\mathrm{pr}}>}\frac{\partial B_\nu(T)}{\partial T}d\nu} \tag{2.71}$$

with

$$\int_0^\infty \frac{\partial B_\nu(T)}{\partial T}d\nu = \frac{\partial B(T)}{\partial T} = \frac{4\sigma}{\pi}T^3 \tag{2.72}$$

Instead of $\kappa_{\nu,\mathrm{ext}} = \kappa^*_{\nu,\mathrm{abs}} + \kappa_{\nu,\mathrm{sca}}$ the radiation pressure coefficient $<\kappa_{\nu,\mathrm{pr}}>$, defined as sum over all coefficients of the individual grain species j present in the considered medium, is used:[26, 13]

$$< \kappa_{\nu,\mathrm{pr}} > = \sum_{j=1}^{J} f_\mathrm{j}\kappa^\mathrm{j}_{\nu,\mathrm{pr}} \tag{2.73}$$

with f_j being the mass fraction of species j and

$$\kappa^\mathrm{j}_{\nu,\mathrm{pr}} = \frac{1}{d_\mathrm{j}}\frac{\int_0^\infty n_\mathrm{j}(r)r^3\frac{C^j_{\nu,\mathrm{pr}}(r)}{v_\mathrm{j}}dr}{\int_0^\infty n_\mathrm{j}(r)r^3 dr} \tag{2.74}$$

following equation 2.44. Like mentioned in chapter 2.1.4 the radiation pressure coefficient follows from conservation of momentum[34] and constitutes a corrected extinction coefficient including anisotropic scattering.
A size distribution function $n_\mathrm{j}(r)$ that takes into account the different size spectrum of particles for each species j is introduced, redefining $\kappa^\mathrm{j}_{\nu,\mathrm{pr}}$ as averages over their grain size distribution. $C^j_{\nu,\mathrm{pr}}$ is the radiation pressure cross section depending on radius and frequency of the incident light, d_j is the density of species j. According to the relation between $C^j_{\nu,\mathrm{pr}}$ and the radiation pressure efficiency $Q^j_{\nu,\mathrm{pr}}$ (see equation 2.34), one can rewrite $\kappa^\mathrm{j}_{\nu,\mathrm{pr}}$ as a function of the

latter:[26, 13]

$$\kappa^{\mathrm{j}}_{\nu,\mathrm{pr}} = \frac{3}{4d_{\mathrm{j}}} \frac{\int_0^\infty n_{\mathrm{j}}(r) r^2 Q^{j}_{\nu,\mathrm{pr}}(r) dr}{\int_0^\infty n_{\mathrm{j}}(r) r^3 dr} \tag{2.75}$$

Smaller monochromatic opacities are stronger weighted in the Rosseland mean opacity than larger ones. This represents a situation where more radiation travels through a medium where opacity is smaller. The Rosseland mean is used in optically thick regions.[30]

2.4. Planck Mean Opacity

The Planck mean opacity is the opacity weighted by the black body intensity, and defined as[30]:

$$\kappa_{\mathrm{P}} = \frac{\int_0^\infty < \kappa_{\nu,\mathrm{pr}} > B_\nu(T) d\nu}{\int_0^\infty B_\nu(T) d\nu} = \frac{\int_0^\infty < \kappa_{\nu,\mathrm{pr}} > B_\nu(T) d\nu}{B(T)} = \frac{\pi}{\sigma T^4} \int_0^\infty < \kappa_{\nu,\mathrm{pr}} > B_\nu(T) d\nu \tag{2.76}$$

It is applicable in optically thin media. In contrast to the Rosseland mean opacity, high $\kappa(\nu)$ contribute most to the Planck mean opacity.

3. Computational Methods

3.1. Mean Opacity Code

In programming the monochromatic and mean opacities for assumed mixtures of dust (see section 4.2), I followed the methods explained by Pollack et al.[26, 27] (1985, 1994) and by Henning & Stognienko[13] (1994). Abbreviations are made concerning the Mie Theory code used and the applied integration method.

First of all, as can be seen from equation 2.75, the radiation pressure efficiency for each single predefined particle radius r and frequency ν must be computed. For the calculation of extinction and scattering efficiencies, as well as the asymmetry parameter, I used an already existing Mie Theory code, called Mie.m[17, 18, 39]. This MATLAB code is programmed according to the Fortran code CALLBH.f[40] from Bohren & Huffman[3] (1983). A matrix $\mathbf{Q}_{\mathrm{j}}(\nu,\mathbf{r})$ is then calculated for every material at frequencies at which optical constants/complex refractive indices are defined, and for particle sizes of a predefined vector $\mathbf{r}$. This vector $\mathbf{r}$ is generated with 50 logarithmic intervals, each consisting again of 51 equidistant sampling points. Afterwards, $\mathbf{Q}_{\mathrm{j}}$ is linearly interpolated to frequencies ν for which no optical constants are provided. The vector ν is generated the same way as $\mathbf{r}$ but with a higher resolution, having 100 logarithmic defined intervals with 101 equidistant points within.

The integrals in equation 2.75 are obtained by summing over n sub-integrations, carried out for each logarithmic interval (r_i, r_{i+1}) in $\mathbf{r}$, with $i = 0, 1, ...n-1$. For this, numerical integration with 1/3 Simpson's rule over N+1 equidistant points $(r_{i,0}, r_{i,1}, ..., r_{i,N})$, in between the logarithmic subintervals (r_i, r_{i+1}), was used. The last sampling point is always equal to the first in the new subinterval: $r_{i,N} = r_{i+1,0}$ (see figure 13).
This method was used to cover also very small radii and prevent from doing a complete logarithmic numerical integration, in which all formulas must be logarithmized and become quite long and confusing. Hence, this facilitates the occurrence of errors. The consistency of the scheme is checked in section 5.1.4 by comparing it to results from just one numerical integration with 1/3

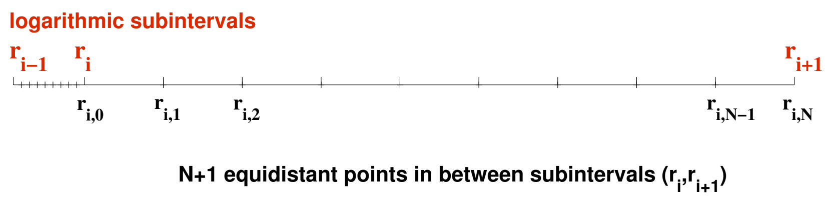

Figure 13: Sketch for construction of the particle size vector $\mathbf{r}$ consisting of n logarithmic subintervals (red) with $N+1$ equidistant sample points in between (black).

Simpson's rule, with n equidistant sample points over the whole interval $r_0, r_{\mathrm{n}-1}$. Of course, here a much higher resolution, i.e. more sample points n, is/are needed.
Following Pollack et al.[26, 27] (1985, 1994) and Henning & Stognienko[13] (1994), the monochromatic opacities $\kappa_{\mathrm{j}}(\nu)$ are then multiplied by their specified mass fractions f_{j} and summed up to $\kappa(\nu)$ over each particle species j existing in the specified temperature and density range of the medium. The medium density ρ_m is only represented in the mean opacity via the vaporization temperature of the particle species:

$$f_{\mathrm{j}} = \begin{cases} f_{\mathrm{j}}, & T \leq T_{\mathrm{vap}}(\rho_{\mathrm{m}}) \\ 0, & T > T_{\mathrm{vap}}(\rho_{\mathrm{m}}) \end{cases} \tag{3.1}$$

For the integrals in equation 2.71 for the Rosseland and equation 2.76 for the Planck mean opacities, the same method like for the integrals in equation 2.75 is used.
Regarding composite particles of different porosity, I followed the equations derived by Cuzzi et al.[6] (2014) in section 2.2. Optical properties for the new, via Garnett Effective Medium Theory computed, average refractive indices were again obtained with Mie Theory, although the assumption of sphericity is no longer entirely valid for the large particle radii in question, i.e. from micron sizes up to 1 cm.

3.2. Mie Code

To compute the extinction, scattering and radiation pressure efficiencies I used an external full Mie Theory code. Unfortunately, I could not obtain or reproduce the Mie code used by Pollack et al. (1985, 1994)[26, 27] since in their previous papers no information was provided for re-computation. The difference in results arising from this circumstance is not a small one, and is demonstrated in section 5.1.2. To check the external code for errors, I also provide a comparison with the traditional Mie Theory code BHMIE.f[40], presented in section 5.1.3 from Bohren & Huffman[3] (1983).

3.2.1. Mie.m

The MATLAB code provided by Maetzler[17, 18, 39] (2002a,b) is based on BHMIE.f[40]. Accordingly, the following steps for the calculation of extinction, scattering, absorption efficiencies and asymmetry parameter are implemented.
For the truncation of the infinite series after $n_{\max}$ terms the following criteria for stability is given by Bohren & Huffman[3] (1983), according to Wiscombe[37] (1980):

$$n_{\max} = x + 4x^{1/3} + 2 \tag{3.2}$$

With the recurrence relations[3]

$$\psi_{\mathrm{n}}'(x) = \psi_{\mathrm{n}-1}(x) - \frac{n\psi_{\mathrm{n}}(x)}{x}, \quad \xi_{\mathrm{n}}'(x) = \xi_{\mathrm{n}-1}(x) - \frac{n\xi_{\mathrm{n}}(x)}{x}, \tag{3.3}$$

and the logarithmic derivative that also satisfies the recurrence relation (since the Bessel functions also do)[3]

$$D_{\mathrm{n}}(mx) = \frac{d}{d(mx)} \ln \psi_{\mathrm{n}}(mx), \quad D_{\mathrm{n}-1} = \frac{n}{mx} - \frac{1}{D_{\mathrm{n}} + n/(mx)} \tag{3.4}$$

the equations for the scattering coefficients (2.29, 2.30) transform to a more computable form used in the MATLAB code:[3, 39]

$$a_{\mathrm{n}} = \frac{[D_{\mathrm{n}}(mx)/m + n/x]\psi_{\mathrm{n}}(x) - \psi_{\mathrm{n}-1}(x)}{[D_{\mathrm{n}}(mx)/m + n/x]\xi_{\mathrm{n}}(x) - \xi_{\mathrm{n}-1}(x)} \tag{3.5}$$

$$b_{\mathrm{n}} = \frac{[mD_{\mathrm{n}}(mx)/m + n/x]\psi_{\mathrm{n}}(x) - \psi_{\mathrm{n}-1}(x)}{[mD_{\mathrm{n}}(mx)/m + n/x]\xi_{\mathrm{n}}(x) - \xi_{\mathrm{n}-1}(x)} \tag{3.6}$$

For the calculation of $D_{\mathrm{n}}(mx)$ a downward scheme is used since it is more stable. This is due to the downward stability of the spherical Bessel function j_{n}.[3] The spherical Bessel functions are the Bessel functions of first and second kind J_{n} and Y_{n}, respectively, and multiplied by a factor:[3]

$$j_{\mathrm{n}}(x) = \sqrt{\frac{\pi}{2x}} J_{\mathrm{n}+1/2}(x), \quad y_{\mathrm{n}}(x) = \sqrt{\frac{\pi}{2x}} Y_{\mathrm{n}+1/2}(x) \tag{3.7}$$

The first orders are given with[3]

$$j_0(x) = \frac{\sin x}{x}, \quad y_0(x) = -\frac{\cos x}{x}. \tag{3.8}$$

After the calculation of the scattering coefficients with equations 3.5 and 3.6 with the MATLAB function Mie_ab.m called in Mie.m, the efficiencies Q_{sca}, Q_{ext}, Q_{abs} are computed using equations 2.37 and 2.38, as well as the relation $Q_{\mathrm{abs}} = Q_{\mathrm{ext}} - Q_{\mathrm{sca}}$.[3]
The asymmetry parameter is computed with a somewhat longer formula[3]

$$< \cos\theta >= \frac{4}{Q_{\mathrm{sca}} x^4} \left[\sum \frac{n(n+2)}{n+1} \Re\left\{ a_{\mathrm{n}} a^*_{\mathrm{n}+1} + b_{\mathrm{n}} b^*_{\mathrm{n}+1} \right\} + \sum_n \frac{2n+1}{n(n+1)} \Re\left\{ a_{\mathrm{n}} b^*_{\mathrm{n}} \right\} \right], \tag{3.9}$$

with $\Re\{\}$ being the real part of the complex argument in the brackets.

3.2.2. BHMIE.f

To make sure Mie.m works properly according to the original code by Bohren & Huffman[3] (1983), I compared results from Mie.m to those obtained from a slightly modified version of BHMIE.f by B. T. Draine[41]. The modification consists in including the computation of the asymmetry parameter. A comparison of efficiencies obtained by BHMIE.f and by Mie.m is given in figure 19 in section 5.1.3.

4. Data

4.1. Size Distribution Function for Protostellar Environments

The best analogue for dust in protoplanetary disks is probably realized by interstellar dust.[26] Mathis et al.[19] (1977) fitted the observed interstellar extinction with a particle size distribution of uncoated graphite, enstatite, olivine, silicon carbide, iron, and magnetite and defined a power law with $n(r) \propto r^{-3.5}$, known as MRN size distribution function (SDF). For graphite this applies to a size range between 0.005 to 1 μm, for the other materials the size range is much narrower. The according wavelength range for extinction is between 0.11 and 1 μm. Pollack et al.[26] (1985) introduced an additional particle size range between 1 and 5 μm with a SDF according in shape to terrestrial aerosols. It is as well used in later studies[27, 13, 31, 6] and called modified MRN size distribution function:

$$n(r) = \begin{cases} 1, & r < 0.005\mu m \equiv P_0, \\ (P_0/r)^{3.5}, & P_0 \leq r < 1\ \mu m, \\ (1/P_0)^2 (P_0/r)^{5.5}, & 1 \leq r < 5\ \mu m, \\ 0, & r \geq 5\ \mu m. \end{cases} \tag{4.1}$$

Although protoplanets evolve in the protoplanetary disk, the same SDF should not be used as a first assumption for their initial atmospheres. Due to grain growth, a broader size range should be considered, and a less steep slope regarding larger radii.

As proposed in Cuzzi et al.[6] (2014), I will use the following SDF for aggregate particles when computing opacity tables for protoplanetary atmospheres and consider particle radii from 1 μm upwards, and a slope s being 3.1:

$$n(r) = n_0 r^{-s}, \quad 1\ \mu m \leq r \leq 1\ cm \tag{4.2}$$

It is to keep in mind that using Mie Theory for these large radii demands more computational time since, according to the stability criterion for $n_{\max}$ (see equation 3.2 in section 3.2.1) after which the infinite series of the scattering coefficients $a_{\mathrm{n}}, b_{\mathrm{n}}$ are truncated, large size parameters x will lead to a significant increase of $n_{\max}$.

4.2. Optical Constants, Mass Fractions and Densities

For the computation of monochromatic and mean opacities dust properties of the following papers are applied.

- Pollack et al.[27] (1994)
  They provide complex refractive indices for wavelength ranges from 0.1 μm up to 0.1 m and assume different compositions for molecular clouds and accretion disks. Compared to their first paper[26], they excluded compositional properties of chondritic meteorites like hydrated silicates and magnetite, probably formed by aqueous alteration processes on the parent bodies, and consider only observational determined compositions from molecular clouds, accretion disks, solar system bodies and the diffuse ISM. The material mixture

Table 1: Density and mass fraction of different species, according to Pollack et al.[27] (1994).

Species		Density	Mass fraction	
		(g cm^{-3})	Molecular cloud	Accretion disk
Iron	Fe	7.87	2.53×10^{-4}	1.26×10^{-4}
	Fe (T > 680 K)		6.14×10^{-4}	
Olivine	$[Fe_{0.3}Mg_{0.7}]_2SiO_4$	3.49	2.51×10^{-3}	2.64×10^{-3}
Orthopyroxene	$Fe_{0.3}Mg_{0.7}SiO_3$	3.40	7.33×10^{-4}	7.70×10^{-4}
Troilite	FeS	4.83	5.69×10^{-4}	7.68×10^{-4}
Refractory and		1.50	3.53×10^{-3}	
volatile organics	CHON (1:1:0.5:0.12)	1.00	6.02×10^{-4}	
Water ice	H_2O	0.92	1.19×10^{-3}	5.55×10^{-3}

consists of troilite, metallic iron, water ice, refractory and volatile organics and anhydrous silicates, being Mg-rich olivine ($[Mg,Fe]_2SiO_4$) and orthopyroxene ($[Mg,Fe]SiO_3$) with an Fe/(Fe+Mg) ratio of 0.3. Troilite represents the dominant source of condensed sulphur with 50% residing in it in molecular cloud cores and 75% in accretion disks. It appears as an additional infra-red continuum source of opacity close to its condensation temperature. After the vaporization of troilite around 680 K to solid Fe and H_2S gas, the mass fraction of iron is increased. Mass fractions and material densities are listed in table 1. Water ice is assumed to constitute 11% of the available oxygen in molecular clouds and 52% in accretion disks. These assumptions arise from the comparison of the strength of the 3 μm H_2O band in the IR spectra of molecular clouds to features of other grain components. In the case of accretion disks, it can be determined from its cometary abundance. They obtained vaporization temperatures by performing thermodynamic equilibrium calculations and fitting a Clausius-Clapeyron equation to them. The vaporization of refractory and volatile organics is controlled by kinetics and hence, the critical temperature is determined from laboratory and observational data for relevant time-scales, i.e. the free-fall time at 1 AU from a 1 $M_\odot$ star, corresponding to 3×10^6 s, and the age of disks of interest, being around 10^{14} s. The vaporization temperatures are given in table 2.

Henning & Stognienko[13] (1996) emphasize that optical constants data from Pollack et al.[27] (1994) does not always fulfill the Kramers-Kronig relation, an integral relation between imaginary and real part of a complex function[3]. Extrapolations to longer wavelengths for silicates were carried out according to measurements by Campbell & Ulrichs[4] (1969), by assuming k being constant.[27, 13]

- Henning & Stognienko[13] (1996)
  They took optical constants for organics from Pollack et al.[27] (1994). The main difference between them is that measurements of refractive indices from silicates are mainly of amorphous samples, taken from Dorschner et al.[7] (1995) (as seen in figure 16 and also partly present in figure 15 for data from Semenov et al. [31], 2003), with the imaginary refractive index k showing smoother peaks in the near-IR region ($\lesssim 1$ μm) and a broader feature around 20 μm. Note that the optical constants for olivine differ greatly in magnitude from those of Pollack et al.[27] (1994) and Semenov et al.[31] (2003). New optical

Table 2: Vaporization temperatures of different species for molecular clouds (mc) and accretion disks (ad), according to Pollack et al.[27] (1994).

Species		Vaporization temperature (K) Gas density (g cm^{-3}) 10^{-18}	10^{-16}	10^{-14}	10^{-12}	10^{-10}	10^{-8}	10^{-6}	10^{-4}
Iron	mc/ad	835	908	994	1100	1230	1395	1612	1908
Olivine	mc/ad	929	997	1076	1168	1277	1408	1570	1774
Orthopyroxene	mc/ad	920	980	1049	1129	1222	1331	1462	1621
Troilite	mc/ad	680	680	680	680	680	680	680	680
Refractory organics	mc	575	575	575	575	575	575	575	575
	ad	425	425	425	425	425	425	425	425
Volatile organics	mc	375	375	375	375	375	375	375	375
	ad	275	275	275	275	275	275	275	275
Water ice	mc	106	115	125	138	153	172	197	230
	ad	109	118	129	143	159	180	207	244

constants for iron are taken from Ordal et al.[23] (1988), being quite similar to that by Pollack et al.[27] (1994), for troilite from Begemann et al.[2] (1994) and for water ice from Hudgins et al.[15] (1993). Regarding silicates and their strong dependence of refractive indices on the iron content, Dorschner et al. (1995) assume a ratio of Fe/(Fe+Mg)=0.0...0.1. Henning & Stognienko[13] (1996) assumed iron-poor silicates Fe/(Fe+Mg)=0, with the mass fraction of metallic iron being twice the value given by Pollack et al.[27] (1994) in table 1 for T > 680 K, and being 3.6 times the value given by Pollack et al.[27] (1994) for lower temperatures, and iron-rich silicates Fe/(Fe+Mg)=0.5, with mass fractions of 1/4 of Pollack et al.[27] (1994) for T > 680 K and zero below. The mass fraction of troilite is only 1/20 of that by Pollack et al.[27] (1994).

Extrapolation of optical constants of silicates for longer wavelengths was done assuming $k \propto \lambda^{-1}$, instead of k being constant like in Pollack et al.[27] (1994). For wavelengths longer than 500 μm, the Rosseland mean is not that sensitive to slight changes in absorption coefficients. In the case of troilite, new absorption features around 30 μm, measured by Begemann et al. (1994), are present. The new included data is in the range 10 to 500 μm, for the other regions k from Pollack et al.[27] (1994) was adopted. For organics the Kramer Kronig analysis of optical constants from Pollack et al.[27] (1994) yielded similar values, with a small reduction of ~5% in n for long wavelengths. Optical constants of amorphous water ice at a temperature of 100 K are provided by Hudgins et al.[15] (1993) and replace the Pollack et al.[27] (1994) data of hexagonal phase between 2.5 and 200 μm. Although optical constants data by Henning & Stognienko[13] (1996) is not available online, the new included data from the above mentioned sources is and replaces the Pollack et al.[27] (1994) data in the specified wavelength ranges. New computed real parts of refractive indices and extrapolations are not available, but changes are partly present in the data by Semenov et al.[31] (2003). A comparison is therefore provided with the mentioned new optical constants sources in figure 14-15 and in figure 16 for silicates from Dorschner et al.[7] (1995).

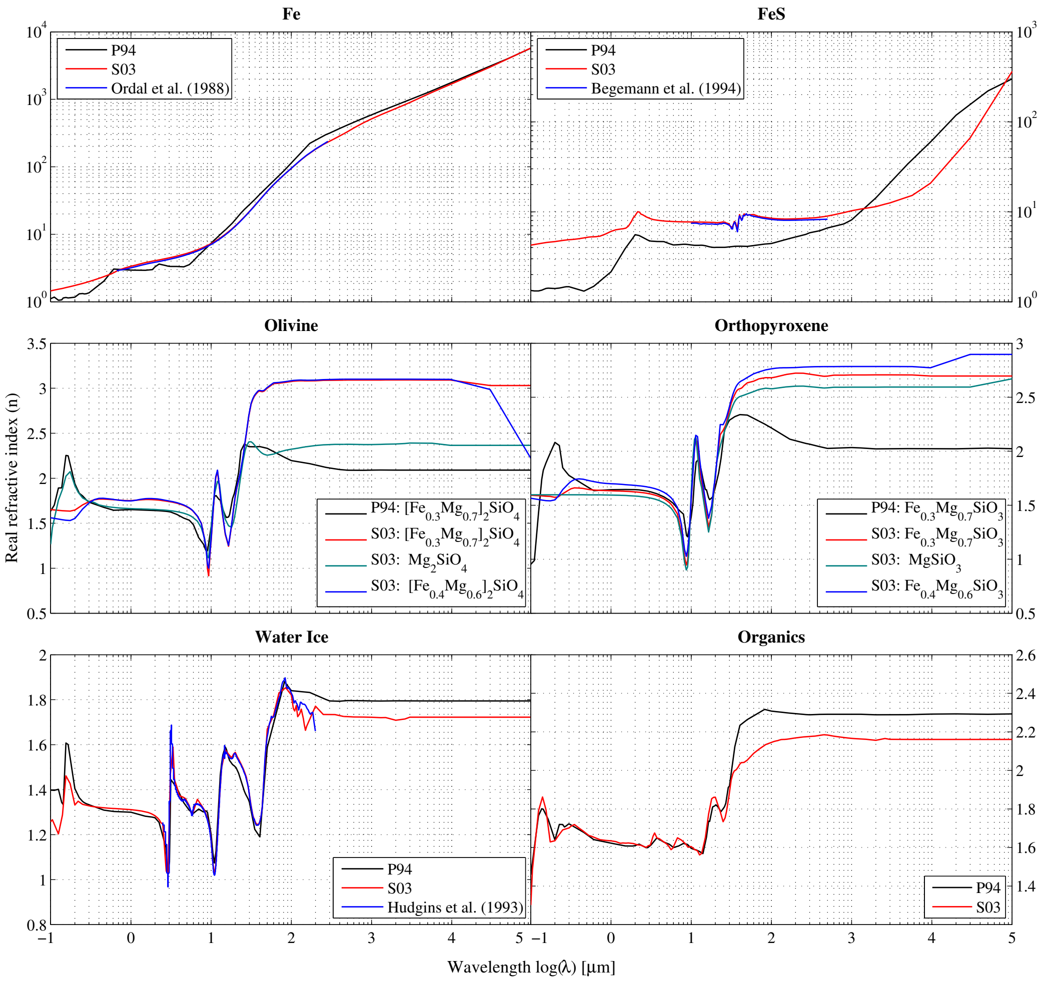

Figure 14: Real complex refractive index n for different materials from Pollack et al.[27] (1994; P94), Semenov et al.[31] (2003; S03), Ordal et al.[23] (1988), Begemann et al.[2] (1994) and Hudgins et al.[15] (1993).

- Semenov et al.[31] (2003)
  They re-estimated the absolute abundance of silicates, iron and troilite given by Henning & Stognienko[13] (1996) for the iron-rich (Fe/(Fe+Mg)=0.4) and iron-poor (Fe/(Fe+Mg)=0) case from iron stoichiometry. In contrast to Pollack et al.[27] (1994), they account only for six roughly specified temperature regions by assuming for silicates and iron the same vaporization temperature range which will not be applied here when using their optical constants data. New densities and mass fractions for iron, silicates and troilite with respect to the normal, iron-rich and iron-poor assumptions for silicates, are listed in table 3.

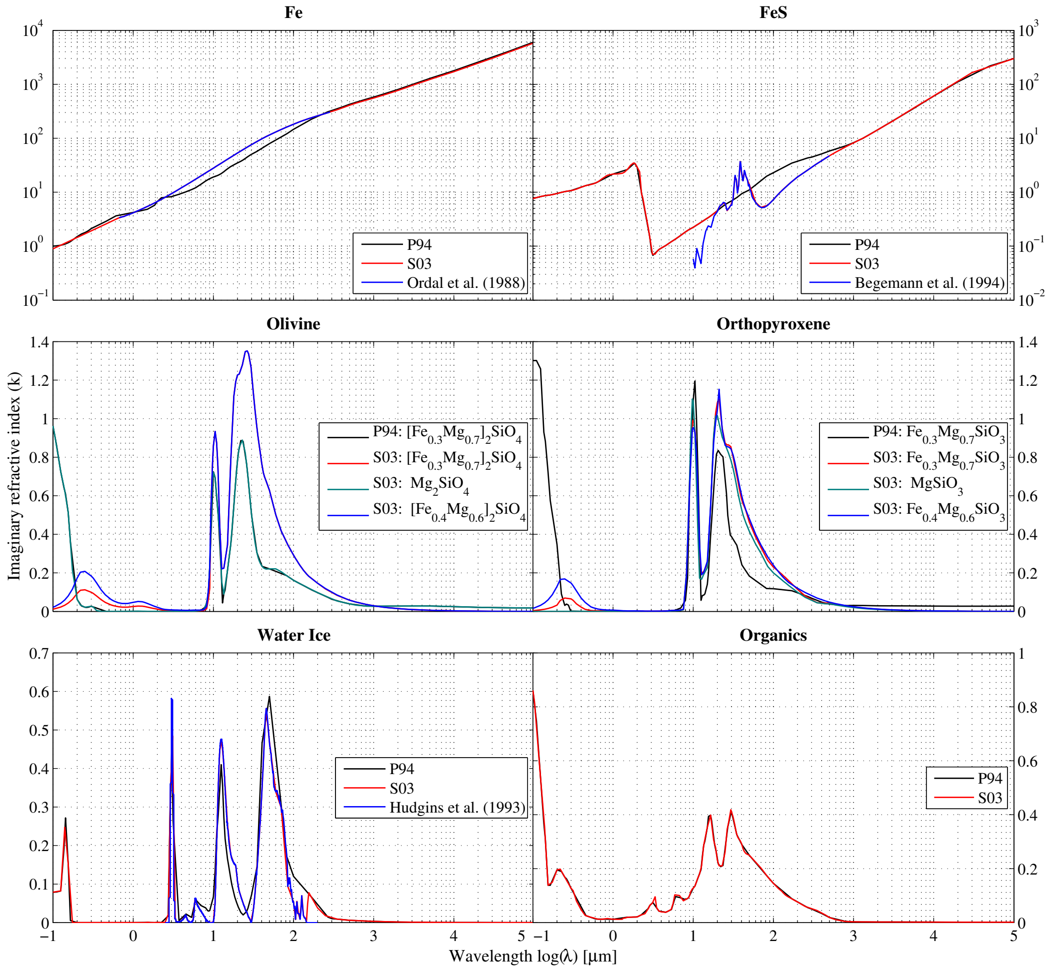

Figure 15: Imaginary complex refractive index k for different materials from Pollack et al.[27] (1994; P94), Semenov et al.[31] (2003; S03), Ordal et al.[23] (1988), Begemann et al.[2] (1994) and Hudgins et al.[15] (1993).

- Cuzzi et al.[6] (2014)
  They use the optical constants of Pollack et al.[27] (1994), but do not differ between silicates, or between volatile and refractory organics. Hence, they only assume 5 instead of 7 species and make slight changes in the optical constants, as well as the mass fraction and density for silicates. They also calculate average optical constants for aggregate particles of different compositions via EMT. I will not use their average optical constants here when dealing with aggregates, but provide a comparison to newly calculated ones by considering the whole range of species given in Pollack et al.[27] (1994) in section 5.2.

Vaporization temperatures and material densities (except for iron-rich and iron-poor silicates) are taken from Pollack et al.[27] (1994) for all optical constants data used. The mass fractions are applied according to Pollack et al.[27] (1994), Semenov et al.[31] (2003) and the therein specified

Table 3: Density and mass fraction of different species for normal, iron-rich and iron-poor silicates, according to Semenov et al.[31] (2003).

	"normal" Fe/(Fe+Mg)=0.3		"iron-rich" Fe/(Fe+Mg)=0.4		"iron-poor" Fe/(Fe+Mg)=0	
Species	ρ (g cm^{-3})	f	ρ (g cm^{-3})	f	ρ (g cm^{-3})	f
Fe	7.87	1.26×10^{-4}	-	-	7.87	7.97×10^{-4}
Fe (T > 680 K)		6.15×10^{-4}		2.42×10^{-4}		1.29×10^{-3}
$Fe_{2x}Mg_{2-2x}SiO_4$	3.49	2.64×10^{-3}	3.59	3.84×10^{-3}	3.20	6.30×10^{-4}
$Fe_xMg_{1-x}SiO_3$	3.40	7.70×10^{-4}	3.42	4.44×10^{-5}	3.20	1.91×10^{-3}
FeS	4.83	7.68×10^{-4}	4.83	3.80×10^{-4}	4.83	7.68×10^{-4}
Refractory and	1.50	3.53×10^{-3}	1.50	3.53×10^{-3}	1.50	3.53×10^{-3}
volatile CHON	1.00	6.02×10^{-4}	1.00	6.02×10^{-4}	1.00	6.02×10^{-4}
H_2O	0.92	5.55×10^{-3}	0.92	5.55×10^{-3}	0.92	5.55×10^{-3}

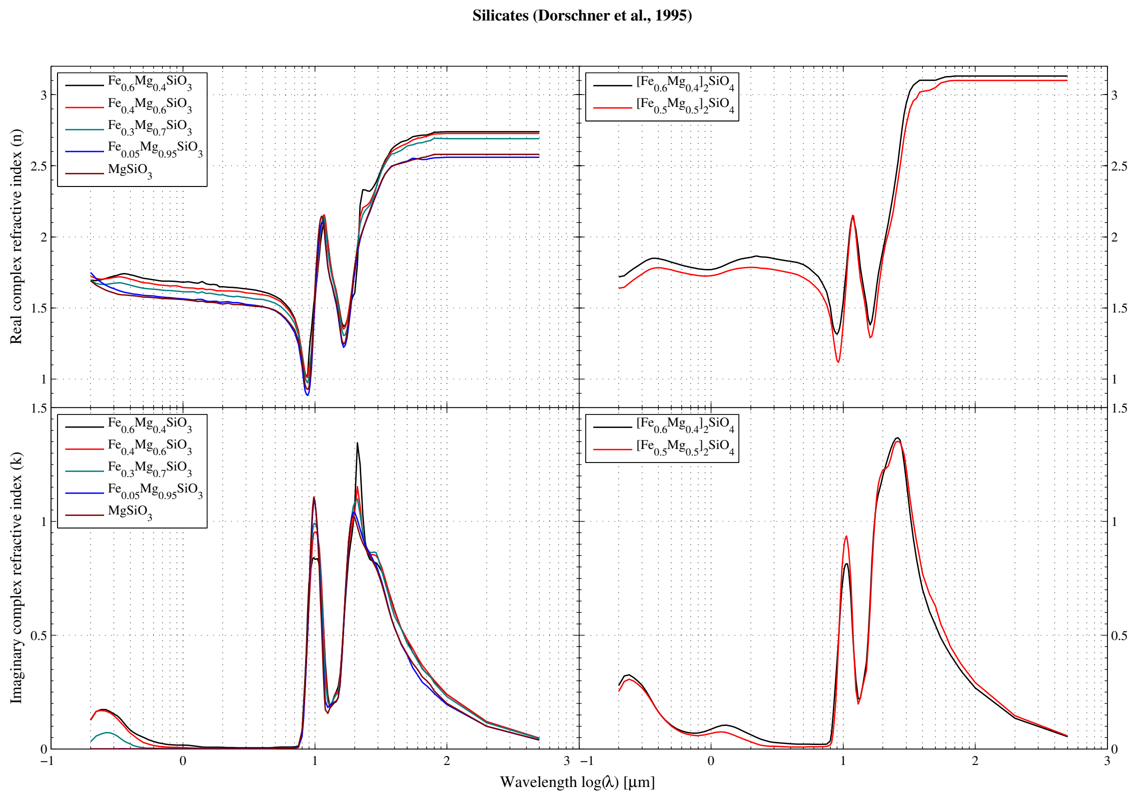

Figure 16: Complex refractive indices for silicates from Dorschner et al.[7] (1995).

definitions or sources of complex refractive indices. All of the four papers that compute mean or monochromatic opacities make usage of the MRN size distribution function. Only Cuzzi et al.[6] (2014) additionally use a flatter SDF when considering larger particle sizes of aggregates. While it is unclear which exact Mie code was used by Pollack et al.[27] (1994), Henning &

Stognienko[13] (1996) and Semenov et al.[31] (2003) use Mie Theory for at least smaller particles. All of them additionally assume aggregate particles. Cuzzi et al.[6] (2014) used approximation methods depending on the size parameter regimes, but sometimes give additionally full Mie Theory calculations for comparison. For the computation of aggregate particles, Cuzzi et al.[6] (2014), as well as Pollack et al.[27] (1994), use the Maxwell-Garnett Effective Medium Theory. Henning & Stognienko[13] (1996) use the Bruggeman mixing rule generalized for multiple components by Ossenkopf[24] (1991). The main difference is that the Bruggeman rule allows interactions between inclusions while Garnett EMT assumes a material mixture with sub-grains interacting independently with light. These interactions would become important in the resonance region. With organics being the most abundant in the assumed dust mass fraction and having optical constants far from the resonance region, the differences between this two mixing rules would hence occur after the vaporization temperature of organics.[13] Semenov et al.[31] (2003) assume particles from different coagulation processes, namely particle-cluster aggregation (PCA) and cluster-cluster aggregation (CCA), both making up 50% of the total amount and having 0.01 μm spherical inclusions. Beside the homogeneous/composite, compact/porous structure, they also consider multishell spherical particles, having all species distributed as layers in concentric spherical shells, and follow calculations for their aggregate model proposed by Henning & Stognienko[13] (1996).

5. Results

5.1. Testing the Code

In this section the code is tested using the optical constants for olivine, iron, orthopyroxene, troilite, organics and water ice from Pollack et al.[27] (1994), available as download in [42].

5.1.1. Checking numerical integration scheme for mean opacities

To test the numerical integration code for the computation of the Rosseland and Planck opacity means and compare it to the results of Pollack et al.[27] (1994), I used recalculated coefficients from Henning & Stognienko[13] (1996, see [43]), derived from the optical constants from Pollack et al.[27] (1994). They also recalculated the Rosseland mean opacity for molecular clouds with a gas density of ρ=10^{-8} g cm^{-3} (see [43]). Since coefficients were only available for 74 different wavelengths with unequally spaced intervals, numerical integration of the weighting function using the trapezoidal rule seemed more appropriate since Simpson's rule can only be applied to equally spaced intervals. To overcome this, and test my code which carries out sub-integrations of the logarithmic intervals and is further used for computation, I simulated $N = 48$ equally spaced sampling points between all available wavelengths. A linear interpolation was used to obtain coefficient values for the new generated points. This, of course, has no physical meaning at all, it moreover seems like an unnecessary manipulation of data or additional work when applying Simpson's rule integration over completely linear data, but was just done to exclude possible errors arising from the code. All in all, the values are well reproduced by using the trapezoidal rule, as can be seen in figure 17, although the resolution, i.e. the number of wavelengths for which the coefficients are defined, is very small. Also, there are no errors in the numerical integration scheme I used for further computations. Four out of seven coefficients

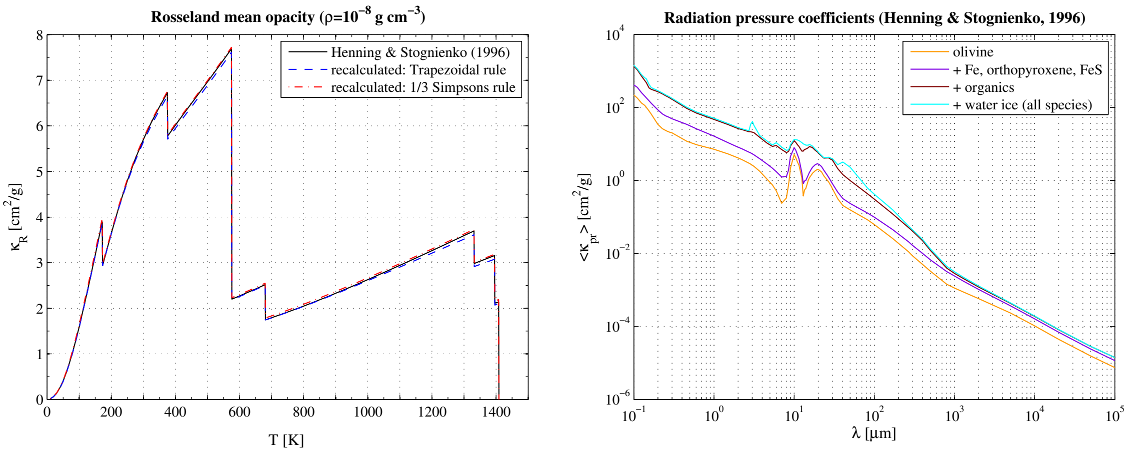

Figure 17: Recalculated Rosseland mean opacity (left) for molecular clouds with a gas density of 10^{-8} g cm^{-3} using radiation pressure coefficients (right) of Henning & Stognienko[13] (1996) recalculated from optical constants data of Pollack et al.[27] (1994). For better visibility only four out of seven <$\kappa_{\rm pr}$> are plotted.

for different material mixtures corresponding to different temperature regimes from Henning & Stognienko[13] (1996) are plotted in the right sub-figure.

5.1.2. Comparison of coefficients

The data provided by Henning & Stognienko (1996) was calculated with the Mie code from Pollack et al.[27] (1994). It was not possible for me to obtain this code for reproducing the radiation pressure coefficients needed for the calculation of the mean opacities. So, only a comparison with the full Mie Theory code I used is possible. The error arising from these different codes for the coefficients is not a small one, as can be seen in figure 18 for olivine. The shape of the curves for both scattering coefficients seems well reproduced in the left sub-figure but the magnitude is not. Interestingly the cut-off of scattering and absorption coefficient of Henning & Stognienko (1996) from the newly calculated values already happens at very low frequencies. This is not the case for the radiation pressure coefficient which shows a very steep increase after approximately 1500 THz. This strong increase cannot be reproduced by my computations. Below 1500 THz the curves of both radiation pressure coefficients nearly match but the sum of absorption and scattering coefficient, i.e. the extinction coefficient, is well below my calculated values, although the spread between extinction and scattering is nearly the same for both methods. Hence, the difference in magnitude in this range, resulting in almost equal radiation pressure coefficients, is caused solely by the different asymmetry factors entering in the correction term (see equation 2.40).

Above 1500 THz the spread between scattering and extinction coefficient increases, as does the deviation of the radiation pressure coefficient curve from my calculated values. This could be

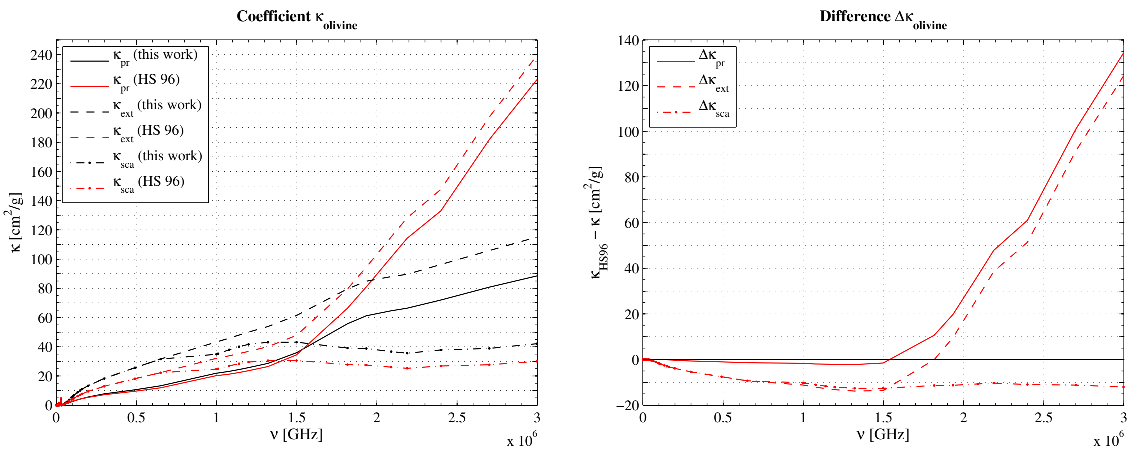

Figure 18: Recalculation of absorption, scattering and radiation pressure coefficients for olivine (left) using a full Mie Theory code (this work, black) and comparison to the recalculated coefficients by Henning & Stognienko[13] (1996, red) using a Mie Theory code from Pollack et al.[27] (1994). Note that coefficients are already multiplied with the assumed mass fraction. The optical constants and mass fractions according to molecular clouds are again taken from Pollack et al.[27] (1994). The difference between both calculations is plotted in the right diagram.

probably because with increasing frequency or decreasing wavelength the error in efficiencies, arising for very large radii compared to the wavelength, $r \gg \lambda$, becomes more and more apparent in a Mie approximation code than in a full Mie Theory code. In other words, the decrease in the wavelength leads to an increase in the overall size parameters and errors occur for methods valid only in the smaller size parameter range which makes the question, how the Mie calculations were done by Pollack et al.[27] (1994), even more relevant. Unfortunately, I cannot provide a detailed code comparison and draw more meaningful conclusions.

5.1.3. Checking the Mie Theory code

To make sure that no errors enter through the external code Mie.m, I also computed efficiencies Q with a slightly modified version of the code[41] of Bohren & Huffman (1983) and compared them to the results of Mie.m. As can be seen in figure 19, the curves of the efficiencies derived from both codes completely match for all materials. So an error arising for the efficiencies from Mie.m can be excluded.

In general, considering large size parameters $X \gg 1$, the efficiencies calculated by a full Mie Theory code converge towards the geometrical optics limit. As can be seen in figure 19 and is pointed out by several authors (see e.g., Bohren & Huffman, 1983), the extinction efficiency Q_{ext} heads towards the value 2 for increasing size parameters X. This is known as the extinction paradox since it states that a large body would remove twice the energy incident on it, and is twice the limit obtained from geometrical optics. While geometrical optics provides a good approximation by assuming a large particle as a planar obstacle with the same projected area, it neglects edge deflections adding to the total extinction. This circumstance, requiring the extinction cross section to be twice the geometrical cross section, is not always observed due to limited acceptance angles of detectors when measuring extinction by very large particles.[3]
When converging towards the geometrical optics limit, some materials show an additional structure, called interference structure, that is, according to the definition of the extinction phenomenon, due to the interference between incident and forward scattered light. The existence of the fine ripple structure in between relates mathematically to conditions where the denominators of the scattering coefficients a_{n} and b_{n} vanish. Both structures are hence due to scattering and should not be confused with bulk absorption peaks when the complex refractive index k, and hence absorption, is large, as can be seen for solid iron and troilite. In such cases the interference and ripple structure becomes damped and is almost not present.[3]

5.1.4. Resolution

For the numerical integration over particle radius (dr) 50 sub-integrations n between logarithmic intervals with 51 equidistant points ($N + 1$) in between were chosen. For the frequency, testing yielded an optimal selection of $n = 100$ and $N = 100$. Higher resolutions lead to no significant effort compared to runtime since they would bring only changes after the fourth position after decimal point, mostly due to rounding. Since opacity means for aggregates with larger particle sizes show only decreases in the order of 10, very small improvements by choosing more sample points for integration can be neglected without any further concern in order to achieve an acceptable runtime.

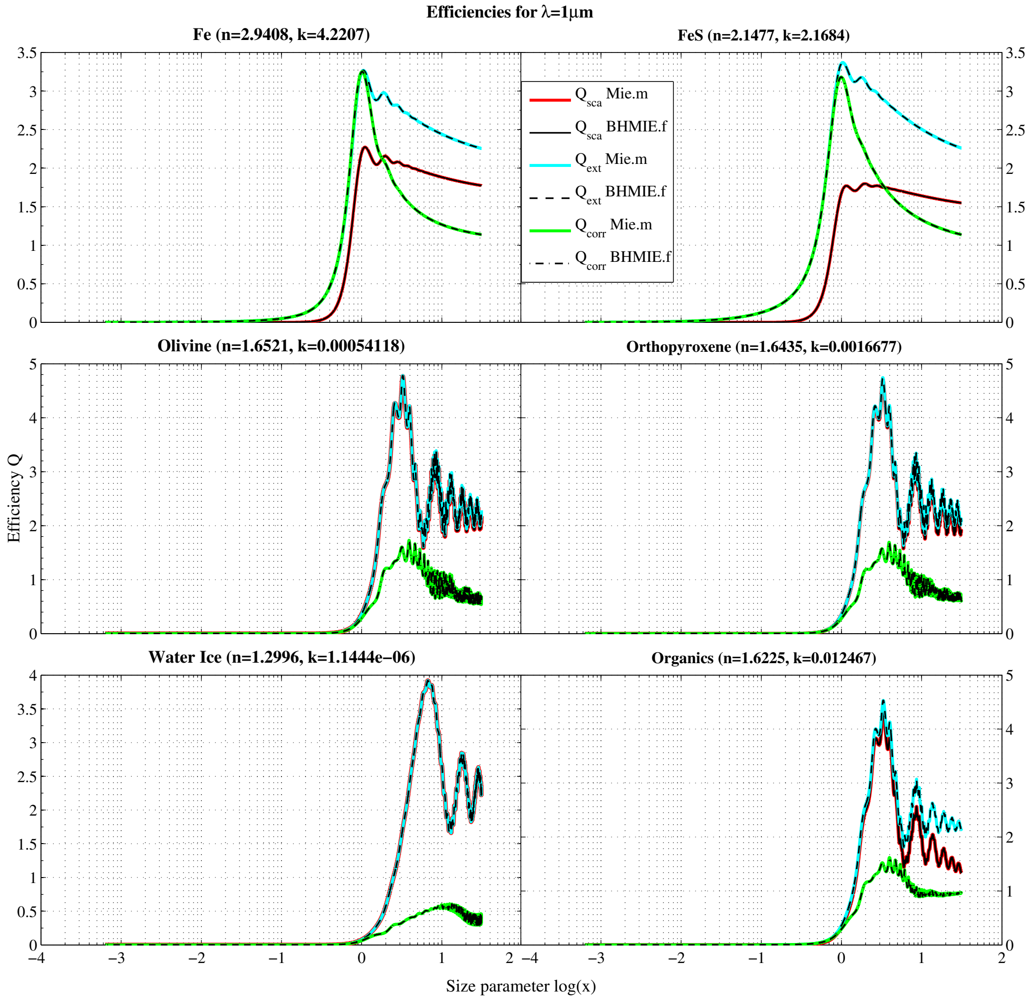

Figure 19: Efficiencies derived from BHMIE.f and Mie.m for different materials at $\lambda = 1\mu m$.

In table 4 the peaks in Rosseland mean extinction coefficient (over the considered temperature range), derived from Simpson's rule integration over the whole frequency interval, are compared to those summing up different Simpson's rule sub-integrations for logarithmic intervals. At first with a higher resolution for dr, but afterwards compared with two smaller resolutions that show only slight changes in the fourth position after decimal point (see table 5a+b). The peaks over the temperature range relate to the vaporization temperatures of the different materials in molecular clouds according to a medium density of $\rho = 10^{-8}$ g cm^{-3}, i.e. 172 K for water ice, 375 K for volatile organics, 575 K for refractory organics, 680 K for troilite, 1331 K for orthopyroxene and 1395 K for solid iron.

Using sub-integrations for logarithmic specified intervals yields better results for a smaller amount of sample points along with a shorter runtime. This is, of course, due to its consideration of more values in the longer wavelength/lower frequency range, already at small resolutions. In contrast, a single integration with equidistant subintervals has most of its sampling points covering the smaller wavelength/higher frequency range. The amount of points, or the length of the frequency vector, for which the efficiencies Q are interpolated, is determined by $n_{\text{points}} = (N+1)(n-1) - (n-2)$ for using sub-integrations for logarithmic intervals or by $n_{\text{points}} = N + 1$ for a single integration with N subintervals. Furthermore, the highest change is seen for lower temperatures where the Planck curve is in general broader and more shifted to longer wavelengths and hence, weights them stronger than it is the case at higher temperatures. So the inclusion of more longer wavelengths, i.e. lower frequencies, in the numerical integration scheme clearly makes a difference for opacities the lower temperature region.

sub-integrations	subintervals	mean opacity peaks [cm^2/g]					
(n)	(N)	172 K	375 K	575 K	680 K	1331 K	1395 K
50	50	4.0562	7.0902	8.1937	2.9847	4.1095	3.5851
100	100	4.0562	7.0904	8.1939	2.9847	4.1096	3.5852
200	100	4.0562	7.0904	8.1939	2.9847	4.1096	3.5852
1	10000	4.0475	7.0868	8.1927	2.9841	4.1092	3.5848
1	20000	4.0582	7.0911	8.1941	2.9848	4.1096	3.5852

Table 4: Testing different resolutions for the numerical integration of the weighting function in equation 2.71 with 1/3 Simpson's rule for $n_{\text{r,points}} = 9901$ ($n_{\text{r}} = 100, N_{\text{r}} = 100$).

(a) n_r=30, N_r=30							
sub-integrations	subintervals	mean opacity peaks [cm^2/g]					
(n)	(N)	172 K	375 K	575 K	680 K	1331 K	1395 K
50	50	4.0562	7.0902	8.1937	2.9846	4.1094	3.5850
100	100	4.0562	7.0904	8.1939	2.9847	4.1095	3.5851

(b) n_r=50, N_r=50							
sub-integrations	subintervals	mean opacity peaks [cm^2/g]					
(n)	(N)	172 K	375 K	575 K	680 K	1331 K	1395 K
50	50	4.0562	7.0902	8.1937	2.9847	4.1095	3.5852
100	100	4.0562	7.0904	8.1939	2.9848	4.1096	3.5852

Table 5: Testing different resolutions for the numerical integration of the weighting function in equation 2.71 with 1/3 Simpson's rule for (a) $n_{\text{r,points}} = 871$ ($n_{\text{r}} = 30, N_{\text{r}} = 30$) and (b) $n_{\text{r,points}} = 2451$ ($n_{\text{r}} = 50, N_{\text{r}} = 50$).

particle radius (r)			frequency (ν)			points
n	N	n_{points}	n	N	n_{points}	($n_{\text{r}} \times n_{\nu}$)
50	50	2451	50	50	2451	6007401
50	50	2451	100	100	9901	24267351
100	100	9901	100	100	9901	98029801

Table 6: Comparison of different variations in vector length of particle radius (r) and frequency (ν).

5.1.5. Comparison of mean coefficients

Figure 20 gives a comparison of the Rosseland mean opacity for a gas density of 10^{-8} g cm^{-3} recalculated by Henning & Stognienko (1996) and this work. There is a clear, but almost constant offset from the original curve in each temperature regime corresponding to different mixtures of material species. This is probably explained by differences in the Mie Theory codes used, as shown in the previous chapters. For the different peaks the deviation from the values by Henning & Stognienko (1996) is given with +4.16% at 172 K, +5.39% at 375 K, +6.53% at 575 K, +18.52% at 680 K, +11.21% at 1331 K, +13.63% at 1395 K and +0.97% at 1408 K. The highest deviation is found in the temperature regime after the vaporization of organics, in the range of 576-680 K, corresponding to a dust mixture of olivine, orthopyroxene, iron and troilite with deviations ranging from +18.68% at 576 K to +18.52% at 680 K at which troilite is vaporized.

In table 13-14 in Appendix A.3 the recalculated Planck and Rosseland mean opacities are listed for a temperature range of 10-1908 K and for gas densities ranging from 10^{-18} to 10^{-4} g cm^{-3}.

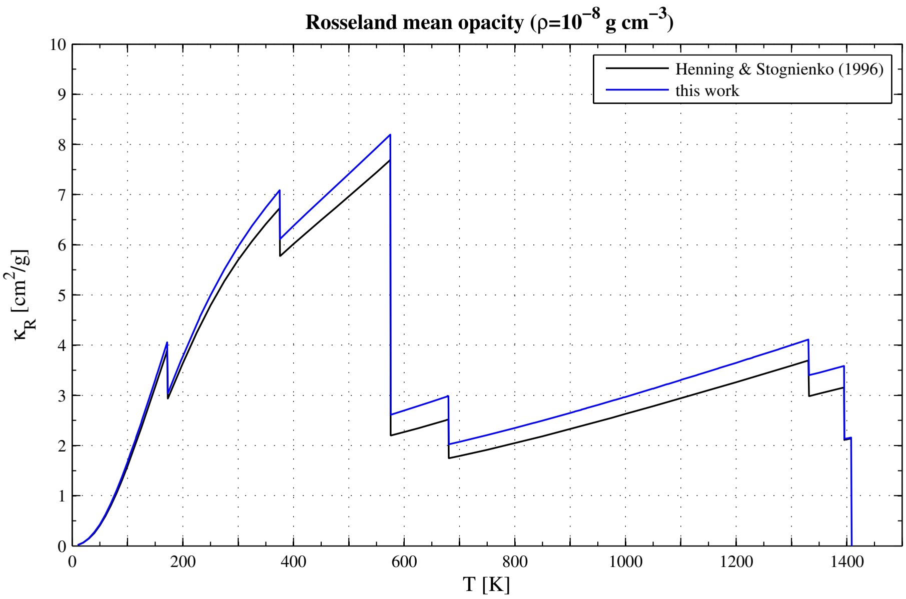

Figure 20: Recalculated Rosseland mean opacity for molecular clouds with a gas density of 10^{-8} g cm^{-3} of Henning & Stognienko (1996)[13] and this work. Both are recalculated from optical constants data of Pollack et al.[27] (1994).

5.2. Optical Constants for Aggregates

Optical constants for aggregated particles of different mixture were calculated with the Effective Medium Theory (see section 2.2) that gives average refractive indices for particles having different species inclusions. Following Cuzzi et al.[6] (2014), I computed optical constants for nine different kinds of aggregates with properties and compositional inclusions listed in table 7-8, according to the temperature regime where they can exist, taken again from Pollack et al.[27] (1994). The particle volume fractions f_v for the nine aggregates are given for the compact case (porosity ϕ=0) in table 9. Note that when assuming porosity, $f_mathrmv$ and the aggregate particle density is reduced by the factor $(1-\phi)$, with respect to their non-porous values.
In contrast to Cuzzi et al.[6] (2014), I used the full range of particle species given by Pollack et al.[27] (1994) and did not melt two species to being only one, namely olivine and orthopyroxene to silicates and volatile and refractory organics to organics. This is why the optical constants for aggregates of this work (see figure 21a) and those of Cuzzi et al.[6] (2014) (see figure 22, i.e. figure 6 in their paper) show small differences, but the overall features appear to be quite similar. Note that the peak <0.5 μm that also exists for the single species olivine, orthopyroxene, water ice and organics (see figure 14 in section 4.2) and hence, is produced here by their presence as inclusions, is absent in figure 22 because Cuzzi et al.[6] (2014) apparently do not present values at this small wavelengths. The higher the volume fraction of silicates within the aggregate particle becomes, the more the peak grows in magnitude. Also, the feature of two small peaks appearing between 50 and 100 μm in figure 22, both in real and imaginary refractive index, is perhaps due to a higher weighting of water ice compared to the other species (being only 4 instead of 7 in their paper) and appears in figure 21a only as one peak.
As a comparison, optical constants for the porous aggregates of different composition are plotted in figure 21b. Note the decrease in magnitude for both real and imaginary refractive indices relating to a reduced particle volume fraction and hence, a smaller difference between denominator and numerator in equation 2.47 resulting in a lower ratio. The porosity is assumed to be 90%.

Table 7: Compact aggregate density and mass fraction for aggregates of nine different compositions.

Properties of aggregates		
Composition	compact aggregate density $\bar{\rho}$ (g cm^{-3})	gas mass fraction $f=\sum_\mathrm{j} f_\mathrm{j}$
Fe, Olivine, Orthopyroxene, FeS, CHON refr., vol., Water ice	1.38	1.399×10^{-2}
Fe, Olivine, Orthopyroxene, FeS, CHON refr., vol.	2.05	8.436×10^{-3}
Fe, Olivine, Orthopyroxene, FeS, CHON refr.	2.23	7.834×10^{-3}
Fe, Olivine, Orthopyroxene, FeS	3.72	4.304×10^{-3}
Fe, Olivine, Orthopyroxene	3.79	4.024×10^{-3}
Olivine, Orthopyroxene	3.47	3.410×10^{-3}
Fe, Olivine	3.90	3.254×10^{-3}
Olivine	3.49	2.640×10^{-3}
Fe	7.87	6.140×10^{-4}

Table 8: Temperature regime of aggregates according to the vaporization temperatures of their various species inclusions given by Pollack et al.[27] (1994).

Temperature regime (K) for aggregates									
		Gas density (g cm^{-3})							
Composition		10^{-18}	10^{-16}	10^{-14}	10^{-12}	10^{-10}	10^{-8}	10^{-6}	10^{-4}
all	T_{min}				1				
	T_{max}	109	118	129	143	159	180	207	244
without water ice	T_{min}	110	119	130	144	160	181	208	245
	T_{max}				275				
without volatile organics	T_{min}				276				
	T_{max}				425				
without organics	T_{min}				426				
	T_{max}				680				
without troilite	T_{min}				681				
	T_{max}	835	908	994	1100	1222	1331	1462	1621
silicates	T_{min}	836	909	995	1101	-	-	-	-
	T_{max}	920	980	1049	1129	-	-	-	-
iron + olivine	T_{min}	-	-	-	-	1223	1332	1463	1622
	T_{max}	-	-	-	-	1230	1395	1570	1774
olivine	T_{min}	921	981	1050	1130	1231	1396	-	-
	T_{max}	929	997	1076	1168	1277	1408	-	-
iron	T_{min}	-	-	-	-	-	-	1571	1775
	T_{max}	-	-	-	-	-	-	1612	1908

Table 9: Particle volume fraction of inclusions for nine aggregates with different compositions.

Particle volume fraction f_v of inclusions for different compositions						
Fe	Olivine	Orthopyroxene	FeS	CHON refr.	vol.	Water ice
1.6×10^{-3}	7.46×10^{-2}	2.23×10^{-2}	1.57×10^{-2}	2.319×10^{-1}	5.93×10^{-2}	5.946×10^{-1}
3.9×10^{-3}	1.839×10^{-1}	5.51×10^{-2}	3.87×10^{-2}	5.721×10^{-1}	1.464×10^{-1}	
4.6×10^{-3}	2.154×10^{-1}	6.45×10^{-2}	4.53×10^{-2}	6.702×10^{-1}		
1.38×10^{-2}	6.532×10^{-1}	1.956×10^{-1}	1.373×10^{-1}			
7.35×10^{-2}	7.130×10^{-1}	2.135×10^{-1}				
	7.696×10^{-1}	2.304×10^{-1}				
9.35×10^{-2}	9.065×10^{-1}					
	1					
1						

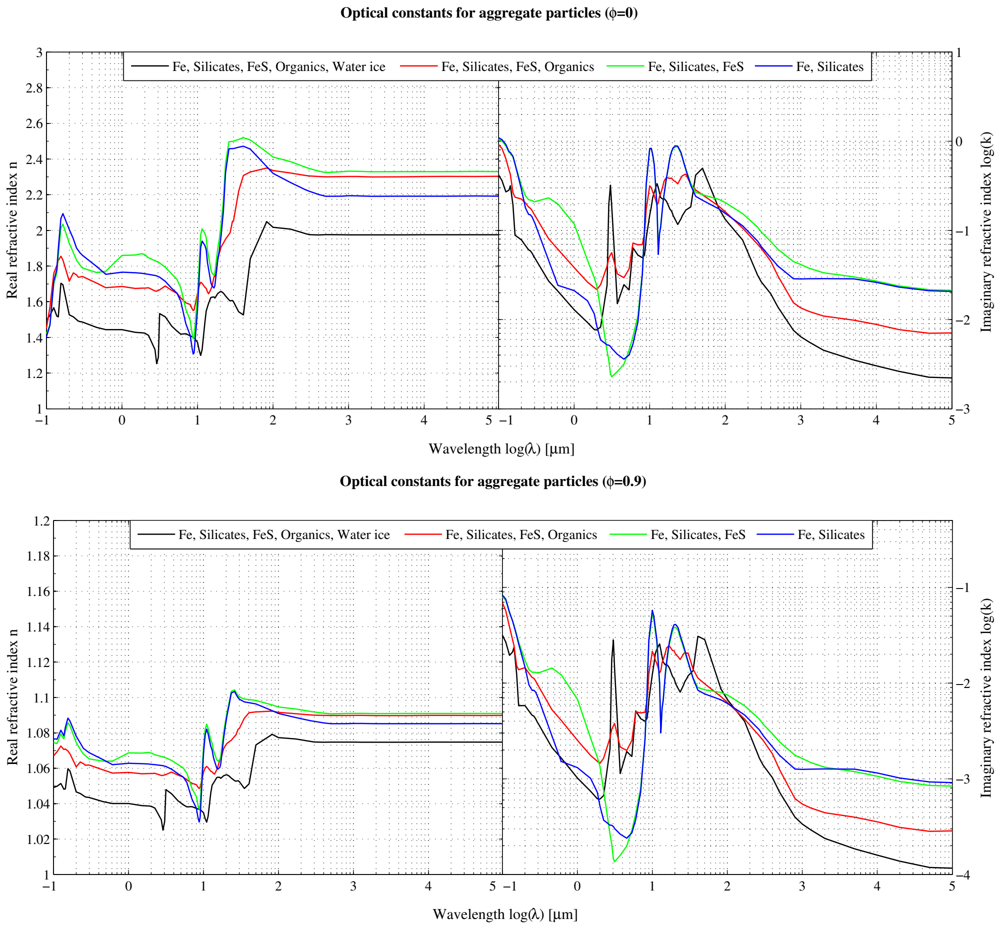

Figure 21: Complex refractive indices for (a) compact and (b) porous aggregates (ϕ=0.9) obtained from EMT by using the optical constants and defined species properties of Pollack et al.[27] (1994).

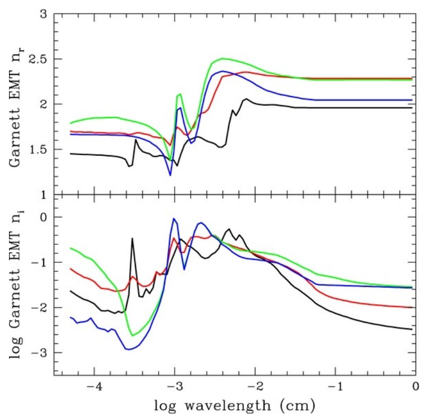

Figure 22: Complex refractive indices for aggregates obtained from EMT by Cuzzi et al.[6] (2014, figure 6 in their paper).

5.3. Monochromatic Coefficients

5.3.1. Compact and porous aggregate particles

As can be seen in figure 23, porous aggregates show stronger features between 0.1 and 50 μm in their radiation pressure coefficients, relating to the already mentioned interference structure. This is because compact aggregates have a larger imaginary refractive index than porous aggregates and hence, these features resulting from scattering are more strongly damped by absorption. When converging towards the geometrical optics limit $r \gg \lambda$ (to the left side in the figure), compact aggregates approach a constant value, while adding porosity results in an increase since it mimics the behaviour of smaller particles[10] existing in a vacuum. Hence, their curves are more similar to a MRN SDF, as can be seen in figure 24. At longer wavelengths, the existence of larger particle sizes results in higher monochromatic radiation pressure coefficients. This is because for particles with $r \ll \lambda$ absorption becomes the dominant process[3, 6]. The absence of scattering when approaching longer wavelengths results in a significant decrease in extinction. The bump that indicates this decrease in scattering is hence shifted more to the right for aggregates with higher $r_{\max}$. With increasing $r_{\max}$ also the interference structure for porous aggregates becomes less pronounced, and also the magnitude of $\kappa_{\rm pr}$ decreases due to an increasing amount of particle sizes being already in their geometrical optics regime.

A comparison to the monochromatic coefficients obtained from a MRN SDF and for aggregates of different compositions, relating to different temperature regimes where they are assumed to exist, is given in figure 24. In addition, to provide a better understanding of the behaviour of the mean opacity curves in section 5.4.2, vertical lines are plotted indicating at which wavelength for the given temperatures the weighting functions for the Planck mean (black) and the Rosse-

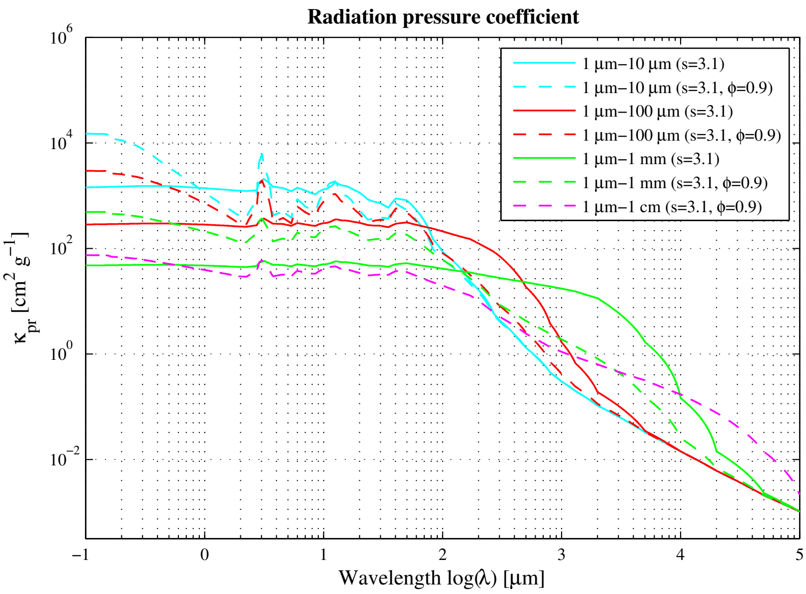

Figure 23: Radiation pressure coefficient for compact (ϕ=0) and porous (ϕ=0.9) aggregates.

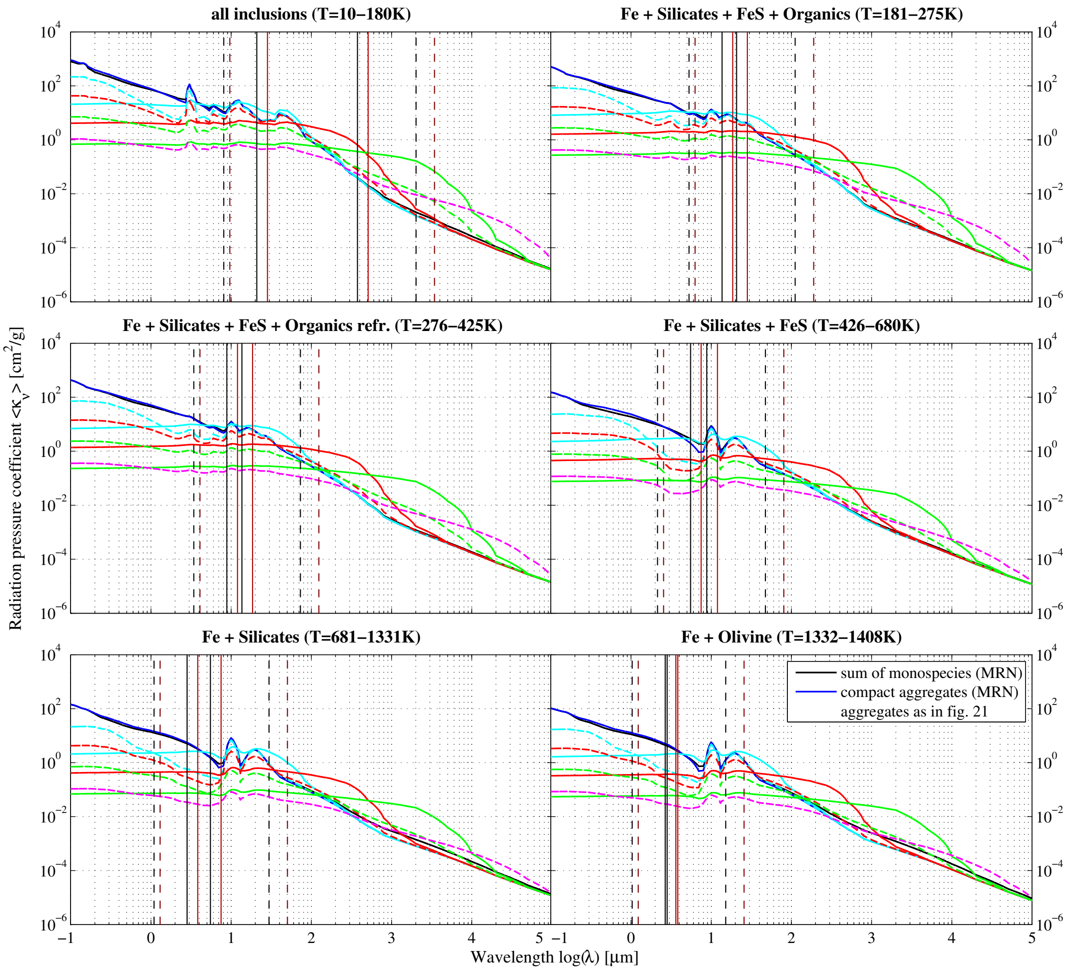

Figure 24: Radiation pressure coefficients for different compositions, corresponding to different temperature ranges, for compact homogeneous particles (black) and compact aggregates (blue) having a MRN SDF, as well as compact (ϕ=0; solid) and porous (ϕ=0.9; dashed) aggregates having a SDF with slope 3.1 and a particle range from 1-10 μm (cyan), 1-100 μm (red), 1 μm-1mm (green) and 1 μm-1cm (magenta). The solid vertical lines correspond to the wavelength where the Planck function $B(T)$ (black) and its derivative with temperature $\partial B/\partial T$ (darkred) have its maximum and hence, coefficients are weighted stronger and will contribute most to the mean opacities. The dashed vertical lines indicate wavelengths at which the maximum of the corresponding weighting function has decreased by 1/10.

land mean (darkred) have their maximum. The dashed curves relate to wavelengths at which the maxima of the weighting functions have decreased to 10%.

5.4. Mean Opacities

Recalculations of mean opacities were carried out for molecular clouds (figure 20 in section 5.1.5) and accretion disks (see table 15-16 in the Appendix A.3) with optical constants from Pollack et al.[27] (1994) and, only for accretion disks, with optical constants from Semenov et al.[31] (2003). In both cases, spherical homogeneous compact particles having a MRN SDF were assumed. In addition, mean opacities of compact and porous aggregates for two different size distributions and different particle size ranges are presented.

5.4.1. Compact spherical particles

Newly calculated Rosseland and Planck mean opacities from optical constants data of Semenov et al.[31] (2003) for compact spherical particles are presented in table 17-22 in Appendix A.3 and for a density of 10^{-8} g cm^{-3} in figure 25 for three different metallicity cases.
Considering iron-rich silicates, when all of the iron is at first only contained in silicates and to a lesser extent - compared to the other two cases - in troilite, the Rosseland and Planck mean curves both show a smoother increase between the peaks than in the iron-poor silicates and normal case. Due to the low mass fraction of troilite for the iron-rich case, the curve is also well below the others, especially after the vaporization of organics (T>425 K), a temperature region where troilite obviously strongly contributes to the mean opacity in the other two cases. After the vaporization temperature of troilite (T< 680 K) the existence of metallic iron as solid particles but, especially, the higher mass fraction of olivine results in a sharper increase compared to the other two metallicity assumptions. The dip after the vaporization temperature of orthopyroxene is almost not present since its mass fraction compared to olivine is assumed to be two order of magnitudes smaller in the case of iron-rich silicates (see table 3). The high mass fraction of olivine therefore results in higher mean extinctions in the higher temperature regime of the curve compared to the other two assumptions.
The highest amount of solid metallic iron particles is given from the beginning in the case of iron-poor silicates. This is reflected in the steep slope of the curve between the peaks compared to the other two cases. Before the vaporization of troilite, the relation of olivine:orthopyroxene:iron is 1:0.3:0.05 for the normal silicates assumption with Fe/(Fe+Mg)=0.3, 1:0.01:1 for assuming iron-rich silicates with Fe/(Fe+Mg)=0.4, and 0.33:1:0.42 for the iron-poor silicates case. For T > 680 K it is 1:0.01:0.23, 1:0.01:0.06, and 0.33:1:0.68 for normal, iron-rich and iron-poor silicates, respectively.

5.4.2. Compact and porous aggregated particles

New mean opacities for compact, as well as porous particles were calculated for the average optical constants obtained by EMT. As can be seen in figure 26, the curves for compact solids and compact aggregates with a MRN size distribution function are quite similar at smaller temperatures, then the aggregates show a significant deviation from the compact monospecies particles, especially after the vaporization of organics. Both curves match again at higher temperatures. This effect becomes clear when looking at the radiation pressure coefficients for aggregates consisting of iron, silicates and troilite in figure 24. There is a significant deviation of the curve

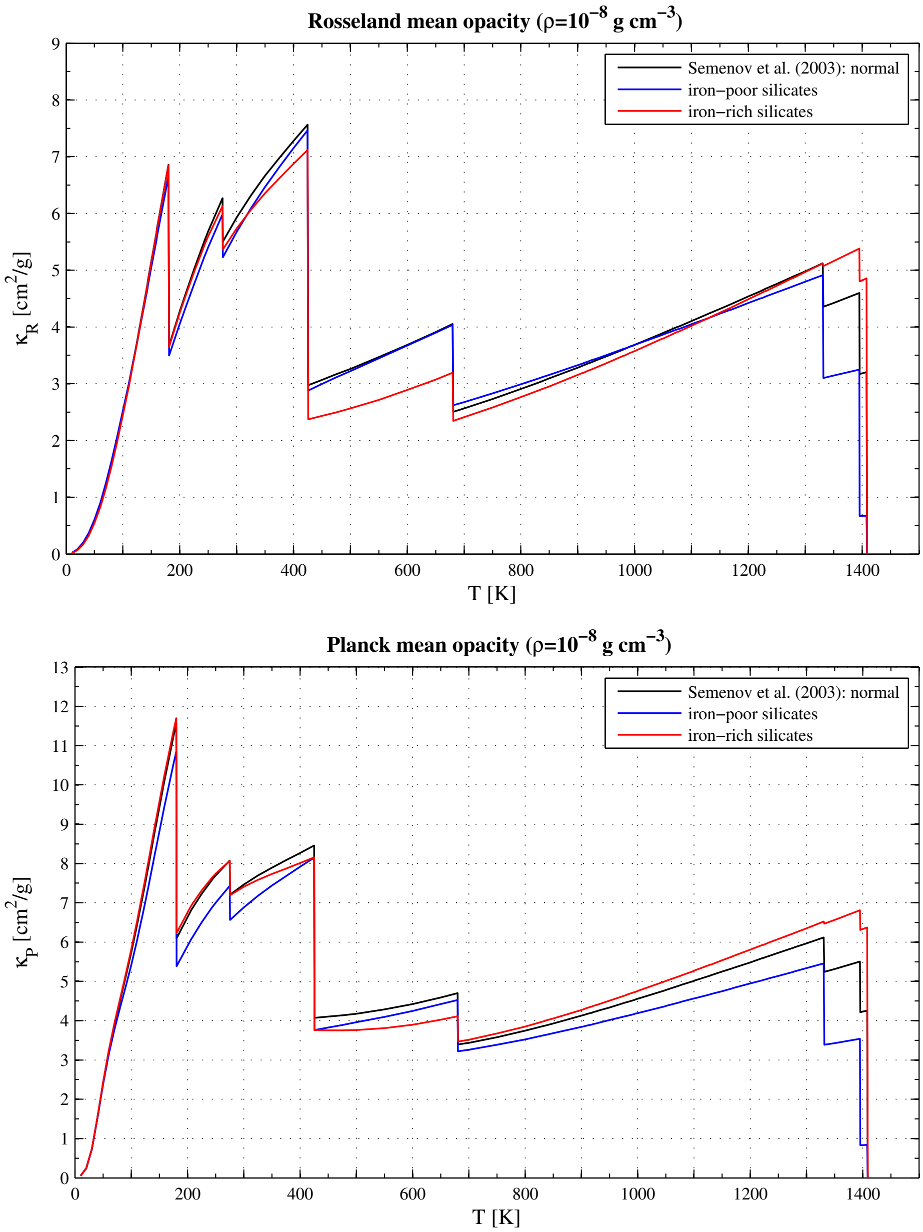

Figure 25: Rosseland and Planck mean opacity for accretion disks using optical constants data from Semenov et al.[31] (2003) considering normal, iron-rich and iron-poor silicates.

representing the standard mixture of compact, homogeneous particles from the curve of compact aggregates with a MRN SDF between the two red lines, indicating the wavelength range in which $\partial B/\partial T$ is maximal at the considered temperatures. Hence, these radiation pressure coefficients contribute the most to the Rosseland mean opacity, producing a decrease in magnitude compared to the "standard" MRN case. When inspecting the radiation pressure coefficient of

aggregates consisting of iron and silicates, we notice that at those wavelengths where weighted most heavily, the coefficients lay slightly above the curve of compact monospecies and hence, we see a stronger slope in the Rosseland mean curve up to the vaporization temperature of orthopyroxene.
The SDF with a slope of 3.1 is applied for particle ranges of 1 μm up to maximum sizes of 10 μm (cyan), 100 μm (red), 1 mm (green) and 1 cm (magenta), like in Cuzzi et al. [6] (2014). Dashed curves relate to aggregates having a porosity of 90%, whereas solid is used for compact aggregates. The maximum opacity is obtained for temperatures smaller than the vaporization temperature of organics for a size range of 1-10 μm. Interestingly, adding porosity to the aggregates does here not result in an opacity increase, whereas it does for broader size ranges with higher maximal particle radii. Increasing the maximum particle radius leads to a higher opacity at small temperatures and a smoother increase up to the maximum opacity that is always at temperatures close to the vaporization temperature of water ice. In the case of $r_{\max}$=100 μm, adding porosity even changes the trend of the curve to steeper slopes, as seen for smaller particle ranges, and a clear increase in magnitude in the region where water ice no longer but organics still exist, i.e. between $\sim$173 and 425 K. The assumption of small sizes and high porosities simulates the behaviour of even smaller monospecies, the inclusions of the aggregate, as independent single particles in a matrix consisting of vacuum. That is why when looking at 1 to 10 μm sizes, adding porosity results in a decrease in magnitude.
When considering the high temperature regime, it becomes obvious that larger size particles exert a very smooth trend in opacity. At these high temperatures the derivative of the Planck mean with respect to temperature has its maximum at higher frequencies/shorter wavelengths and hence, efficiencies in this regime are stronger weighted. Since with increasing $r_{\max}$, the higher amount of compact aggregates of larger sizes interact with radiation at these frequencies already beyond their geometrical optics limit, and Q_{ext} and κ_{pr} approach a constant value. This is the case for all compact aggregates, even smaller ones in ranges of 1-10μm. Porous aggregates are sometimes below their compact counterparts since the frequency region where κ_{pr} is weighted the most, relates to a dip in their curves. Note that for a temperature of 425 K the wavelength where $\partial B/\partial T$ has its maximum is around $\sim$5μm. The Rosseland mean opacities in figure 26 are quite similar to the ones obtained by Cuzzi et al.[6] (2014), although the magnitude is somewhat different, especially when considering larger $r_{\max}$ where the mean opacities for porous aggregates of sizes 1 μm-100 cm are well above the ones for compact aggregates of 1 μm-1 mm (see their figure 11). This difference may occur from the usage of different efficiency calculations, based on Mie approximations in their work and on full Mie Theory here.

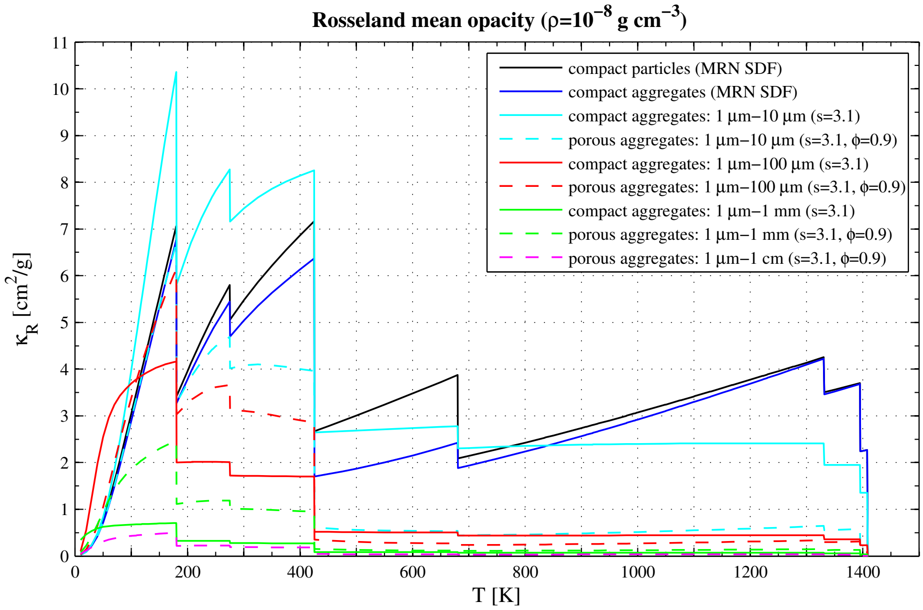

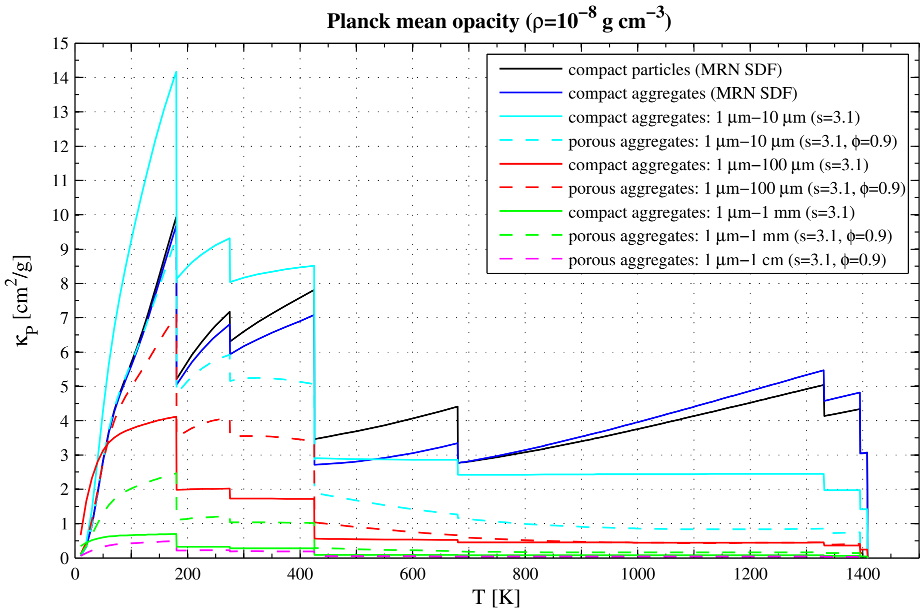

Figure 26: Rosseland and Planck mean opacity for compact particles (MRN SDF; black), compact aggregate particles (MRN SDF, blue), aggregate particles having different size ranges and a SDF with slope 3.1 (solid: compact, dashed: porosity=90%).

6. Conclusion

Considering aggregates, the shape of the Rosseland mean opacity over temperature from Cuzzi et al.[6] (2014), as well as the influence of porosity and larger particle sizes, could be well reproduced. Only some differences in magnitude remain since I used full Mie Theory instead of Mie approximations. The methods applied for Mie scattering calculations by Pollack et al.[26, 27] (1985, 1994) were somewhat harder to comprehend due to a lacking or not so obvious description in their previous papers. Nevertheless, the recalculated Rosseland mean opacity for molecular clouds using full Mie Theory yielded values having a maximum deviation of +18.7% at temperatures before the vaporization of troilite (∼425-680 K) that can be viewed as sufficient when considering the higher change in results exerted by the influence of particle growth and porosity.

Although these calculations and simplified assumptions can serve as a good first approximation for the opacity in protostellar environments, several shortcomings should be kept in mind:

1. Considering very large particle sizes, the assumption of sphericity demanded by Mie Theory becomes invalid. Furthermore, the stability criterion by Wiscombe[37] (1980) demands that $n_{\max}$ at which the series expansion of the scattering coefficients is truncated, increases with particle radius which makes the use of full Mie Theory computational intensive.
   For large particles scattering also depends on the shape and orientation.[3] Some authors[27, 9] apply Discrete Dipole Approximation (DDA) when regarding non-spherical particles. This method first proposed by Purcell & Pennypacker[29] (1973) and further developed by Draine & Lee[9] (1984) treats the grain as a set of dipoles, but is computationally intensive.[38]

2. When using opacity tables in evolution models, a constant adjustment of the size distribution would be needed for correct modelling of disk and later protoplanetary atmosphere dynamics. Keeping this in mind, it would make sense to create efficiency tables highly resolved in particle radii that can be later used to calculate the monochromatic coefficients for different size ranges and distributions.

3. Porosity assumptions among literature vary very strongly. We do not have yet observational evidence for dust properties in protoplanetary atmospheres, although there is ongoing work to determine interstellar dust properties. In many studies, one finds high porosity assumptions of 0.8-0.9 (e.g. Mathis & Whiffen,[20] 1989; Voshchinnikov et al.,[35] 2006; Cuzzi et al.,[6] 2014) obtained by fitting their models to the extinction curve towards specific stars. Heng & Draine[12] (2009) rule out the existence of grains having porosities $\gtrsim$0.55 from diagnostics based on optical and X-ray properties of the dust halo around the galactic binary GX13+1. Considering cometary dust, density deductions indicate the existence of very high grain porosities, reaching from 0.68 to 0.975[10]. These very high porosities (>95%) in cometary dust seem to be confirmed by experiments carried out on high porosity aggregates with a nephelometer, resulting in the construction of polarimetric phase curves matching that of cometary dust.[11]

4. Refractive indices sometimes vary with measurement methods, structure (crystalline/amorphous) and show temperature dependencies, especially ices. The effect of temperature on optical constants, except for water ice (see e.g. Warren,[36] 1984; Hudgins et al.,[15] 1993) but not considered in this work, is not well studied since most of the measurements are carried out at room temperature.

5. One disadvantage in this work using EMT is that we already assume that the mass fraction of a certain species that is used later in the calculation of the monochromatic coefficients, is the same as the particle volume fraction of that species as aggregate inclusion (like in Cuzzi et al.,[6] 2014). So, when applying changes to the considered mass fraction which is especially relevant in protoplanetary atmospheres, optical constants via EMT must also be updated and the whole procedure must be repeated which is computationally time consuming. Of course, one can label this effect as 'minor' since, like mentioned before, there is yet not enough observational evidence to correctly determine sizes, porosity and composition which would probably produce higher errors in monochromatic and mean opacities than neglecting changes in prior assumed gas mass fractions.

The highest opacity is always found shortly before the vaporization of water ice near 172 K for accretion disks. The highest opacity < 425 K is obtained for compact aggregates having radii of 1-10 μm and a not so steep slope (3.1) in their size distribution, compared to the MRN SDF. Further particle growth and aggregation leads to an overall decrease in magnitude, except at very low temperatures where they exert a higher mean extinction coefficient than the typical MRN SDF. Increasing the porosity for very large particle radii can again lead to an increase in opacity.

References

[1] Armitage, P. J. (2009): Astrophysics of Planet Formation. Cambridge University Press, New York, 2010, p. 34-38, 41-49, 52, 109-140.

[2] Begemann, B., Dorschner, J., Henning, T., Mutschke, H. and Thamm, E. (1994). A laboratory approach to the interstellar sulfide dust problem. Astrophysical Journal, Part 2 - Letters, vol. 423, no. 1, p. L71-L74. http://www.astro.uni-jena.de/Laboratory/Database/jpdoc/f-dbase.html

[3] Bohren, C F. & Huffman, D. R. (1983): Absorption and Scattering of Light by Small Particles. Wiley-VCH, Berlin, p. 3-11, 22-23, 25-29, 57-63, 69-72, 79-89, 92-94, 99-111, 120, 126-129, 227-232, 306, 477.

[4] Campbell, M. J. and Ulrichs, J. (1969). Electrical properties of rocks and their significance for lunar radar observations. Journal of Geophysical Research, Volume 74, Issue 25, 5867-5881.

[5] Clayton, D. D. (1968): Principles of Stellar Evolution and Nucleosynthesis. McGraw-Hill, New York, p. 108, 170-183.

[6] Cuzzi, J. N., Estrada, P. R. and Davis, S. S. (2014): Utilitarian opacity model for aggregate particles in protoplanetary nebulae and exoplanet atmospheres. The Astrophysical Journal Supplement Series, 210-221.

[7] Dorschner, J., Begemann, B., Henning, T., Jaeger, C. and Mutschke, H. (1995). Steps toward interstellar silicate mineralogy. II. Study of Mg-Fe-silicate glasses of variable composition. Astronomy and Astrophysics, v.300, p.503-520.

[8] Durisen, R. H., Boss, A. P., Mayer, L., Nelson, A. F., Quinn, Th. and Rice, W. K. M. (2007): Gravitational Instabilities in Gaseous Protoplanetary Disks and Implications for Giant Planet Formation. Protostars and Planets V, Arizona LPI, p. 607-622.

[9] Draine, B. T. & Lee, H. M. (1984). Optical properties of interstellar graphite and silicate grains. The Astrophysical Journal, **285**, 89-108.

[10] Greenberg, J. M. & Remo, J. L. (1997). Annals of the New York Academy of Sciences, Vol. 822, Near-Earth Objects: The United Nations Conference, p. 96-117.

[11] Hadamcik, E., Levasseur-Regourd, A. C. and Worms, J. C. (2002). High porosity for cometary dust: evidence from PROGRA^2 experiment. COSPAR Colloquia Series, Vol. 15, 274-278.

[12] Heng, K. & Draine, B. T. (2009). Constraining the Porosities of Interstellar Dust Grains. arXiv:0906.0773 [astro-ph.GA], 10pp.

[13] Henning, Th. & Stognienko, R. (1996): Dust opacities for protoplanetary accretion disks: influence of dust aggregates. Astronomy & Astrophysics, 311, 291-303.

[14] Henning, Th. & Semenov, D. (2013): Chemistry in Protoplanetary Disks. Chemical Reviews, Vol. 113, No. 12, p. 9016-9042.

[15] Hudgins, D. M., Sandford, S. A., Allamandola, L. J. and Tielens, L. J. (1993). Mid- and Far-Infrared Spectroscopy of Ices: Optical Constants and Integrated Absorbances. Astrophysical Journal Supplement Series (ISSN 0067-0049), vol. 86, no. 2, p. 713-870.

[16] Lammer, H., Stökl, A., Erkaev, N. V., Dorfi, E. A., Odert, P., Güdel, M., Kulikov, Yu. N., Kislyakova, K. G. and Leitzinger, M. (2014). Origin and loss of nebula-captured hydrogen envelopes from 'sub'- to 'super-Earths' in the habitable zone of Sun-like stars. Monthly Notices of the Royal Astronomical Society, Volume 439, Issue 4, p.3225-3238.

[17] Maetzler, C. (2002): MATLAB Functions for Mie Scattering and Absorption, IAP Res. Rep. No. 2002-08, p. 1-18. Download: http://omlc.org/software/mie/maetzlermie/Maetzler2002.pdf (17.07.2017, 10:30 UTC)

[18] Maetzler, C. (2002): MATLAB Functions for Mie Scattering and Absorption - Version 2, IAP Res. Rep. No. 2002-08, p. 1-22. Download: http://www.atmo.arizona.edu/students/courselinks/spring09/atmo656b/maetzler_mie_v2.pdf (17.07.2017, 10:30 UTC)

[19] Mathis, J. S., Rumpl, W. and Nordsieck, K. H. (1977). The size distribution of interstellar grains. The Astrophysical Journal, **217**: p. 425-433.

[20] Mathis, J. S. & Whiffen, G. (1989). Composite interstellar grains. Astrophysical Journal, Part 1, Vol. 341, p. 808-822.

[21] Movshovitz, N. and Podolak, M. (2008). The opacity of grains in protoplanetary atmospheres. Icarus **194**, Issue 1, 368-378.

[22] Movshovitz, N., Bodenheimer, P., Podolak, M. and Lissauer, J. J. (2010). Formation of Jupiter using opacities based on detailed grain physics. Icarus **209**, Issue 2, 616-624.

[23] Ordal, M. A., Bell, R. J., Alexander, R. W. Jr., Newquist, L. A. and Querry, M. R. (1988). Applied Optics, Vol. 27, Issue 6, p. 1203-1209.

[24] Ossenkopf, V. (1991). Effective-medium theories for cosmic dust grains. Astronomy and Astrophysics 251, 210-219.

[25] Podolak, M. (2003). The contribution of small grans to the opacity of protoplanetary atmospheres. Icarus **165**, Issue 2, 428-437.

[26] Pollack, J. B., McKay, C. P. and Christofferson, B. M. (1985). A Calculation of the Rosseland Mean Opacity of Dust Grains in Primordial Solar System Nebulae. Icarus **64**, 471-492.

[27] Pollack, J. B., Hollenbach, D., Beckwith, S., Simonelli, D. P., Roush, T. and Fong, W. (1994). Composition and radiative properties of grains in molecular clouds and accretion disks. The Astrophysical Journal, 421, 615-639.

[28] Pollack, J. B., Hubickyj, O., Bodenheimer, P., Lissauer, J. J., Podolak, M. and Greenzweig, Y. (1996). Formation of the Giant Planets by Concurrent Accretion of Solids and Gas. Icarus **124**, 62-85.

[29] Purcell, E. M. & Pennypacker, C. R. (1973). Scattering and absorption of light by nonspherical dielectric grains. The Astrophysical Journal, **186**, 705-714.

[30] Seager, S. (2010): Exoplanet Atmospheres: Physical Processes. Princeton University Press, Princeton, New Jersey, p. 91.

[31] Semenov, D., Henning, Th., Helling, M. Ch., Ilgner and Sedlmayr, E. (2003): Rosseland and Planck Mean Opacities for Protoplanetary Discs. Astronomy & Astrophysics, 410, 611-621.

[32] Stahler, S. W. and Palla, F. (2004): The Formation of Stars. Wiley-VCH, Weinheim, First Edition, First Reprint, p. 282-368.

[33] Stökl, A., Dorfi, E. and Lammer, H. (2015). Hydrodynamic simulations of captured protoatmospheres around Earth-like planets. Astronomy & Astrophysics, Volume 576, A87, 11pp.

[34] van de Hulst, H. C. (1957): Light Scattering by Small Particles. New York, NY, Dover-Publ., Unabridged and corr. republ. of the work originally publ. in 1957 by Wiley, NQ (1981), p. 13-14.

[35] Voshchinnikov, N. V., Il'in, V. B., Henning, Th. and Dubkova, D. N. (2006). Dust extinction and absorption: the challenge of porous grains. Astronomy & Astrophysics 445, 167-177.

[36] Warren, S. G. (1984). Optical constants of ice from the ultraviolet to the microwave. Applied Optics, 23, 1206-1225.

[37] Wiscombe, W. J. (1980): Improved Mie scattering algorithms. Applied Optics, 19, p. 1505-1509.

[38] Yurkin, M. A. & Hoekstra, A. G. (2007). The discrete dipole approximation: an overview and recent developments. Journal of Quantitative Spectroscopy and Radiative Transfer, Vol. 106, Issure 1-3, 558-589.

Program codes:

[39] Mie.m, Mie_ab.m: Mätzler, C., May 2002, revised July 2002.
Code: http://omlc.ogi.edu/software/mie/maetzlermie/ (17.07.2017, 10:30 UTC)

[40] CALLBH.f, BHMIE.f: Bohren, C F. and Huffman, D. R. (1983): Absorption and Scattering of Light by Small Particles. Wiley-VCH, Berlin, 479-481.

[41] callbhmie.f, bhmie.f: Draine, B. T., Dept. Astrophysical Sciences, Princeton University. Code: https://www.astro.princeton.edu/~draine/scattering (12.08.2017, 11 UTC)

Data:

[42] Optical constants used by Pollack et al.[27] (1994) provided by Semenov, D. A. (2001): http://www2.mpia-hd.mpg.de/homes/henning/Dust_opacities/Opacities/RI/old_ri.html (25.07.2017, 15:30 UTC)

[43] Recalculated coefficients and Rosseland mean opacity for molecular clouds and a gas density of 10^{-8} g cm^{-3} by Henning & Stognienko[13] (1996, using the optical constants[42] and the Mie code from Pollack et al.[27], 1994), provided by Stognienko, R. (1996): http://www2.mpia-hd.mpg.de/homes/henning/Dust_opacities/Opacities/Ralf/pol_komp.html (25.07.2017, 15:30 UTC)

A. Appendix

A.1. Optical Constants

Optical constans for compact aggregates (Φ=0) obtained via EMT (see section 2.2) are presented in tables 10-11. The aggregate compositions relate to material species and their properties like gas mass fractions, vaporization temperatures and particle densities given in Pollack et al.[27] (1994). The optical constants for different species are available as download in [42].

Real part n of complex refractive index

λ [μm]	all	Fe+Si+FeS +Org	Fe+Si+FeS +Org (refr)	Fe+Si+FeS	Fe+Si	Fe+Ol	Ol	Si	Fe
0.1	1.4964	1.4511	1.4497	1.4201	1.4023	1.5694	1.6350	1.4299	1.1093
0.2	1.5266	1.7151	1.7285	1.9282	2.0053	1.9848	1.9396	1.9766	1.1684
0.3	1.4861	1.7414	1.7446	1.7889	1.8603	1.8820	1.7340	1.7434	1.3534
1.0	1.4434	1.6857	1.6968	1.8596	1.7657	1.8010	1.6521	1.6501	2.9408
2.0	1.4239	1.6760	1.6878	1.8634	1.7571	1.7896	1.6407	1.6415	3.2905
6.0	1.4185	1.6218	1.6256	1.6784	1.6025	1.6272	1.4846	1.4916	4.0278
7.0	1.4208	1.5941	1.5916	1.5568	1.4763	1.4815	1.3406	1.3667	4.8936
8.0	1.4090	1.5841	1.5779	1.4940	1.4107	1.4088	1.2683	1.3015	5.6764
8.5	1.4037	1.5597	1.5499	1.4210	1.3358	1.3496	1.2091	1.2267	6.0848
9.0	1.3986	1.5539	1.5433	1.3975	1.3136	1.3307	1.1925	1.2081	6.5081
10.0	1.3720	1.6479	1.6539	1.6324	1.5542	1.5870	1.4596	1.4575	7.3760
10.5	1.3276	1.6899	1.7048	1.8139	1.7378	1.7740	1.6407	1.6368	7.8096
11.0	1.2992	1.7093	1.7296	1.9759	1.9048	1.9358	1.7961	1.7978	8.2387
11.5	1.3321	1.7026	1.7228	2.0085	1.9404	1.9485	1.8070	1.8306	8.6640
12.5	1.4818	1.6814	1.6995	1.9834	1.9158	1.9100	1.7663	1.8035	9.5060
13.0	1.5474	1.6751	1.6927	1.9606	1.8917	1.9003	1.7561	1.7794	9.9243
13.5	1.5712	1.6553	1.6702	1.8905	1.8196	1.8239	1.6814	1.7086	10.3417
14.0	1.5906	1.6447	1.6582	1.8551	1.7834	1.7946	1.6526	1.6729	10.7589
15.0	1.6237	1.6695	1.6769	1.7807	1.7082	1.7251	1.5851	1.5992	11.5953
15.5	1.6256	1.6853	1.6905	1.7615	1.6893	1.7019	1.5628	1.5809	12.0173
16.5	1.6271	1.7401	1.7406	1.7480	1.6772	1.7080	1.5700	1.5701	12.8832
17.0	1.6205	1.7427	1.7439	1.7610	1.6913	1.7322	1.5946	1.5848	13.3327
18.5	1.6460	1.8448	1.8500	1.8970	1.8317	1.9127	1.7743	1.7257	14.7796
19.5	1.6533	1.8744	1.8833	1.9550	1.8903	1.9712	1.8331	1.7847	15.8510
20.5	1.6582	1.9080	1.9214	2.0356	1.9723	2.0602	1.9206	1.8656	17.0079
22.0	1.6484	1.9290	1.9495	2.1664	2.1069	2.2069	2.0632	1.9972	18.8237
23.5	1.6327	1.9509	1.9801	2.3729	2.3228	2.4574	2.3046	2.2070	20.6229
26.0	1.6103	1.9773	2.0078	2.4978	2.4573	2.5385	2.3815	2.3367	23.3692
27.0	1.6048	1.9874	2.0165	2.4979	2.4582	2.5281	2.3710	2.3370	24.3977
29.0	1.6070	2.0504	2.0759	2.4985	2.4585	2.5126	2.3549	2.3365	26.3999
30.0	1.5988	2.0554	2.0806	2.4997	2.4591	2.5089	2.3508	2.3368	27.3956
35.0	1.5436	2.2199	2.2373	2.5105	2.4661	2.5088	2.3498	2.3430	32.6822
40.5	1.5259	2.3077	2.3209	2.5197	2.4724	2.5111	2.3517	2.3489	39.1164
50.0	1.8414	2.3274	2.3386	2.5067	2.4559	2.4908	2.3320	2.3328	50.1464
100	2.0173	2.3360	2.3410	2.4111	2.3202	2.3499	2.1954	2.2002	114.135
170	2.0073	2.3216	2.3259	2.3858	2.2689	2.3155	2.1619	2.1500	222.125
400	1.9746	2.3024	2.3045	2.3326	2.2014	2.2486	2.0968	2.0840	369.221
500	1.9760	2.3005	2.3021	2.3246	2.1912	2.2402	2.0886	2.0739	416.469
800	1.9756	2.3015	2.3034	2.3286	2.1920	2.2398	2.0882	2.0748	528.011
1000	1.9752	2.3023	2.3043	2.3318	2.1944	2.2420	2.0904	2.0771	588.923
1300	1.9752	2.3023	2.3042	2.3311	2.1939	2.2424	2.0908	2.0766	668.46
2000	1.9747	2.2998	2.3017	2.3288	2.1913	2.2418	2.0901	2.0741	817.008
5000	1.9749	2.3005	2.3024	2.3295	2.1920	2.2420	2.0904	2.0747	1258.52
10000	1.9755	2.3024	2.3042	2.3293	2.1918	2.2420	2.0904	2.0745	1778.93
20000	1.9756	2.3030	2.3048	2.3293	2.1917	2.2420	2.0904	2.0745	2540.49
50000	1.9753	2.3020	2.3039	2.3307	2.1931	2.2420	2.0904	2.0758	3998.57
100000	1.9757	2.3033	2.3050	2.3295	2.1919	2.2420	2.0904	2.0746	5831.30

Table 10: Real part of complex refractive index for compact aggregates of different compositions.

Imaginary part k of complex refractive index

λ [μm]	all	Fe+Si+FeS +Org	Fe+Si+FeS +Org (refr)	Fe+Si+FeS	Fe+Si	Fe+Ol	Ol	Si	Fe
0.1	0.4181	0.9172	0.9266	1.0529	1.0937	0.9664	0.9621	1.1054	1.0000
0.2	0.0783	0.2246	0.2300	0.3203	0.2906	0.2764	0.0625	0.1221	1.5028
0.3	0.0495	0.1494	0.1533	0.2096	0.1228	0.1586	0.0264	0.0209	2.1204
1.0	0.0129	0.0383	0.0430	0.1184	0.0211	0.0271	0.0005	0.0008	4.2207
2.0	0.0077	0.0217	0.0218	0.0237	0.0084	0.0105	0.0001	0.0004	6.7248
6.0	0.0637	0.0723	0.0680	0.0064	0.0053	0.0049	0.0025	0.0035	12.0870
7.0	0.0529	0.0689	0.0649	0.0110	0.0094	0.0071	0.0056	0.0081	14.0212
8.0	0.0494	0.0695	0.0669	0.0336	0.0322	0.0253	0.0243	0.0313	16.0718
8.5	0.0525	0.0908	0.0910	0.0939	0.0942	0.0714	0.0712	0.0941	16.9952
9.0	0.0817	0.1710	0.1825	0.3234	0.3297	0.2301	0.2315	0.3311	17.8125
10.0	0.1481	0.3165	0.3501	0.8139	0.8260	0.7359	0.7239	0.8150	19.0733
10.5	0.1831	0.3010	0.3319	0.8208	0.8349	0.7100	0.6943	0.8200	19.5839
11.0	0.2344	0.2685	0.2910	0.6927	0.7068	0.6117	0.5959	0.6925	20.0938
11.5	0.2654	0.2466	0.2619	0.5393	0.5497	0.5100	0.4969	0.5386	20.6526
12.5	0.3345	0.1930	0.1924	0.1835	0.1825	0.2158	0.2104	0.1787	22.0799
13.0	0.3027	0.2036	0.1958	0.0589	0.0538	0.0458	0.0440	0.0523	22.9856
13.5	0.2618	0.2421	0.2339	0.0958	0.0918	0.0938	0.0914	0.0899	23.9792
14.0	0.2335	0.2577	0.2494	0.1125	0.1088	0.1137	0.1111	0.1068	25.0211
15.0	0.2235	0.3143	0.3073	0.2013	0.1998	0.2169	0.2133	0.1972	27.1019
15.5	0.2284	0.3564	0.3498	0.2521	0.2518	0.2653	0.2612	0.2488	28.0744
16.5	0.2148	0.3879	0.3861	0.3604	0.3627	0.3532	0.3477	0.3585	29.8422
17.0	0.2049	0.3899	0.3920	0.4220	0.4256	0.4116	0.4047	0.4204	30.6503
18.5	0.1741	0.3823	0.3988	0.6405	0.6498	0.6300	0.6150	0.6385	32.8462
19.5	0.1638	0.3860	0.4092	0.7597	0.7722	0.7557	0.7361	0.7573	34.1795
20.5	0.1463	0.3652	0.3926	0.8291	0.8439	0.8467	0.8228	0.8262	35.4766
22.0	0.1299	0.3511	0.3789	0.8700	0.8872	0.9146	0.8863	0.8668	37.4790
23.5	0.1167	0.3326	0.3570	0.8613	0.8814	0.9128	0.8817	0.8590	39.6932
26.0	0.1350	0.3883	0.4034	0.7328	0.7461	0.7935	0.7662	0.7265	43.9664
27.0	0.1458	0.4093	0.4204	0.6571	0.6650	0.7234	0.6988	0.6477	45.7302
29.0	0.1607	0.4226	0.4280	0.5351	0.5342	0.5800	0.5605	0.5204	49.0386
30.0	0.1690	0.4274	0.4304	0.4891	0.4848	0.5161	0.4989	0.4724	50.5013
35.0	0.1831	0.3289	0.3294	0.3382	0.3212	0.3142	0.3038	0.3130	57.0121
40.5	0.4162	0.2842	0.2833	0.2681	0.2415	0.2416	0.2337	0.2354	65.3905
50.0	0.4981	0.2503	0.2504	0.2510	0.2175	0.2281	0.2207	0.2121	79.6328
100	0.1330	0.1615	0.1643	0.2055	0.1551	0.1664	0.1615	0.1515	146.507
170	0.0778	0.1063	0.1094	0.1543	0.1125	0.1142	0.1109	0.1100	228.107
400	0.0195	0.0453	0.0472	0.0752	0.0494	0.0499	0.0485	0.0484	377.062
500	0.0137	0.0307	0.0327	0.0613	0.0398	0.0404	0.0392	0.0389	425.374
800	0.0076	0.0154	0.0174	0.0447	0.0287	0.0282	0.0274	0.0281	527.635
1000	0.0064	0.0135	0.0154	0.0414	0.0286	0.0278	0.0270	0.0280	580.033
1300	0.0056	0.0123	0.0140	0.0376	0.0287	0.0280	0.0272	0.0281	651.580
2000	0.0045	0.0109	0.0124	0.0335	0.0288	0.0286	0.0278	0.0281	801.145
5000	0.0035	0.0098	0.0112	0.0302	0.0287	0.0287	0.0279	0.0280	1279.99
10000	0.0030	0.0088	0.0100	0.0270	0.0261	0.0255	0.0248	0.0255	1786.06
20000	0.0026	0.0077	0.0088	0.0238	0.0231	0.0218	0.0212	0.0226	2573.68
50000	0.0023	0.0070	0.0080	0.0216	0.0211	0.0191	0.0186	0.0206	4150.85
100000	0.0022	0.0071	0.0080	0.0213	0.0207	0.0184	0.0179	0.0203	6111.45

Table 11: Imaginary part of complex refractive index for compact aggregates of different compositions.

A.2. Monochromatic Coefficients

Recalculated radiation pressure coefficients for material species taken from Pollack et al.[27] (1994) are shown in table 12. Note that these monochromatic coefficients are not yet multiplied with their gas mass fraction f.

Monochromatic radiation pressure coefficient κ_ν [cm^2/g]

λ [μm]	Material species						
	Iron	Olivine	Orthopyroxene	Troilite	Organics refr.	Organics vol.	Water ice
0.1	17403.0385	35257.7633	50764.8036	23307.1600	79344.3647	119016.5470	50510.7208
0.2	17095.4052	14317.9314	19886.1028	20060.0333	33906.1210	50859.1816	16185.9838
0.3	13672.2355	8728.1434	8223.2646	17805.6264	25750.1760	38625.2640	9482.8858
1.0	4978.5899	3114.2538	3169.6504	9916.4420	7465.1081	11197.6622	3235.6980
2.0	2827.8014	1687.6529	1764.8375	5188.8886	4260.8787	6391.3181	1345.0981
6.0	981.2251	203.9055	256.5451	2127.1854	1729.2288	2593.8432	1540.1896
7.0	787.6550	95.6273	208.3457	1803.7993	1364.9928	2047.4892	1026.2180
8.0	633.2329	134.9791	312.2375	1506.0655	1074.9535	1612.4303	763.4778
9.0	517.7167	872.9519	2425.3087	1228.3030	1007.4115	1511.1172	553.8872
10.0	432.2360	2074.2578	3137.5026	973.2260	1035.3659	1553.0488	906.3398
10.5	397.6439	1727.4929	2908.0219	869.3039	1015.3938	1523.0908	1700.2208
11.0	366.9850	1339.9016	2132.4002	781.5563	1042.3767	1563.5650	2758.4080
11.5	339.4686	1089.7219	1401.9122	707.8155	1073.5861	1610.3792	3199.9617
12.5	291.5740	488.0117	221.1949	591.9188	1112.6799	1669.0198	3894.3761
13.0	270.5261	155.1944	241.3967	544.5760	1296.6171	1944.9257	3145.8013
13.5	251.3320	228.0019	226.3106	502.1166	1430.9682	2146.4523	2288.5181
14.0	233.9419	252.1643	223.7439	463.6010	1445.8587	2168.7881	1756.4024
15.0	204.2237	413.3809	287.6584	396.6132	1498.8068	2248.2102	1243.9625
15.5	191.6814	483.8516	384.4657	368.0856	1571.9397	2357.9095	1085.4255
16.5	170.4409	586.9508	677.9505	320.4017	1416.7501	2125.1252	802.4236
17.0	161.4210	645.9193	783.0452	300.7405	1303.8512	1955.7768	680.8867
18.5	139.3011	771.8295	1022.1849	254.8464	889.7080	1334.5621	429.9731
19.5	127.7670	817.2882	1053.1199	232.0777	751.2165	1126.8248	325.6609
20.5	118.0783	797.1309	969.9165	213.2097	604.1805	906.2707	242.9564
22.0	105.8578	706.3693	816.6619	189.9690	532.3621	798.5431	154.4117
23.5	95.3524	554.8947	680.6239	171.2804	505.4314	758.1470	111.3487
26.0	80.2554	418.0706	403.0871	146.8055	639.6846	959.5268	134.6079
27.0	75.1140	372.3778	314.9556	138.4644	678.2142	1017.3213	166.3977
29.0	66.4370	284.8543	226.6873	123.6634	653.5055	980.2582	248.7805
30.0	62.8659	246.8240	210.6590	117.1598	650.3040	975.4560	285.2833
35.0	50.0929	129.0252	151.3259	93.3614	375.9608	563.9412	513.8944
40.5	40.9408	84.0618	89.6351	79.2420	260.6910	391.0365	1474.9602
50.0	31.6515	63.1161	54.0474	63.4868	174.5033	261.7549	1111.8927
82.3	20.1579	33.7465	21.9698	44.0357	69.2102	103.8154	158.6007
100.0	17.0478	24.8487	18.3042	36.5249	47.6379	71.4569	94.2048
170.0	11.6257	10.2714	10.6256	16.8873	17.1345	25.7017	30.0293
268.1	7.5001	4.4391	5.0302	8.4296	6.8300	10.2449	4.2963
300.4	6.7565	3.4464	3.9812	6.9422	5.5324	8.2987	2.7800
400.0	5.1898	2.0138	2.1443	4.4882	2.7943	4.1914	1.6334
500.0	4.1801	1.3127	1.3715	3.0188	1.2491	1.8737	0.9985
800.0	2.6547	0.5727	0.6808	1.3919	0.1767	0.2651	0.4104
1000	2.1256	0.4508	0.5569	0.8786	9.71e-02	0.1456	0.2625
1300	1.6136	0.3494	0.4263	0.4565	6.90e-02	0.1035	0.1596
2000	0.9835	0.2321	0.2652	0.1459	3.96e-02	5.95e-02	6.71e-02
5000	0.2972	9.32e-02	0.1031	1.17e-02	1.41e-02	2.12e-02	1.14e-02
10000	0.1097	4.15e-02	5.04e-02	2.01e-03	6.22e-03	9.34e-03	3.64e-03
20000	3.76e-02	1.77e-02	2.46e-02	4.17e-04	2.63e-03	3.94e-03	1.43e-03
50000	8.01e-03	6.21e-03	9.74e-03	7.00e-05	9.67e-04	1.45e-03	2.05e-04
100000	2.39e-03	2.99e-03	5.02e-03	1.72e-05	5.58e-04	8.37e-04	3.64e-05

Table 12: Monochromatic radiation pressure coefficient for different material species as defined in density and optical constants in Pollack et al.[27] (1994). These coefficients are not yet multiplied by their individual gas mass fraction f.

A.3. Mean Coefficients

Tables 13-22 contain recalculated Rosseland and Planck mean opacities using optical constants data by Pollack et al.[27] (1994) and Semenov et al. [31] (2003) and a MRN size distribution function (see definition (4.1) in section 4.1) assuming compact spherical and homogeneous particles. Unusual temperatures listed often relate to vaporization temperatures at different gas densities (see table 2 in section 4.2 defined by Pollack et al.[27], 1994).

T [K]	Rosseland mean extinction coefficients [cm²/g] ρ [g cm⁻³] 10^{-18}	10^{-16}	10^{-14}	10^{-12}	10^{-10}	10^{-8}	10^{-6}	10^{-4}
10	0.0165	0.0165	0.0165	0.0165	0.0165	0.0165	0.0165	0.0165
20	0.0653	0.0653	0.0653	0.0653	0.0653	0.0653	0.0653	0.0653
40	0.2700	0.2700	0.2700	0.2700	0.2700	0.2700	0.2700	0.2700
60	0.6225	0.6225	0.6225	0.6225	0.6225	0.6225	0.6225	0.6225
80	1.1005	1.1005	1.1005	1.1005	1.1005	1.1005	1.1005	1.1005
100	1.6673	1.6673	1.6673	1.6673	1.6673	1.6673	1.6673	1.6673
106	1.8501	1.8501	1.8501	1.8501	1.8501	1.8501	1.8501	1.8501
115	1.5026	2.1332	2.1332	2.1332	2.1332	2.1332	2.1332	2.1332
125	1.7475	1.7475	2.4583	2.4583	2.4583	2.4583	2.4583	2.4583
138	2.0827	2.0827	2.0827	2.8934	2.8934	2.8934	2.8934	2.8934
153	2.4866	2.4866	2.4866	2.4866	3.4059	3.4059	3.4059	3.4059
172	3.0105	3.0105	3.0105	3.0105	3.0105	4.0562	4.0562	4.0562
197	3.6931	3.6931	3.6931	3.6931	3.6931	3.6931	4.8819	4.8819
200	3.7730	3.7730	3.7730	3.7730	3.7730	3.7730	3.7730	4.9769
230	4.5328	4.5328	4.5328	4.5328	4.5328	4.5328	4.5328	5.8633
300	5.9660	5.9660	5.9660	5.9660	5.9660	5.9660	5.9660	5.9660
375	7.0904	7.0904	7.0904	7.0904	7.0904	7.0904	7.0904	7.0904
400	6.3770	6.3770	6.3770	6.3770	6.3770	6.3770	6.3770	6.3770
500	7.4130	7.4130	7.4130	7.4130	7.4130	7.4130	7.4130	7.4130
575	8.1939	8.1939	8.1939	8.1939	8.1939	8.1939	8.1939	8.1939
680	2.9847	2.9847	2.9847	2.9847	2.9847	2.9847	2.9847	2.9847
700	2.0732	2.0732	2.0732	2.0732	2.0732	2.0732	2.0732	2.0732
835	2.4518	2.4518	2.4518	2.4518	2.4518	2.4518	2.4518	2.4518
908	1.6853	2.6748	2.6748	2.6748	2.6748	2.6748	2.6748	2.6748
920	1.7117	1.7117	2.7125	2.7125	2.7125	2.7125	2.7125	2.7125
929	1.2394	1.7316	2.7409	2.7409	2.7409	2.7409	2.7409	2.7409
980		1.8470	2.9044	2.9044	2.9044	2.9044	2.9044	2.9044
994		1.3515	2.9500	2.9500	2.9500	2.9500	2.9500	2.9500
997		1.3568	1.8864	2.9599	2.9599	2.9599	2.9599	2.9599
1049			2.0095	3.1318	3.1318	3.1318	3.1318	3.1318
1076			1.5000	3.2225	3.2225	3.2225	3.2225	3.2225
1100				3.3037	3.3037	3.3037	3.3037	3.3037
1129				2.2056	3.4027	3.4027	3.4027	3.4027
1168				1.6744	3.5370	3.5370	3.5370	3.5370
1222					3.7249	3.7249	3.7249	3.7249
1230					3.1003	3.7529	3.7529	3.7529
1277					1.8896	3.9183	3.9183	3.9183
1331						4.1096	4.1096	4.1096
1395						3.5852	4.3378	4.3378
1408						2.1574	4.3843	4.3843
1462							4.5778	4.5778
1570							4.1045	4.9656
1612							1.3470	5.1164
1621								5.1486
1774								4.7075
1908								1.5963

Table 13: Rosseland mean extinction coefficients [cm^2/g] for molecular clouds recalculated from optical constants data of Pollack et al.[27] (1994).

Planck mean extinction coefficients [cm^2/g]

T [K]	ρ [g cm^{-3}] 10^{-18}	10^{-16}	10^{-14}	10^{-12}	10^{-10}	10^{-8}	10^{-6}	10^{-4}
10	0.0387	0.0387	0.0387	0.0387	0.0387	0.0387	0.0387	0.0387
20	0.1659	0.1659	0.1659	0.1659	0.1659	0.1659	0.1659	0.1659
40	0.7283	0.7283	0.7283	0.7283	0.7283	0.7283	0.7283	0.7283
60	1.4906	1.4906	1.4906	1.4906	1.4906	1.4906	1.4906	1.4906
80	2.2489	2.2489	2.2489	2.2489	2.2489	2.2489	2.2489	2.2489
100	3.0112	3.0112	3.0112	3.0112	3.0112	3.0112	3.0112	3.0112
106	3.2439	3.2439	3.2439	3.2439	3.2439	3.2439	3.2439	3.2439
115	2.8666	3.5960	3.5960	3.5960	3.5960	3.5960	3.5960	3.5960
125	3.2346	3.2346	3.9891	3.9891	3.9891	3.9891	3.9891	3.9891
138	3.6952	3.6952	3.6952	4.4970	4.4970	4.4970	4.4970	4.4970
153	4.1946	4.1946	4.1946	4.1946	5.0672	5.0672	5.0672	5.0672
172	4.7706	4.7706	4.7706	4.7706	4.7706	5.7456	5.7456	5.7456
197	5.4272	5.4272	5.4272	5.4272	5.4272	5.4272	6.5368	6.5368
200	5.4984	5.4984	5.4984	5.4984	5.4984	5.4984	5.4984	6.6232
230	6.1278	6.1278	6.1278	6.1278	6.1278	6.1278	6.1278	7.3855
300	7.1503	7.1503	7.1503	7.1503	7.1503	7.1503	7.1503	7.1503
375	7.9047	7.9047	7.9047	7.9047	7.9047	7.9047	7.9047	7.9047
400	7.0627	7.0627	7.0627	7.0627	7.0627	7.0627	7.0627	7.0627
500	7.8820	7.8820	7.8820	7.8820	7.8820	7.8820	7.8820	7.8820
575	8.5986	8.5986	8.5986	8.5986	8.5986	8.5986	8.5986	8.5986
680	3.5088	3.5088	3.5088	3.5088	3.5088	3.5088	3.5088	3.5088
700	2.7016	2.7016	2.7016	2.7016	2.7016	2.7016	2.7016	2.7016
835	3.0638	3.0638	3.0638	3.0638	3.0638	3.0638	3.0638	3.0638
908	2.4362	3.2972	3.2972	3.2972	3.2972	3.2972	3.2972	3.2972
920	2.4647	2.4647	3.3373	3.3373	3.3373	3.3373	3.3373	3.3373
929	1.8486	2.4864	3.3677	3.3677	3.3677	3.3677	3.3677	3.3677
980		2.6139	3.5442	3.5442	3.5442	3.5442	3.5442	3.5442
994		1.9813	3.5938	3.5938	3.5938	3.5938	3.5938	3.5938
997		1.9876	2.6579	3.6044	3.6044	3.6044	3.6044	3.6044
1049			2.7964	3.7920	3.7920	3.7920	3.7920	3.7920
1076			2.1581	3.8910	3.8910	3.8910	3.8910	3.8910
1100				3.9798	3.9798	3.9798	3.9798	3.9798
1129				3.0184	4.0879	4.0879	4.0879	4.0879
1168				2.3641	4.2344	4.2344	4.2344	4.2344
1222					4.4386	4.4386	4.4386	4.4386
1230					3.6663	4.4689	4.4689	4.4689
1277					2.6134	4.6475	4.6475	4.6475
1331						4.8527	4.8527	4.8527
1395						4.1898	5.0953	5.0953
1408						2.9145	5.1445	5.1445
1462							5.3479	5.3479
1570							4.7343	5.7505
1612							1.4862	5.9052
1621								5.9382
1774								5.3470
1908								1.7180

Table 14: Planck mean extinction coefficients [cm^2/g] for molecular clouds recalculated from optical constants data of Pollack et al.[27] (1994).

Rosseland mean extinction coefficients [cm^2/g]

T [K]	ρ [g cm^{-3}] 10^{-18}	10^{-16}	10^{-14}	10^{-12}	10^{-10}	10^{-8}	10^{-6}	10^{-4}
10	0.0218	0.0218	0.0218	0.0218	0.0218	0.0218	0.0218	0.0218
20	0.0924	0.0924	0.0924	0.0924	0.0924	0.0924	0.0924	0.0924
40	0.4360	0.4360	0.4360	0.4360	0.4360	0.4360	0.4360	0.4360
60	1.0915	1.0915	1.0915	1.0915	1.0915	1.0915	1.0915	1.0915
80	1.9762	1.9762	1.9762	1.9762	1.9762	1.9762	1.9762	1.9762
100	2.9429	2.9429	2.9429	2.9429	2.9429	2.9429	2.9429	2.9429
109	3.3847	3.3847	3.3847	3.3847	3.3847	3.3847	3.3847	3.3847
118	1.6081	3.8289	3.8289	3.8289	3.8289	3.8289	3.8289	3.8289
129	1.8880	1.8880	4.3757	4.3757	4.3757	4.3757	4.3757	4.3757
143	2.2629	2.2629	2.2629	5.0781	5.0781	5.0781	5.0781	5.0781
159	2.7082	2.7082	2.7082	2.7082	5.8854	5.8854	5.8854	5.8854
180	3.3022	3.3022	3.3022	3.3022	3.3022	6.9330	6.9330	6.9330
200	3.8583	3.8583	3.8583	3.8583	3.8583	3.8583	7.8883	7.8883
207	4.0475	4.0475	4.0475	4.0475	4.0475	4.0475	8.2075	8.2075
244	4.9776	4.9776	4.9776	4.9776	4.9776	4.9776	4.9776	9.7236
275	5.6520	5.6520	5.6520	5.6520	5.6520	5.6520	5.6520	5.6520
300	5.3073	5.3073	5.3073	5.3073	5.3073	5.3073	5.3073	5.3073
400	6.6080	6.6080	6.6080	6.6080	6.6080	6.6080	6.6080	6.6080
425	6.8879	6.8879	6.8879	6.8879	6.8879	6.8879	6.8879	6.8879
500	2.6539	2.6539	2.6539	2.6539	2.6539	2.6539	2.6539	2.6539
680	3.3729	3.3729	3.3729	3.3729	3.3729	3.3729	3.3729	3.3729
700	2.1415	2.1415	2.1415	2.1415	2.1415	2.1415	2.1415	2.1415
835	2.5332	2.5332	2.5332	2.5332	2.5332	2.5332	2.5332	2.5332
908	1.7720	2.7643	2.7643	2.7643	2.7643	2.7643	2.7643	2.7643
920	1.7997	1.7997	2.8033	2.8033	2.8033	2.8033	2.8033	2.8033
929	1.3036	1.8207	2.8328	2.8328	2.8328	2.8328	2.8328	2.8328
980		1.9420	3.0023	3.0023	3.0023	3.0023	3.0023	3.0023
994		1.4215	3.0496	3.0496	3.0496	3.0496	3.0496	3.0496
997		1.4271	1.9835	3.0598	3.0598	3.0598	3.0598	3.0598
1049			2.1129	3.2382	3.2382	3.2382	3.2382	3.2382
1076			1.5777	3.3323	3.3323	3.3323	3.3323	3.3323
1100				3.4166	3.4166	3.4166	3.4166	3.4166
1129				2.3190	3.5193	3.5193	3.5193	3.5193
1168				1.7612	3.6587	3.6587	3.6587	3.6587
1222					3.8538	3.8538	3.8538	3.8538
1230					3.1980	3.8829	3.8829	3.8829
1277					1.9875	4.0547	4.0547	4.0547
1331						4.2534	4.2534	4.2534
1395						3.7005	4.4905	4.4905
1408						2.2692	4.5388	4.5388
1462							4.7399	4.7399
1570							4.2391	5.1430
1612							1.3470	5.2998
1621								5.3334
1774								4.8647
1908								1.5963

Table 15: Same as table 13 but for accretion disks.

Planck mean extinction coefficients [cm^2/g]

T [K]	ρ [g cm^{-3}] 10^{-18}	10^{-16}	10^{-14}	10^{-12}	10^{-10}	10^{-8}	10^{-6}	10^{-4}
10	0.0603	0.0603	0.0603	0.0603	0.0603	0.0603	0.0603	0.0603
20	0.3283	0.3283	0.3283	0.3283	0.3283	0.3283	0.3283	0.3283
40	1.8690	1.8690	1.8690	1.8690	1.8690	1.8690	1.8690	1.8690
60	3.6554	3.6554	3.6554	3.6554	3.6554	3.6554	3.6554	3.6554
80	4.7986	4.7986	4.7986	4.7986	4.7986	4.7986	4.7986	4.7986
100	5.6557	5.6557	5.6557	5.6557	5.6557	5.6557	5.6557	5.6557
109	6.0503	6.0503	6.0503	6.0503	6.0503	6.0503	6.0503	6.0503
118	3.0409	6.4728	6.4728	6.4728	6.4728	6.4728	6.4728	6.4728
129	3.4513	3.4513	7.0303	7.0303	7.0303	7.0303	7.0303	7.0303
143	3.9506	3.9506	3.9506	7.7927	7.7927	7.7927	7.7927	7.7927
159	4.4826	4.4826	4.4826	4.4826	8.6986	8.6986	8.6986	8.6986
180	5.1108	5.1108	5.1108	5.1108	5.1108	9.8641	9.8641	9.8641
200	5.6333	5.6333	5.6333	5.6333	5.6333	5.6333	10.8793	10.8793
207	5.7993	5.7993	5.7993	5.7993	5.7993	5.7993	11.2047	11.2047
244	6.5461	6.5461	6.5461	6.5461	6.5461	6.5461	6.5461	12.6418
275	7.0331	7.0331	7.0331	7.0331	7.0331	7.0331	7.0331	7.0331
300	6.4380	6.4380	6.4380	6.4380	6.4380	6.4380	6.4380	6.4380
400	7.3282	7.3282	7.3282	7.3282	7.3282	7.3282	7.3282	7.3282
425	7.5348	7.5348	7.5348	7.5348	7.5348	7.5348	7.5348	7.5348
500	3.3498	3.3498	3.3498	3.3498	3.3498	3.3498	3.3498	3.3498
680	3.9099	3.9099	3.9099	3.9099	3.9099	3.9099	3.9099	3.9099
700	2.8071	2.8071	2.8071	2.8071	2.8071	2.8071	2.8071	2.8071
835	3.1808	3.1808	3.1808	3.1808	3.1808	3.1808	3.1808	3.1808
908	2.5615	3.4225	3.4225	3.4225	3.4225	3.4225	3.4225	3.4225
920	2.5915	2.5915	3.4641	3.4641	3.4641	3.4641	3.4641	3.4641
929	1.9443	2.6143	3.4957	3.4957	3.4957	3.4957	3.4957	3.4957
980		2.7484	3.6787	3.6787	3.6787	3.6787	3.6787	3.6787
994		2.0840	3.7301	3.7301	3.7301	3.7301	3.7301	3.7301
997		2.0906	2.7947	3.7412	3.7412	3.7412	3.7412	3.7412
1049			2.9404	3.9359	3.9359	3.9359	3.9359	3.9359
1076			2.2699	4.0387	4.0387	4.0387	4.0387	4.0387
1100				4.1310	4.1310	4.1310	4.1310	4.1310
1129				3.1737	4.2433	4.2433	4.2433	4.2433
1168				2.4865	4.3955	4.3955	4.3955	4.3955
1222					4.6077	4.6077	4.6077	4.6077
1230					3.7961	4.6392	4.6392	4.6392
1277					2.7487	4.8248	4.8248	4.8248
1331						5.0382	5.0382	5.0382
1395						4.3392	5.2905	5.2905
1408						3.0654	5.3416	5.3416
1462							5.5531	5.5531
1570							4.9043	5.9718
1612							1.4862	6.1327
1621								6.1670
1774								5.5402
1908								1.7180

Table 16: Same as table 14 but for accretion disks.

	Rosseland mean extinction coefficients [cm^2/g]							
T [K]	ρ [g cm^{-3}]							
	10^{-18}	10^{-16}	10^{-14}	10^{-12}	10^{-10}	10^{-8}	10^{-6}	10^{-4}
10	0.0170	0.0170	0.0170	0.0170	0.0170	0.0170	0.0170	0.0170
20	0.0749	0.0749	0.0749	0.0749	0.0749	0.0749	0.0749	0.0749
40	0.3389	0.3389	0.3389	0.3389	0.3389	0.3389	0.3389	0.3389
60	0.8473	0.8473	0.8473	0.8473	0.8473	0.8473	0.8473	0.8473
80	1.5836	1.5836	1.5836	1.5836	1.5836	1.5836	1.5836	1.5836
100	2.4800	2.4800	2.4800	2.4800	2.4800	2.4800	2.4800	2.4800
109	2.9224	2.9224	2.9224	2.9224	2.9224	2.9224	2.9224	2.9224
118	1.6979	3.3855	3.3855	3.3855	3.3855	3.3855	3.3855	3.3855
129	2.0163	2.0163	3.9758	3.9758	3.9758	3.9758	3.9758	3.9758
143	2.4454	2.4454	2.4454	4.7573	4.7573	4.7573	4.7573	4.7573
159	2.9574	2.9574	2.9574	2.9574	5.6724	5.6724	5.6724	5.6724
180	3.6403	3.6403	3.6403	3.6403	3.6403	6.8601	6.8601	6.8601
200	4.2761	4.2761	4.2761	4.2761	4.2761	4.2761	7.9185	7.9185
207	4.4910	4.4910	4.4910	4.4910	4.4910	4.4910	8.2630	8.2630
244	5.5320	5.5320	5.5320	5.5320	5.5320	5.5320	5.5320	9.8120
275	6.2666	6.2666	6.2666	6.2666	6.2666	6.2666	6.2666	6.2666
300	5.9294	5.9294	5.9294	5.9294	5.9294	5.9294	5.9294	5.9294
400	7.2791	7.2791	7.2791	7.2791	7.2791	7.2791	7.2791	7.2791
425	7.5659	7.5659	7.5659	7.5659	7.5659	7.5659	7.5659	7.5659
500	3.2626	3.2626	3.2626	3.2626	3.2626	3.2626	3.2626	3.2626
680	4.0538	4.0538	4.0538	4.0538	4.0538	4.0538	4.0538	4.0538
700	2.5663	2.5663	2.5663	2.5663	2.5663	2.5663	2.5663	2.5663
835	3.0366	3.0366	3.0366	3.0366	3.0366	3.0366	3.0366	3.0366
908	2.3328	3.3153	3.3153	3.3153	3.3153	3.3153	3.3153	3.3153
920	2.3690	2.3690	3.3624	3.3624	3.3624	3.3624	3.3624	3.3624
929	1.8482	2.3963	3.3980	3.3980	3.3980	3.3980	3.3980	3.3980
980		2.5544	3.6030	3.6030	3.6030	3.6030	3.6030	3.6030
994		2.0160	3.6602	3.6602	3.6602	3.6602	3.6602	3.6602
997		2.0239	2.6082	3.6725	3.6725	3.6725	3.6725	3.6725
1049			2.7763	3.8884	3.8884	3.8884	3.8884	3.8884
1076			2.2370	4.0023	4.0023	4.0023	4.0023	4.0023
1100				4.1044	4.1044	4.1044	4.1044	4.1044
1129				3.0436	4.2289	4.2289	4.2289	4.2289
1168				2.4953	4.3980	4.3980	4.3980	4.3980
1222					4.6348	4.6348	4.6348	4.6348
1230					3.9607	4.6701	4.6701	4.6701
1277					2.8126	4.8787	4.8787	4.8787
1331						5.1203	5.1203	5.1203
1395						4.6012	5.4087	5.4087
1408						3.2057	5.4675	5.4675
1462							5.7123	5.7123
1570							5.2886	6.2037
1612							1.2912	6.3949
1621								6.4359
1774								6.0883
1908								1.5447

Table 17: Recalculation for Fe/(Fe+Mg)=0.3 ("normal" silicates; nrm) from optical constants data from Semenov et al.[31] (2003).

Planck mean extinction coefficients [cm^2/g]

T [K]	ρ [g cm^{-3}] 10^{-18}	10^{-16}	10^{-14}	10^{-12}	10^{-10}	10^{-8}	10^{-6}	10^{-4}
10	0.0532	0.0532	0.0532	0.0532	0.0532	0.0532	0.0532	0.0532
20	0.2461	0.2461	0.2461	0.2461	0.2461	0.2461	0.2461	0.2461
40	1.5433	1.5433	1.5433	1.5433	1.5433	1.5433	1.5433	1.5433
60	3.2187	3.2187	3.2187	3.2187	3.2187	3.2187	3.2187	3.2187
80	4.5084	4.5084	4.5084	4.5084	4.5084	4.5084	4.5084	4.5084
100	5.7357	5.7357	5.7357	5.7357	5.7357	5.7357	5.7357	5.7357
109	6.3408	6.3408	6.3408	6.3408	6.3408	6.3408	6.3408	6.3408
118	3.6640	6.9845	6.9845	6.9845	6.9845	6.9845	6.9845	6.9845
129	4.1541	4.1541	7.8119	7.8119	7.8119	7.8119	7.8119	7.8119
143	4.7427	4.7427	4.7427	8.8940	8.8940	8.8940	8.8940	8.8940
159	5.3582	5.3582	5.3582	5.3582	10.1078	10.1078	10.1078	10.1078
180	6.0669	6.0669	6.0669	6.0669	6.0669	11.5624	11.5624	11.5624
200	6.6392	6.6392	6.6392	6.6392	6.6392	6.6392	12.7324	12.7324
207	6.8173	6.8173	6.8173	6.8173	6.8173	6.8173	13.0871	13.0871
244	7.5944	7.5944	7.5944	7.5944	7.5944	7.5944	7.5944	14.5164
275	8.0768	8.0768	8.0768	8.0768	8.0768	8.0768	8.0768	8.0768
300	7.4658	7.4658	7.4658	7.4658	7.4658	7.4658	7.4658	7.4658
400	8.2709	8.2709	8.2709	8.2709	8.2709	8.2709	8.2709	8.2709
425	8.4601	8.4601	8.4601	8.4601	8.4601	8.4601	8.4601	8.4601
500	4.1771	4.1771	4.1771	4.1771	4.1771	4.1771	4.1771	4.1771
680	4.7035	4.7035	4.7035	4.7035	4.7035	4.7035	4.7035	4.7035
700	3.4389	3.4389	3.4389	3.4389	3.4389	3.4389	3.4389	3.4389
835	3.8730	3.8730	3.8730	3.8730	3.8730	3.8730	3.8730	3.8730
908	3.3154	4.1600	4.1600	4.1600	4.1600	4.1600	4.1600	4.1600
920	3.3532	3.3532	4.2097	4.2097	4.2097	4.2097	4.2097	4.2097
929	2.7274	3.3820	4.2474	4.2474	4.2474	4.2474	4.2474	4.2474
980		3.5517	4.4668	4.4668	4.4668	4.4668	4.4668	4.4668
994		2.9161	4.5285	4.5285	4.5285	4.5285	4.5285	4.5285
997		2.9251	3.6104	4.5418	4.5418	4.5418	4.5418	4.5418
1049			3.7953	4.7763	4.7763	4.7763	4.7763	4.7763
1076			3.1683	4.9005	4.9005	4.9005	4.9005	4.9005
1100				5.0120	5.0120	5.0120	5.0120	5.0120
1129				4.0925	5.1480	5.1480	5.1480	5.1480
1168				3.4631	5.3325	5.3325	5.3325	5.3325
1222					5.5902	5.5902	5.5902	5.5902
1230					4.8130	5.6286	5.6286	5.6286
1277					3.8209	5.8544	5.8544	5.8544
1331						6.1143	6.1143	6.1143
1395						5.5020	6.4222	6.4222
1408						4.2540	6.4846	6.4846
1462							6.7430	6.7430
1570							6.2208	7.2551
1612							1.4708	7.4521
1621								7.4941
1774								7.0305
1908								1.7021

Table 18: Recalculation for Fe/(Fe+Mg)=0.3 ("normal"; nrm) from optical constants data from Semenov et al.[31] (2003).

Rosseland mean extinction coefficients [cm^2/g]

T [K]	ρ [g cm^{-3}] 10^{-18}	10^{-16}	10^{-14}	10^{-12}	10^{-10}	10^{-8}	10^{-6}	10^{-4}
10	0.0220	0.0220	0.0220	0.0220	0.0220	0.0220	0.0220	0.0220
20	0.0879	0.0879	0.0879	0.0879	0.0879	0.0879	0.0879	0.0879
40	0.3710	0.3710	0.3710	0.3710	0.3710	0.3710	0.3710	0.3710
60	0.9018	0.9018	0.9018	0.9018	0.9018	0.9018	0.9018	0.9018
80	1.6465	1.6465	1.6465	1.6465	1.6465	1.6465	1.6465	1.6465
100	2.5218	2.5218	2.5218	2.5218	2.5218	2.5218	2.5218	2.5218
109	2.9452	2.9452	2.9452	2.9452	2.9452	2.9452	2.9452	2.9452
118	1.6779	3.3844	3.3844	3.3844	3.3844	3.3844	3.3844	3.3844
129	1.9740	1.9740	3.9406	3.9406	3.9406	3.9406	3.9406	3.9406
143	2.3696	2.3696	2.3696	4.6740	4.6740	4.6740	4.6740	4.6740
159	2.8388	2.8388	2.8388	2.8388	5.5338	5.5338	5.5338	5.5338
180	3.4646	3.4646	3.4646	3.4646	3.4646	6.6604	6.6604	6.6604
200	4.0528	4.0528	4.0528	4.0528	4.0528	4.0528	7.6846	7.6846
207	4.2539	4.2539	4.2539	4.2539	4.2539	4.2539	8.0240	8.0240
244	5.2524	5.2524	5.2524	5.2524	5.2524	5.2524	5.2524	9.6015
275	5.9897	5.9897	5.9897	5.9897	5.9897	5.9897	5.9897	5.9897
300	5.6723	5.6723	5.6723	5.6723	5.6723	5.6723	5.6723	5.6723
400	7.1490	7.1490	7.1490	7.1490	7.1490	7.1490	7.1490	7.1490
425	7.4627	7.4627	7.4627	7.4627	7.4627	7.4627	7.4627	7.4627
500	3.2222	3.2222	3.2222	3.2222	3.2222	3.2222	3.2222	3.2222
680	4.0375	4.0375	4.0375	4.0375	4.0375	4.0375	4.0375	4.0375
700	2.6764	2.6764	2.6764	2.6764	2.6764	2.6764	2.6764	2.6764
835	3.1070	3.1070	3.1070	3.1070	3.1070	3.1070	3.1070	3.1070
908	1.3591	3.3562	3.3562	3.3562	3.3562	3.3562	3.3562	3.3562
920	1.3791	1.3791	3.3980	3.3980	3.3980	3.3980	3.3980	3.3980
929	0.4106	1.3943	3.4296	3.4296	3.4296	3.4296	3.4296	3.4296
980		1.4822	3.6103	3.6103	3.6103	3.6103	3.6103	3.6103
994		0.4439	3.6605	3.6605	3.6605	3.6605	3.6605	3.6605
997		0.4454	1.5122	3.6713	3.6713	3.6713	3.6713	3.6713
1049			1.6060	3.8598	3.8598	3.8598	3.8598	3.8598
1076			0.4875	3.9587	3.9587	3.9587	3.9587	3.9587
1100				4.0472	4.0472	4.0472	4.0472	4.0472
1129				1.7556	4.1547	4.1547	4.1547	4.1547
1168				0.5383	4.3002	4.3002	4.3002	4.3002
1222					4.5030	4.5030	4.5030	4.5030
1230					2.8516	4.5331	4.5331	4.5331
1277					0.6004	4.7108	4.7108	4.7108
1331						4.9158	4.9158	4.9158
1395						3.2516	5.1594	5.1594
1408						0.6768	5.2090	5.2090
1462							5.4149	5.4149
1570							3.6679	5.8264
1612							2.7084	5.9860
1621								6.0202
1774								4.1409
1908								3.2402

Table 19: Recalculation for Fe/(Fe+Mg)=0 ("iron-poor" silicates; ips) from optical constants data from Semenov et al.[31] (2003).

Planck mean extinction coefficients [cm^2/g]

T [K]	ρ [g cm^{-3}] 10^{-18}	10^{-16}	10^{-14}	10^{-12}	10^{-10}	10^{-8}	10^{-6}	10^{-4}
10	0.0550	0.0550	0.0550	0.0550	0.0550	0.0550	0.0550	0.0550
20	0.2462	0.2462	0.2462	0.2462	0.2462	0.2462	0.2462	0.2462
40	1.5221	1.5221	1.5221	1.5221	1.5221	1.5221	1.5221	1.5221
60	3.1383	3.1383	3.1383	3.1383	3.1383	3.1383	3.1383	3.1383
80	4.3238	4.3238	4.3238	4.3238	4.3238	4.3238	4.3238	4.3238
100	5.4179	5.4179	5.4179	5.4179	5.4179	5.4179	5.4179	5.4179
109	5.9608	5.9608	5.9608	5.9608	5.9608	5.9608	5.9608	5.9608
118	3.2236	6.5441	6.5441	6.5441	6.5441	6.5441	6.5441	6.5441
129	3.6448	3.6448	7.3026	7.3026	7.3026	7.3026	7.3026	7.3026
143	4.1570	4.1570	4.1570	8.3083	8.3083	8.3083	8.3083	8.3083
159	4.7039	4.7039	4.7039	4.7039	9.4535	9.4535	9.4535	9.4535
180	5.3544	5.3544	5.3544	5.3544	5.3544	10.8499	10.8499	10.8499
200	5.9030	5.9030	5.9030	5.9030	5.9030	5.9030	11.9962	11.9962
207	6.0792	6.0792	6.0792	6.0792	6.0792	6.0792	12.3491	12.3491
244	6.8885	6.8885	6.8885	6.8885	6.8885	6.8885	6.8885	13.8105
275	7.4332	7.4332	7.4332	7.4332	7.4332	7.4332	7.4332	7.4332
300	6.8829	6.8829	6.8829	6.8829	6.8829	6.8829	6.8829	6.8829
400	7.9173	7.9173	7.9173	7.9173	7.9173	7.9173	7.9173	7.9173
425	8.1499	8.1499	8.1499	8.1499	8.1499	8.1499	8.1499	8.1499
500	3.9585	3.9585	3.9585	3.9585	3.9585	3.9585	3.9585	3.9585
680	4.5285	4.5285	4.5285	4.5285	4.5285	4.5285	4.5285	4.5285
700	3.2626	3.2626	3.2626	3.2626	3.2626	3.2626	3.2626	3.2626
835	3.6314	3.6314	3.6314	3.6314	3.6314	3.6314	3.6314	3.6314
908	2.0962	3.8678	3.8678	3.8678	3.8678	3.8678	3.8678	3.8678
920	2.1120	2.1120	3.9085	3.9085	3.9085	3.9085	3.9085	3.9085
929	0.5463	2.1242	3.9394	3.9394	3.9394	3.9394	3.9394	3.9394
980		2.1990	4.1184	4.1184	4.1184	4.1184	4.1184	4.1184
994		0.5822	4.1687	4.1687	4.1687	4.1687	4.1687	4.1687
997		0.5839	2.2258	4.1796	4.1796	4.1796	4.1796	4.1796
1049			2.3126	4.3702	4.3702	4.3702	4.3702	4.3702
1076			0.6302	4.4711	4.4711	4.4711	4.4711	4.4711
1100				4.5616	4.5616	4.5616	4.5616	4.5616
1129				2.4579	4.6719	4.6719	4.6719	4.6719
1168				0.6863	4.8216	4.8216	4.8216	4.8216
1222					5.0307	5.0307	5.0307	5.0307
1230					3.1310	5.0619	5.0619	5.0619
1277					0.7545	5.2452	5.2452	5.2452
1331						5.4565	5.4565	5.4565
1395						3.5369	5.7071	5.7071
1408						0.8373	5.7579	5.7579
1462							5.9689	5.9689
1570							3.9528	6.3880
1612							3.0852	6.5497
1621								6.5842
1774								4.4186
1908								3.5702

Table 20: Recalculation for Fe/(Fe+Mg)=0 ("iron-poor" silicates; ips) from optical constants data from Semenov et al.[31] (2003).

Rosseland mean extinction coefficients [cm^2/g]

T [K]	ρ [g cm^{-3}] 10^{-18}	10^{-16}	10^{-14}	10^{-12}	10^{-10}	10^{-8}	10^{-6}	10^{-4}
10	0.0153	0.0153	0.0153	0.0153	0.0153	0.0153	0.0153	0.0153
20	0.0697	0.0697	0.0697	0.0697	0.0697	0.0697	0.0697	0.0697
40	0.3247	0.3247	0.3247	0.3247	0.3247	0.3247	0.3247	0.3247
60	0.8213	0.8213	0.8213	0.8213	0.8213	0.8213	0.8213	0.8213
80	1.5482	1.5482	1.5482	1.5482	1.5482	1.5482	1.5482	1.5482
100	2.4433	2.4433	2.4433	2.4433	2.4433	2.4433	2.4433	2.4433
109	2.8880	2.8880	2.8880	2.8880	2.8880	2.8880	2.8880	2.8880
118	1.6702	3.3546	3.3546	3.3546	3.3546	3.3546	3.3546	3.3546
129	1.9899	1.9899	3.9506	3.9506	3.9506	3.9506	3.9506	3.9506
143	2.4215	2.4215	2.4215	4.7398	4.7398	4.7398	4.7398	4.7398
159	2.9360	2.9360	2.9360	2.9360	5.6615	5.6615	5.6615	5.6615
180	3.6190	3.6190	3.6190	3.6190	3.6190	6.8476	6.8476	6.8476
200	4.2477	4.2477	4.2477	4.2477	4.2477	4.2477	7.8882	7.8882
207	4.4580	4.4580	4.4580	4.4580	4.4580	4.4580	8.2222	8.2222
244	5.4552	5.4552	5.4552	5.4552	5.4552	5.4552	5.4552	9.6848
275	6.1328	6.1328	6.1328	6.1328	6.1328	6.1328	6.1328	6.1328
300	5.7343	5.7343	5.7343	5.7343	5.7343	5.7343	5.7343	5.7343
400	6.8753	6.8753	6.8753	6.8753	6.8753	6.8753	6.8753	6.8753
425	7.1195	7.1195	7.1195	7.1195	7.1195	7.1195	7.1195	7.1195
500	2.5639	2.5639	2.5639	2.5639	2.5639	2.5639	2.5639	2.5639
680	3.1944	3.1944	3.1944	3.1944	3.1944	3.1944	3.1944	3.1944
700	2.4087	2.4087	2.4087	2.4087	2.4087	2.4087	2.4087	2.4087
835	2.8954	2.8954	2.8954	2.8954	2.8954	2.8954	2.8954	2.8954
908	2.7882	3.1867	3.1867	3.1867	3.1867	3.1867	3.1867	3.1867
920	2.8331	2.8331	3.2361	3.2361	3.2361	3.2361	3.2361	3.2361
929	2.8299	2.8671	3.2735	3.2735	3.2735	3.2735	3.2735	3.2735
980		3.0636	3.4895	3.4895	3.4895	3.4895	3.4895	3.4895
994		3.0791	3.5499	3.5499	3.5499	3.5499	3.5499	3.5499
997		3.0909	3.1306	3.5630	3.5630	3.5630	3.5630	3.5630
1049			3.3397	3.7920	3.7920	3.7920	3.7920	3.7920
1076			3.4080	3.9132	3.9132	3.9132	3.9132	3.9132
1100				4.0223	4.0223	4.0223	4.0223	4.0223
1129				3.6727	4.1554	4.1554	4.1554	4.1554
1168				3.7931	4.3369	4.3369	4.3369	4.3369
1222					4.5921	4.5921	4.5921	4.5921
1230					4.5825	4.6302	4.6302	4.6302
1277					4.2671	4.8561	4.8561	4.8561
1331						5.1188	5.1188	5.1188
1395						5.3794	5.4338	5.4338
1408						4.8561	5.4983	5.4983
1462							5.7670	5.7670
1570							6.2474	6.3092
1612							0.5081	6.5211
1621								6.5666
1774								7.2701
1908								0.6079

Table 21: Recalculation for Fe/(Fe+Mg)=0.4 ("iron-rich" silicates; irs) from optical constants data from Semenov et al.[31] (2003).

Planck mean extinction coefficients [cm^2/g]

T [K]	ρ [g cm^{-3}]							
	10^{-18}	10^{-16}	10^{-14}	10^{-12}	10^{-10}	10^{-8}	10^{-6}	10^{-4}
10	0.0526	0.0526	0.0526	0.0526	0.0526	0.0526	0.0526	0.0526
20	0.2459	0.2459	0.2459	0.2459	0.2459	0.2459	0.2459	0.2459
40	1.5470	1.5470	1.5470	1.5470	1.5470	1.5470	1.5470	1.5470
60	3.2347	3.2347	3.2347	3.2347	3.2347	3.2347	3.2347	3.2347
80	4.5517	4.5517	4.5517	4.5517	4.5517	4.5517	4.5517	4.5517
100	5.8143	5.8143	5.8143	5.8143	5.8143	5.8143	5.8143	5.8143
109	6.4347	6.4347	6.4347	6.4347	6.4347	6.4347	6.4347	6.4347
118	3.7718	7.0923	7.0923	7.0923	7.0923	7.0923	7.0923	7.0923
129	4.2760	4.2760	7.9338	7.9338	7.9338	7.9338	7.9338	7.9338
143	4.8770	4.8770	4.8770	9.0283	9.0283	9.0283	9.0283	9.0283
159	5.4986	5.4986	5.4986	5.4986	10.2482	10.2482	10.2482	10.2482
180	6.2023	6.2023	6.2023	6.2023	6.2023	11.6978	11.6978	11.6978
200	6.7579	6.7579	6.7579	6.7579	6.7579	6.7579	12.8511	12.8511
207	6.9279	6.9279	6.9279	6.9279	6.9279	6.9279	13.1977	13.1977
244	7.6468	7.6468	7.6468	7.6468	7.6468	7.6468	7.6468	14.5688
275	8.0682	8.0682	8.0682	8.0682	8.0682	8.0682	8.0682	8.0682
300	7.4048	7.4048	7.4048	7.4048	7.4048	7.4048	7.4048	7.4048
400	8.0091	8.0091	8.0091	8.0091	8.0091	8.0091	8.0091	8.0091
425	8.1547	8.1547	8.1547	8.1547	8.1547	8.1547	8.1547	8.1547
500	3.7596	3.7596	3.7596	3.7596	3.7596	3.7596	3.7596	3.7596
680	4.1155	4.1155	4.1155	4.1155	4.1155	4.1155	4.1155	4.1155
700	3.5184	3.5184	3.5184	3.5184	3.5184	3.5184	3.5184	3.5184
835	3.9924	3.9924	3.9924	3.9924	3.9924	3.9924	3.9924	3.9924
908	3.9787	4.3110	4.3110	4.3110	4.3110	4.3110	4.3110	4.3110
920	4.0294	4.0294	4.3665	4.3665	4.3665	4.3665	4.3665	4.3665
929	4.0261	4.0680	4.4086	4.4086	4.4086	4.4086	4.4086	4.4086
980		4.2941	4.6542	4.6542	4.6542	4.6542	4.6542	4.6542
994		4.3140	4.7235	4.7235	4.7235	4.7235	4.7235	4.7235
997		4.3277	4.3720	4.7385	4.7385	4.7385	4.7385	4.7385
1049			4.6164	5.0025	5.0025	5.0025	5.0025	5.0025
1076			4.6994	5.1426	5.1426	5.1426	5.1426	5.1426
1100				5.2687	5.2687	5.2687	5.2687	5.2687
1129				5.0072	5.4225	5.4225	5.4225	5.4225
1168				5.1514	5.6317	5.6317	5.6317	5.6317
1222					5.9244	5.9244	5.9244	5.9244
1230					5.9145	5.9680	5.9680	5.9680
1277					5.7016	6.2249	6.2249	6.2249
1331						6.5211	6.5211	6.5211
1395						6.8114	6.8721	6.8721
1408						6.3697	6.9433	6.9433
1462							7.2382	7.2382
1570							7.7542	7.8226
1612							0.5788	8.0473
1621								8.0952
1774								8.8196
1908								0.6698

Table 22: Recalculation for Fe/(Fe+Mg)=0.4 ("iron-rich" silicates; irs) from optical constants data from Semenov et al.[31] (2003).